SPONTANEOUS-EMISSION RATES OF QUANTUM DOTS AND DYES CONTROLLED WITH PHOTONIC CRYSTALS

Promotiecommissie:

Promotor:	prof. dr. W. L. Vos
Overige leden:	prof. dr. J.-M. Gérard
	prof. dr. A. Lagendijk
	dr. P. Lodahl
	prof. dr. V. Subramaniam
	prof. dr. D. Vanmaekelbergh

The work described in this thesis is a part of the research program of the "Stichting voor Fundamenteel Onderzoek der Materie" (FOM), which is financially supported by the "Nederlandse Organisatie voor Wetenschappelijk Onderzoek" (NWO).

This work was carried out in the group *Complex Photonic Systems* (COPS), *Faculty of Science and Technology* and *MESA+ Research Institute for Nanotechnology*, *University of Twente*, Enschede, The Netherlands and in the group *Photonic Bandgaps*, at *Center for Nanophotonics*, *AMOLF Institute*, Amsterdam, The Netherlands.

This thesis can be downloaded from *www.photonicbandgaps.com.*
Printed by Print Partners Ipskamp, Enschede, The Netherlands.
ISBN: 90-365-2414-8

SPONTANEOUS-EMISSION RATES OF QUANTUM DOTS AND DYES CONTROLLED WITH PHOTONIC CRYSTALS

SPONTANE-EMISSIE SNELHEDEN VAN QUANTUM DOTS EN KLEURSTOFFEN BEHEERST DOOR FOTONISCHE KRISTALLEN

(met een samenvatting in het Nederlands)

PROEFSCHRIFT

ter verkrijging van
de graad van doctor aan de Universiteit Twente,
op gezag van de rector magnificus,
prof. dr. W. H. M. Zijm,
volgens besluit van het College voor Promoties
in het openbaar te verdedigen
op donderdag 2 november 2006 om 15.00 uur

door

Ivan Sergejevitsj Nikolaev

geboren op 21 december 1978
te Oelan-Oede (Sovjet-Unie)

Dit proefschrift is goedgekeurd door:

prof. dr. W. L. Vos

To all my teachers

CONTENTS

CHAPTER 1

INTRODUCTION

1.1 General introduction

Spontaneous emission is an essential process in generation of light from many different sources of energy such as heat, electricity or chemical interactions, and consequently, it is ultimately responsible for most of the light around us. This process entails radiation of photons in transitions between high-energy and low-energy states of elementary emitters. The latter include atoms (*e.g.*, sodium in light bulbs), molecules (organic dyes) and artificial nanostructures (quantum dots, wires and wells). Spontaneous emission is often called *luminescence*, when radiative transitions occur from emitters that are not excited by temperature alone. And if light is generated by re-emission from elementary sources that are excited by photons, this process is also called *fluorescence*. Since spontaneous emission is crucial for diverse everyday applications such as light-emitting diodes, lasers, TV screens, energy harvesting in solar cells, it is obvious that control over this phenomenon is of great importance.

Spontaneous emission is a bright example of elementary interaction between matter and light, which is closely related to *stimulated* emission: both effects are results of the coupling of emitters to the electromagnetic field [1, 2]. In the case of spontaneous emission, the optical transitions occur via interaction with virtual photons (vacuum fluctuations or vacuum state of the field); while in stimulated emission, the emitters interact with real photons (other field states). It appears that the interaction between emitters and the field can be raised by enhancing the density of the vacuum fluctuations. It was predicted already in 1946 that the emission decay rate (the depopulation rate of the excited state) can be increased, if the emitter is placed in a cavity tuned to its transition frequency [3], and can be decreased if the cavity is detuned [4].

Ultimate inhibition of spontaneous emission can be achieved in artificial periodic structures with tailor-made forbidden frequency bands [5]. These periodic structures known as *photonic crystals* consist of different dielectric materials, where the index of refraction varies on length scales comparable to the wavelength of light. Therefore, the periodicity of photonic crystals is about 1000 times as large as that of atomic crystals. Light with specific frequencies is forbidden to propagate along certain directions by wave interference, similarly to Bragg diffraction of x-rays in atomic crystals. Such forbidden frequency ranges are called *stopgaps*. The larger the contrast of the refractive index between the two materials of a photonic crystal, the more strongly light is influenced, and the broader the stopgaps become. It was predicted in 1987 that an extreme situation may be feasible when light cannot propagate along any direction [6, 7]. This situation is called a *photonic bandgap*. Spontaneous emission is completely inhibited for frequencies inside such a bandgap and, conversely, strongly enhanced for frequencies outside the bandgap. Photonic crystals, therefore, provide an ultimate tool for manipulating with light, which is of extreme interest for scientists and engineers [8, 9].

Recent advances in nanotechnology have resulted in ability to synthesize semiconductor structures with dimensions of a few nanometers. Due to the finite sizes, electron-hole pairs (excitons) can be confined in these nanostructures, which leads to discrete excitonic energy levels. The nanocrystals that confine excitons in spherical or circular spaces are known as *quantum dots*. The discrete structure of the energy levels results in advantageous optical properties of these nanocrystals: narrow and tunable emission spectra. The emission frequencies can be tuned by varying the nanocrystal size: the smaller the size, the higher the emission frequency. These properties make the nanocrystals very promising elementary emitters for new experiments and devices [10, 11].

1.2 Outline of the thesis

This thesis describes time- and angle-resolved experiments, in which effects of three-dimensional (3D) photonic crystals on spontaneous emission of embedded light sources (quantum dots and dye molecules) were studied. The thesis is organized as follows:

In Chapter 2 we review the theoretical basics of the interaction between light and matter. We discuss the factors triggering the process of spontaneous emission and consider in detail the time evolution of the excited state of the emitter that interacts with the quantized

vacuum field. Relation between the rate of spontaneous emission and the local density of states (LDOS) is derived. We discuss conditions, when the excited-state population decays exponentially in time, and how these dynamics can be affected. Propagation of light in photonic crystals is examined. By the example of a 1D photonic crystal, we explain the origin of the stopgap. With the help of photonic dispersion relations, we illustrate important properties of 3D photonic crystals. Strong modifications of the LDOS and radiative rates in 3D photonic crystals predicted by theory are discussed.

In Chapter 3 we discuss tools necessary to control spontaneous emission. We review experimentally realized photonic-bandgap structures, the requirements on their crystal symmetry and the dielectric contrast for opening of the bandgap as well as the methods to fabricate such periodic structures on a large scale. We discuss optical probes necessary for studying the interaction of light with real photonic crystals. These probes include measurements of angle-resolved spectra of reflected and transmitted light as well as emission from internal light sources. We consider the role of unavoidable structural disorder in light propagation through the real photonic crystals. Photonic crystals used in our emission experiments, namely polystyrene opals and titania inverse opals, are described. Finally, we discuss light sources that can be used as internal fluorescent probes of photonic crystals.

Chapter 4 describes the angle-resolved measurements of spontaneous-emission spectra from laser dyes and quantum dots in opal and inverse-opal photonic crystals. We observe pronounced directional dependencies of the emission spectra: angular ranges of strongly reduced emission adjoin with angular ranges of enhanced emission. It appears that emission from embedded light sources is affected both by the periodicity and by the structural imperfections of the crystals: the photons are Bragg diffracted by lattice planes and scattered by unavoidable structural disorder. We quantitatively explain the measured directional emission using a model that unifies diffuse light transport and the photonic band structure.

In Chapter 5 we present an experimental proof of strongly modified spontaneous-emission decay rates from an ensemble of CdSe quantum dots in the titania inverse-opal photonic crystals. By varying the crystal lattice parameter, we achieve both inhibition and enhancement of the emission decay rates. The complex decay curves are successfully analyzed with a continuous distribution of decay rates. The resulting most-frequent decay rate varies by a factor of 3, whereas the width of the distribution reveals a six-fold modification. This large modification of the distribution width in photonic crystals with different lattice parameters is identified with variations of the radiative rates from

quantum dots at various positions in the unit cell and with variously oriented transition dipoles. This interpretation is compared to calculations of the LDOS in the inverse opals. The mean emission rate varies by a factor of 8, in conformity with the change of the total emitted power. By varying the optical frequency within the quantum-dot spectrum, we observe that the changes of the decay rate with the lattice parameter are larger at higher emission frequencies.

In Chapter 6 we discuss the LDOS in the titania inverse opals. We use the plane-wave expansion method to calculate the LDOS in many locations in the unit cell for different dipole orientations. We find that the LDOS in the inverse opals strongly depends on the crystal lattice parameter as well as on the position and orientation of emitting dipoles. We have identified conditions where the LDOS is strongly suppressed, strongly enhanced, and where sharp peaks (van Hove singularities) appear. For theoretical explanation of the experimental observations described in Chapter 5, we have made calculations of the LDOS in several positions in the internal TiO_2-air interface. At the frequencies near the first-order stopgap, the dependence of the LDOS on the crystal lattice parameter is preserved at all investigated locations and dipole orientations, which is agreement with the experimental observations.

Chapter 7 presents a time-resolved study of spontaneous emission from Rhodamine 6G dye in opal photonic crystals. We have measured fluorescence lifetimes of the dye by varying both optical frequency and crystal lattice parameter of polystyrene opals. The observed fluorescence lifetimes are nearly frequency independent within the dye emission spectrum, which is attributed to a broad homogeneous linewidth of the dye. However, the fluorescence lifetimes are modified when the crystal lattice parameter is changed: we observe 16 % enhancement and 10 % inhibition of spontaneous emission, which is explained by the LDOS varying in the opals in bandwidths comparable to the homogeneous linewidth of the dye. The changes of spontaneous emission induced by the polystyrene opals are considerably smaller than the effects measured in the titania inverse opals, which is related to much weaker changes of the LDOS in the opals compared to the inverse opals.

References

[1] S. Haroche and D. Kleppner, *Cavity Quantum Electrodynamics*, Phys. Today **42**, 24 (1989).

[2] Y. Yamamoto and R. E. Slusher, *Optical Processes in Microcavities*, Phys. Today **46**, 66 (1993).

[3] E. M. Purcell, *Spontaneous Emission Probabilities at Radio Frequencies*, Phys. Rev. **69**, 681 (1946).

[4] D. Kleppner, *Inhibited Spontaneous Emission*, Phys. Rev. Lett. **47**, 233 (1981).

[5] V. P. Bykov, *Spontaneous Emission from a Medium with a Band Spectrum*, Sov. J. Quant. Electron. **4**, 861 (1975).

[6] E. Yablonovitch, *Inhibited Spontaneous Emission in Solid-State Physics and Electronics*, Phys. Rev. Lett. **58**, 2059 (1987).

[7] S. John, *Strong Localization of Photons in Certain Disordered Dielectric Superlattices*, Phys. Rev. Lett. **58**, 2486 (1987).

[8] J. D. Joannopoulos, R. D. Meade and J. N. Winn, *Photonic Crystals: Molding the Flow of Light*, Princenton University Press, (1995).

[9] C. M. Soukoulis, editor, *Photonic Crystals and Light Localization in the 21st Century*, Kluwer, Dordrecht, (2001).

[10] A. P. Alivisatos, *Perspectives on the Physical Chemistry of Semiconductor Nanocrystals*, J. Phys. Chem. **100**, 13226 (1996).

[11] D. Bimberg, M. Grundmann and N. Ledentsov, *Quantum Dot Heterostructures*, Wiley & Sons Ltd, Chichester, England (1999).

CHAPTER 2

EMISSION AND PROPAGATION OF LIGHT IN PHOTONIC CRYSTALS

This chapter reviews the theoretical basics of the interaction between light and matter, which is needed in order to understand experiments described in this thesis. We discuss the factors triggering the process of spontaneous emission. The time evolution of the excited state that interacts with the quantized vacuum field is considered in detail. We derive the relation between the rate of spontaneous emission and the local density of vacuum-field states (LDOS). We discuss conditions, when the excited-state population decays exponentially in time, and how these dynamics can be affected. After introducing the concept of photonic crystals - a means to control spontaneous emission, we examine the principles determining propagation of light in these periodic structures. By example of a 1D photonic crystal, we explain the origin of the photonic stopgap. Important properties of 3D photonic crystals are illustrated with the help of photonic dispersion relations, which are calculated using the H-field plane-wave expansion method. We discuss strong modifications of the LDOS and radiative rates in 3D photonic crystals. Finally, alternative methods to calculate the LDOS in finite periodic structures are briefly considered.

2.1 Phenomenon of spontaneous emission

Spontaneous emission of light is called a transition of an emitter (atom, molecule or quantum dot) from its excited state to its lower energy state by sending out one or more photons. The effect received its name "spontaneous" in the classical theory of electromagnetism where there is no radiation field without photons, and without radiation field, atoms can stay forever in their exited states [1]. Although some aspects of atomic radiative transitions such as Einstein's coefficients can be explained in classical optics, a correct description of spontaneous emission requires quantization of the radiation field [2]. In quantum optics, even in absence of photons, the vacuum state still has an energy

per mode of $\frac{1}{2}\hbar\omega$, and consequently, it has non-zero expectation values of the squares of the electric and magnetic fields. Therefore, in the vacuum field state, and in all other stationary field states, the electric and magnetic fields fluctuate around their zero mean values. Interaction of excited atoms with these so-called vacuum fluctuations can explain the "spontaneous" decay to lower atomic states. Other quantum phenomena such as the Casimir forces and the Lamb shift are also regarded as consequences of the vacuum-field fluctuations [1, 2].

In this section we shall consider the quantum theory of interaction of an emitter with the radiation field. We will focus our attention on the interaction of the two-level emitter with a continuum of the radiation-field modes. A two-level description is valid when only two levels of an emitter (atom, molecule or quantum dot) are involved in the transition, while effects of other levels are negligible. With the help of certain realistic approximations, we will derive an expression for the decay rate of the excited state of a two-level atomic system and discuss the factors determining this decay rate. For simplicity the "two-level emitter" will be called "atom" further in the text.

2.1.1 Atom-field interaction Hamiltonian

The interaction of an atom with a radiation field **E** is described by the Hamiltonian:

$$\mathcal{H} = \mathcal{H}_F + \mathcal{H}_A + \mathcal{H}_{int}. \tag{2.1}$$

Here the operators $\mathcal{H}_A$ and $\mathcal{H}_F$ represent the energies of the atom and the radiation field in absence of interaction, respectively; $\mathcal{H}_{int}$ represents the atom-field interaction energy. The operator of the radiation-field energy is given in terms of the creation operators $a^\dagger_{\mathbf{k}}$ and the annihilation operators $a_{\mathbf{k}}$ of the field modes with wavevectors **k** by

$$\mathcal{H}_F = \sum_{\mathbf{k}} \hbar\omega_{\mathbf{k}}(a^\dagger_{\mathbf{k}} a_{\mathbf{k}} + 1/2).^{(1)} \tag{2.2}$$

$\mathcal{H}_A$ and $\mathcal{H}_{int}$ can be expressed in terms of the transition operators $\sigma_{ij} = |i\rangle\langle j|$. Here $\{|i\rangle\}$ represents a complete set of atomic energy eigenstates, *i.e.*, $\sum_i |i\rangle\langle i| = 1$. From the eigenvalue equation $\mathcal{H}_A|i\rangle = \mathcal{E}_i|i\rangle$ it follows that

$$\mathcal{H}_A = \sum_i \mathcal{E}_i|i\rangle\langle i| = \sum_i \mathcal{E}_i\sigma_{ii} = \mathcal{E}_a\sigma_{aa} + \mathcal{E}_b\sigma_{bb}. \tag{2.3}$$

(1) We write operators in the Schrödinger picture, in which the operators are time independent, but the wavefunctions carry the entire time dependency.

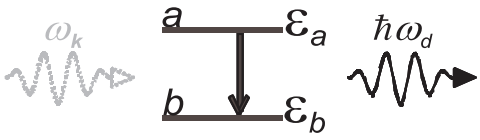

FIGURE 2.1: Scheme of the interaction of a two-level atom in its excited state *a* with a continuum of vacuum-field modes with frequency $\omega_{\mathbf{k}}$, leading to a transition to the atomic ground state *b* via emission of a photon with energy $\hbar\omega_d = \mathcal{E}_a - \mathcal{E}_b$.

In our case of a two-level atom, $\mathcal{E}_a$ and $\mathcal{E}_b$ are the energies of the excited and ground states, respectively, as shown in Figure 2.1. The interaction Hamiltonian in the electric dipole approximation is

$$\mathcal{H}_{int} = -\mathbf{d} \cdot \mathbf{E}, \tag{2.4}$$

where $\mathbf{d}$ is the operator of the electric-dipole transition moment that is given by

$$\mathbf{d} = \sum_{i,j} e|i\rangle\langle i|\mathbf{r}_e|j\rangle\langle j| = \mathbf{d}_{ab}\sigma_{ab} + \mathbf{d}_{ba}\sigma_{ba}. \tag{2.5}$$

Here, $\mathbf{r}_e$ is the displacement operator of the electron with charge e relative to the position of the atom $\mathbf{r}$. $\mathbf{d}_{ij} = e\langle i|\mathbf{r}_e|j\rangle$ is the matrix element of the operator of the dipole transition between the states $|i\rangle$ and $|j\rangle$. It can be shown that $\mathbf{d}_{ab} = \mathbf{d}_{ba}$. We will further write $\mathbf{d}_{ab}$ as $d\mathbf{e}_d$, where d is the magnitude and $\mathbf{e}_d$ is the orientation of $\mathbf{d}_{ab}$. The electric-field operator is evaluated at the atom center $\mathbf{r}$ in the dipole approximation, *i.e.*, $\mathbf{k}\cdot\mathbf{r}_e \ll 1$. The quantized electric field $\mathbf{E}$ has the form:

$$\mathbf{E}(\mathbf{r}) = i\sum_{\mathbf{k},p} z_{\mathbf{k},p}(\mathbf{r})[a_{\mathbf{k},p}\mathbf{\Lambda}_{\mathbf{k},p}(\mathbf{r}) - a^{\dagger}_{\mathbf{k},p}\mathbf{\Lambda}^{*}_{\mathbf{k},p}(\mathbf{r})], \tag{2.6}$$

where $z_{\mathbf{k},p}(\mathbf{r}) = [\hbar\omega_{\mathbf{k},p}/2\epsilon_0\epsilon(\mathbf{r})V]^{\frac{1}{2}}$ is the normalization factor for a field mode $\mathbf{\Lambda}_{\mathbf{k},p}(\mathbf{r})$ with wavevector $\mathbf{k}$ and polarization state $p = 1{,}2$. $\epsilon(\mathbf{r})$ is the dielectric function that is generally position-dependent, V is an arbitrary quantization volume. For the sake of readability of the following formulae, we will leave out the summation on the field polarization p as this summation can be always inserted into the resulting formulae. Now we insert the expressions for $\mathbf{d}$ and $\mathbf{E}(\mathbf{r})$ into Eq. 2.4 and substitute for $\mathcal{H}_A$, $\mathcal{H}_F$ and $\mathcal{H}_{int}$ from Eqs. 2.2, 2.3 and 2.4 into Eq. 2.1 to obtain:

$$\mathcal{H} = \sum_{\mathbf{k}} \hbar\omega_{\mathbf{k}} a_{\mathbf{k}}^{\dagger} a_{\mathbf{k}} + (\mathcal{E}_a \sigma_{aa} + \mathcal{E}_b \sigma_{bb}) + i \sum_{\mathbf{k}} \hbar(\sigma_{ab} + \sigma_{ba})[g_{\mathbf{k}}(\mathbf{r}) a_{\mathbf{k}} - g_{\mathbf{k}}^{*}(\mathbf{r}) a_{\mathbf{k}}^{\dagger}], \tag{2.7}$$

where

$$g_{\mathbf{k}}(\mathbf{r}) = -\hbar^{-1} z_{\mathbf{k}}(\mathbf{r}) \mathbf{d}_{ab} \cdot \mathbf{\Lambda}_{\mathbf{k}}(\mathbf{r}) = -\sqrt{\frac{\omega_{\mathbf{k}}}{2\epsilon_0 \epsilon(\mathbf{r}) \hbar V}} d\mathbf{e}_d \cdot \mathbf{\Lambda}_{\mathbf{k}}(\mathbf{r}). \tag{2.8}$$

In Eq. 2.7 the zero-point energy $\frac{1}{2}\sum_{\mathbf{k}} \hbar\omega_{\mathbf{k}}$ has been ignored because constant terms have no influence on the time behavior of the system. We write the second term in Eq. 2.7 as

$$\mathcal{E}_a \sigma_{aa} + \mathcal{E}_b \sigma_{bb} = \frac{1}{2}\hbar\omega_d(\sigma_{aa} - \sigma_{bb}) + \frac{1}{2}(\mathcal{E}_a + \mathcal{E}_b)(\sigma_{aa} + \sigma_{bb}), \tag{2.9}$$

where $\hbar\omega_d = \mathcal{E}_a - \mathcal{E}_b$ and $\sigma_{aa} + \sigma_{bb} = 1$. The constant energy $\frac{1}{2}(\mathcal{E}_a + \mathcal{E}_b)$ is again omitted. We use the notations

$$\begin{aligned} \sigma_z &= \sigma_{aa} - \sigma_{bb} = |a\rangle\langle a| - |b\rangle\langle b|, \\ \sigma_+ &= \sigma_{ab} = |a\rangle\langle b| \quad \text{and} \\ \sigma_- &= \sigma_{ba} = |b\rangle\langle a|, \end{aligned} \tag{2.10}$$

where the transition operators σ_+, σ_- and the inversion operator σ_z[(2)] satisfy Pauli's commutation relations:

$$\begin{aligned} [\sigma_-, \sigma_+] &= -\sigma_z, \\ [\sigma_-, \sigma_z] &= 2\sigma_-. \end{aligned} \tag{2.11}$$

Then, the Hamiltonian (2.7) takes the form

$$\mathcal{H} = \sum_{\mathbf{k}} \hbar\omega_{\mathbf{k}} a_{\mathbf{k}}^{\dagger} a_{\mathbf{k}} + \frac{1}{2}\hbar\omega_d \sigma_z + i\hbar \sum_{\mathbf{k}} (\sigma_+ + \sigma_-)[g_{\mathbf{k}} a_{\mathbf{k}} - g_{\mathbf{k}}^{*} a_{\mathbf{k}}^{\dagger}]. \tag{2.12}$$

For convenience we have left out the explicit $\mathbf{r}$-dependence of $g_{\mathbf{k}}(\mathbf{r})$ for a while.

2.1.2 Interaction in perturbation approach

In order to solve the evolution of the atom-field system described by the Hamiltonian (2.12), we use the perturbation approach and represent the Hamiltonian as $\mathcal{H} = \mathcal{H}_0 + \mathcal{H}_{int}$, where

$$\mathcal{H}_0 = \sum_{\mathbf{k}} \hbar\omega_{\mathbf{k}} a_{\mathbf{k}}^{\dagger} a_{\mathbf{k}} + \frac{1}{2}\hbar\omega_d \sigma_z \tag{2.13}$$

(2) $\frac{1}{2}\hbar\omega_d\sigma_z$ represents the internal energy of the atom, relative to the average $\frac{1}{2}(\mathcal{E}_a + \mathcal{E}_b)$, which we have set to zero. Therefore σ_z is often referred as the inversion operator.

is the Hamiltonian of the unperturbed atom-field system without any interaction. The perturbation due to the interaction between the atom and the field is described by

$$\mathcal{H}_{int} = i\hbar \sum_{\mathbf{k}} (\sigma_+ + \sigma_-)[g_{\mathbf{k}} a_{\mathbf{k}} - g^*_{\mathbf{k}} a^\dagger_{\mathbf{k}}]. \tag{2.14}$$

Furthermore, it appears to be convenient to represent the Hamiltonian in the interaction picture, which is related to the Schrödinger picture by

$$\mathcal{V} = e^{i\mathcal{H}_0 t/\hbar} \mathcal{H}_{int} e^{-i\mathcal{H}_0 t/\hbar}. \tag{2.15}$$

Using the identities[3]

$$e^{i\omega_{\mathbf{k}} a^\dagger_{\mathbf{k}} a_{\mathbf{k}} t} a_{\mathbf{k}} e^{-i\omega_{\mathbf{k}} a^\dagger_{\mathbf{k}} a_{\mathbf{k}} t} = a_{\mathbf{k}} e^{-i\omega_{\mathbf{k}} t} \text{ and}$$

$$e^{i\omega_d \sigma_z t/2} \sigma_+ e^{-i\omega_d \sigma_z t/2} = \sigma_+ e^{i\omega_d t}, \tag{2.16}$$

we rewrite the Hamiltonian as:

$$\mathcal{V} = i\hbar \sum_{\mathbf{k}} [g_{\mathbf{k}} (\sigma_+ a_{\mathbf{k}} e^{i(\omega_d - \omega_{\mathbf{k}})t} + \sigma_- a_{\mathbf{k}} e^{-i(\omega_d + \omega_{\mathbf{k}})t})$$

$$- g^*_{\mathbf{k}} (\sigma_- a^\dagger_{\mathbf{k}} e^{-i(\omega_d - \omega_{\mathbf{k}})t} + \sigma_+ a^\dagger_{\mathbf{k}} e^{i(\omega_d + \omega_{\mathbf{k}})t})]. \tag{2.17}$$

This Hamiltonian consists of four terms. The term $\sigma_+ a_{\mathbf{k}}$ describes the process of the atomic transition from the ground state to the excited state and annihilation of a photon in a $\mathbf{k}$-mode. The term $\sigma_- a^\dagger_{\mathbf{k}}$ describes the opposite process. In both processes the energy is conserved. The term $\sigma_+ a^\dagger_{\mathbf{k}}$ describes the process in which the atom makes a transition from the ground state to the excited state and a photon is created, resulting in an energy gain of $2\hbar\omega_{\mathbf{k}}$. Similarly, $\sigma_- a_{\mathbf{k}}$ results in the loss of the same energy. In the so-called *rotating-wave approximation*,[4] these energy non-conserving terms are dropped. The resulting Hamiltonian becomes

$$\mathcal{V} = i\hbar \sum_{\mathbf{k}} [g_{\mathbf{k}} \sigma_+ a_{\mathbf{k}} e^{i(\omega_d - \omega_{\mathbf{k}})t} - g^*_{\mathbf{k}} a^\dagger_{\mathbf{k}} \sigma_- e^{-i(\omega_d - \omega_{\mathbf{k}})t}]. \tag{2.18}$$

[3] These identities can be derived if we first write e^{xA} as a series expansion $\sum_{i=0}^{\infty} (xA)^i / i!$ that gives $e^{xA} B e^{-xA} = B + x[A, B] + \frac{x^2}{2!}[A, [A, B]] + ...$, and then use the commutation relations $[a_{\mathbf{k}}, a^\dagger_{\mathbf{k}}] = 1$, $[a_{\mathbf{k}}, a^\dagger_{\mathbf{k}} a_{\mathbf{k}}] = a_{\mathbf{k}}$ and those from Eqs. 2.11.

[4] When the radiation-field and dipole oscillations are close to a resonance, $\omega_{\mathbf{k}} \approx \omega_d$, terms proportional to $e^{\pm i(\omega_d - \omega_{\mathbf{k}})t}$ change slowly in time. The counter-rotating terms proportional to $e^{\pm i(\omega_d + \omega_{\mathbf{k}})t}$ vary rapidly on time scales $(\omega_d - \omega_{\mathbf{k}})^{-1}$ and are ignored in the rotating-wave approximation. The counter-rotating terms still affect dipoles giving rise to minute changes of the transition frequency ($\sim 10^{-10}\omega_d$), called the Bloch-Siegert shift [3].

Now we need to solve the Schrödinger equation for $|\Psi(t)\rangle$:

$$i\hbar\frac{\partial|\Psi(t)\rangle}{\partial t} = \mathcal{V}|\Psi(t)\rangle. \tag{2.19}$$

The state $|\Psi(t)\rangle$ is a linear combination of the states $|a,n\rangle$ and $|b,n\rangle$ of the unperturbed atom-field system. Here, $|a,n\rangle$ is the state, in which the atom is in its excited state and the field has n photons. $|b,n\rangle$ is the state, in which the atom is in its ground state and the field has n photons. Taking at time $t = 0$ the atom to be in the state $|a\rangle$ and the field in the vacuum mode $|0\rangle$, we write the state vector as

$$|\Psi(t)\rangle = c_a(t)|a,0\rangle + \sum_{\mathbf{k}} c_{b,\mathbf{k}}(t)|b,1_{\mathbf{k}}\rangle, \tag{2.20}$$

with initial conditions $c_a(0) = 1$ and $c_{b,\mathbf{k}}(0) = 0$. Because of the perturbation $\mathcal{H}_{int}$, the probability amplitudes c_a and $c_{b,\mathbf{k}}$ become time dependent. Since we want to determine the time evolution of the excited state, we must find an expression for the probability amplitude $c_a(t)$. From the Schrödinger equation we obtain the equation of motion for $c_a(t)$ and $c_{b,\mathbf{k}}(t)$:

$$\dot{c}_a(t) = \sum_{\mathbf{k}} g_{\mathbf{k}} e^{i(\omega_d-\omega_{\mathbf{k}})t} c_{b,\mathbf{k}}(t), \tag{2.21}$$

$$\dot{c}_{b,\mathbf{k}}(t) = -g^*_{\mathbf{k}} e^{-i(\omega_d-\omega_{\mathbf{k}})t} c_a(t). \tag{2.22}$$

To get an equation that contains $c_a(t)$ only, we first integrate Eq. 2.22:

$$c_{b,\mathbf{k}}(t) = -g^*_{\mathbf{k}} \int_0^t dt' e^{-i(\omega_d-\omega_{\mathbf{k}})t'} c_a(t'). \tag{2.23}$$

Then, we substitute the expression for $c_{b,\mathbf{k}}(t)$ into Eq. 2.21:

$$\dot{c}_a(t) = -\sum_{\mathbf{k}} |g_{\mathbf{k}}|^2 \int_0^t dt' e^{-i(\omega_d-\omega_{\mathbf{k}})(t'-t)} c_a(t'). \tag{2.24}$$

To resolve this integro-differential equation, several further approximations have to be made. We assume that the quantization volume V is much larger than the size of the atom. Therefore, there is a quasi-continuum of the field modes, and we can replace the summation over $\mathbf{k}$ by an integral: $\sum_{\mathbf{k}} \rightarrow \frac{V}{(2\pi)^3}\int_0^\infty d\mathbf{k}$. Then, Eq. 2.24 with $g_{\mathbf{k}}$ substituted by the expression in Eq. 2.8 becomes

$$\dot{c}_a(\mathbf{r},t) = -\frac{d^2}{2(2\pi)^3\epsilon_0\epsilon(\mathbf{r})\hbar}\int_0^t dt' c_a(\mathbf{r},t') \times \int_0^\infty d\mathbf{k}\, \omega_{\mathbf{k}} e^{-i(\omega_d-\omega_{\mathbf{k}})(t'-t)} |\mathbf{e}_d \cdot \mathbf{\Lambda}_{\mathbf{k}}(\mathbf{r})|^2. \tag{2.25}$$

It is convenient to add a frequency integration over a Dirac δ function, which does not affect the value of $\dot{c}_a(\mathbf{r}, t)$:

$$\dot{c}_a(\mathbf{r}, t) = -\frac{d^2}{2(2\pi)^3\epsilon_0\epsilon(\mathbf{r})\hbar}\int_0^t dt' c_a(\mathbf{r}, t') \times \int_0^\infty d\omega\omega e^{i(\omega-\omega_d)(t'-t)}\int_0^\infty d\mathbf{k}\delta(\omega-\omega_\mathbf{k})|\mathbf{e}_d\cdot\mathbf{\Lambda}_\mathbf{k}(\mathbf{r})|^2. \quad (2.26)$$

The frequency integral is defined only over positive frequencies, for there are no negative-energy field modes. We notice that Eq. 2.26 contains the local radiative density of optical states (LDOS), which counts the number of modes per unit volume at a given frequency ω to which the atomic dipole oriented along $\mathbf{e}_d$ and positioned at $\mathbf{r}$ can couple. This projected LDOS is defined as [4]:

$$N(\mathbf{r}, \omega, \mathbf{e}_d) \equiv \frac{1}{(2\pi)^3\epsilon(\mathbf{r})}\sum_p\int_0^\infty d\mathbf{k}\delta(\omega-\omega_{\mathbf{k},p})|\mathbf{e}_d\cdot\mathbf{\Lambda}_{\mathbf{k},p}(\mathbf{r})|^2, \quad (2.27)$$

where we have inserted back the summation on the field polarization p. The dielectric function $\epsilon(\mathbf{r})$ must be real here, otherwise the complex mode density $N(\mathbf{r}, \omega, \mathbf{e}_d)$ is not defined. The LDOS will be discussed in more detail in Section 2.3. Thus we have the equation of motion

$$\dot{c}_a(\mathbf{r}, t) = -\frac{d^2}{2\hbar\epsilon_0}\int_0^t dt' c_a(\mathbf{r}, t')\int_0^\infty d\omega\omega N(\mathbf{r}, \omega, \mathbf{e}_d)e^{i(\omega-\omega_d)(t'-t)}, \quad (2.28)$$

where the time integral means that the atom-field system has a memory of $c_a(\mathbf{r}, t)$ at earlier times.

2.1.3 Rate and frequency shift of spontaneous emission

To solve the equation of motion (Eq. 2.28), we replace the probability amplitude $c_a(\mathbf{r}, t')$ by $c_a(\mathbf{r}, t)$ taken at time t. This approach called *Markov approximation*, assumes that if a photon is emitted, memory of this event is lost practically instantly [1, 2]. The time integral then becomes

$$\int_0^t dt' e^{i(\omega-\omega_d)(t'-t)} = \frac{\sin(\omega-\omega_d)t}{\omega-\omega_d} - \frac{i[1-\cos(\omega-\omega_d)t]}{\omega-\omega_d}. \quad (2.29)$$

For sufficiently long times, so that $\omega_d t \gg 1$, the first term in Eq. 2.29 vanishes due to fast oscillations of $\sin(\omega-\omega_d)t$, except if $\omega = \omega_d$; then it equals t. Similarly, the second term

is $(\omega - \omega_d)^{-1}$, except at $\omega = \omega_d$ where it is 0. Therefore, for the case when Eq. 2.29 is in a frequency integral, we can rewrite it as

$$\int_0^t dt' e^{i(\omega-\omega_d)(t'-t)} = \pi\delta(\omega - \omega_d) - iP(\omega - \omega_d)^{-1}, \tag{2.30}$$

where P denotes the Cauchy principal value, and δ is the delta function[2]. If we substitute the resulting expression into Eq. 2.28, it follows that

$$\dot{c}_a(\mathbf{r}, t) = -(\gamma/2 - i\Delta)c_a(\mathbf{r}, t), \tag{2.31}$$

where

$$\gamma = \frac{\pi d^2 \omega_d}{\hbar\epsilon_0} N(\mathbf{r}, \omega_d, \mathbf{e}_d) \tag{2.32}$$

is the rate of the optical transition $|a\rangle \rightarrow |b\rangle$; and

$$\Delta = \frac{d^2}{2\hbar\epsilon_0} P \int_0^\infty \frac{d\omega\omega N(\mathbf{r}, \omega, \mathbf{e}_d)}{\omega - \omega_d} \tag{2.33}$$

represents a shift of the transition frequency ω_d called the *Lamb shift* [1, 2]. From Eq. 2.31 we obtain the expression for the time evolution of the atomic excited state:

$$|c_a(\mathbf{r}, t)|^2 = e^{-\gamma t}. \tag{2.34}$$

Thus, with the help of several approximations, we have derived a simple expression for the probability $|c_a(\mathbf{r}, t)|^2$ of the excited state, which reveals an exponential decay in time with the rate constant γ.

In the Markov approximation we assume that the quasi-continuum of the field modes, the *bath*, is much faster than the oscillation period of the dipole τ_d. Because the LDOS $N(\mathbf{r}, \omega_d, \mathbf{e}_d)$ has a dimension of *per frequency*, it can be considered as the correlation time of the bath τ_b [5]. We can estimate τ_b for the LDOS at optical frequencies ($\sim 10^{-15}$ Hz) in a quantization volume $V = (2\pi c/\omega)^3$: the resulting correlation time τ_b is $\sim 10^{-18}$ s, which is much shorter than $\tau_d \sim 10^{-15}$ s. Therefore, the interaction of the emitting dipole with the fast bath destroys the memory of the past and leads to the exponential decay of the excited state. Interestingly, when the LDOS increases, the bath becomes slow. And when the correlation time τ_b is longer than the dipole oscillation period τ_d, the system retains the memory of the previous times. This means that the atom and the bath are strongly coupled, and the evolution of the atomic excited state is not an exponential decay. The Markov approximation, which is justified in the case of weak atom-field coupling,

is related to the *Weisskopf-Wigner approximation*. The latter assumes that the product $\omega N(\mathbf{r}, \omega, \mathbf{e}_d)$ is a slowly varying function of ω around the dipole transition frequency ω_d, so that in Eq. 2.28, ω can be replaced with ω_d [1]. The frequency integral then becomes proportional to $\delta(t' - t)$, which also results in the exponential decay shown in Eq. 2.34.

From Eq. 2.32 we conclude that the rate of spontaneous emission γ is determined by the electric-dipole moment d and frequency ω_d of the transition $|a\rangle \rightarrow |b\rangle$, and the LDOS at the transition frequency and at the atom position. The first two factors are internal atomic properties, whereas the last one, the LDOS, depends on the environment of the atom. If the atom is placed in an unbounded homogeneous dielectric with $\epsilon(\mathbf{r}) = \epsilon$, the spontaneous-emission rate is position independent and can be readily calculated. For an isotropic medium, we can easily perform integration over $\mathbf{k}$ in the expression for $N(\mathbf{r}, \omega, \mathbf{e}_d)$:

$$\sum_p \int_0^\infty d\mathbf{k} = 2 \int_0^{2\pi} d\phi \int_0^\pi d\theta \sin\theta \int_0^\infty dk k^2. \tag{2.35}$$

Since $k = |\mathbf{k}| = n\omega_k/c$ with the refractive index of the medium $n = \sqrt{\epsilon}$, we write

$$N(\omega) = \frac{4\pi}{(2\pi)^3 n^2} \int_0^\pi d\theta \sin\theta \cos^2\theta \int_0^\infty d\omega_k \frac{n^3}{c^3} {\omega_k}^2 \delta(\omega - \omega_k), \tag{2.36}$$

where θ is the angle between the dipole orientation $\mathbf{e}_d$ and the k-mode vector $\mathbf{\Lambda}_\mathbf{k}$. Thus the radiative density of states per unit volume becomes

$$N(\omega) = \frac{n\omega^2}{3\pi^2 c^3}, \tag{2.37}$$

and gives the familiar expression for the decay rate in a homogeneous medium:[(5)]

$$\gamma_{hom} = \frac{\pi d^2 \omega_d}{\hbar \epsilon_0} N(\omega_d) = \frac{n d^2 \omega_d^3}{3\pi\hbar\epsilon_0 c^3}. \tag{2.38}$$

As we can see in Eq. 2.38, the decay rate depends linearly on the refractive index of the environment and increases as the cube of the transition frequency.

Let us now consider the Lamb shift Δ given by Eq. 2.33. Similarly to the decay rate γ, the Lamb shift depends on the transition dipole moment d and the LDOS $N(\mathbf{r}, \omega, \mathbf{e}_d)$. The integrand in Eq. 2.33 is proportional to ω^2 for large frequencies, and hence, the integral

(5) Here we assumed that the emitter has the same refractive index as the host medium, which gave us a simple relation between decay in a medium and vacuum: $\gamma_{hom} = n\gamma_{hom}^{vac}$. However, it is not always the case, especially for quantum dots: more complicated factors relate the decay rates in a dielectric to those in vacuum. For details see, *e.g.*, Refs. [6–8].

diverges leading to infinite values for the shift of the transition frequency. The divergence in the shift Δ is overcome by using a technique called *mass renormalization* suggested by Bethe [9]: due to the interaction with the vacuum fields, the effective mass of the electron is different from the mass of the electron which does not feel any fields. In addition to this technique, a cut-off of the integration range at high frequencies must be introduced to remove the divergence, which leads to accurate estimations of the shift of the transition frequency [2]. The calculated value of the Lamb shift in vacuum is $\sim 10^{-7}\omega_d$ [10]. In cases when the LDOS is strongly enhanced, the Lamb shift is about $10^{-6}\omega_d$: an order of magnitude larger than the vacuum Lamb shift [11]. Because these modifications are still much smaller than the homogeneous linewidth of available emitters as will be seen below, investigations of the frequency shift are not performed in this thesis.

Let us now summarize the approximations and assumptions that we used to derive the expression for the time-evolution of the atomic exited state:

a. The electric-dipole approximation to evaluate the electric-field operator $\mathbf{E}(\mathbf{r})$.

b. The perturbation approach to describe the time evolution of the atom-field system.

c. The rotating-wave approximation to neglect the rapidly-changing counter-rotating terms.

d. The dielectric function $\epsilon(\mathbf{r})$ is real to define the LDOS $N(\mathbf{r}, \omega, \mathbf{e}_d)$.

e. The atom-field interaction is considered as a *Markovian* process to solve the integro-differential Equation 2.28.

Possibilities to modify the rates of spontaneous emission from emitters at fixed frequencies ω have been attracting much interest after Purcell [12] originally recognized that the rate γ is increased if the emitter is placed in a cavity tuned to the emitter transition frequency. The rate γ can be also decreased by detuning the cavity, see [13–15]. The effect of the cavity consists in enhancing or inhibiting the vacuum-field fluctuations. Modified rates of spontaneous emission were also demonstrated by placing an emitter near a reflecting interface, see *e.g.* [16, 17]. However, ultimate modifications of the spontaneous emission in large volumes can be achieved in media with frequency bands free from electromagnetic fluctuations, as was suggested by Bykov [18]. We will see in the following section that periodic dielectric photonic structures are an ideal example of such media.

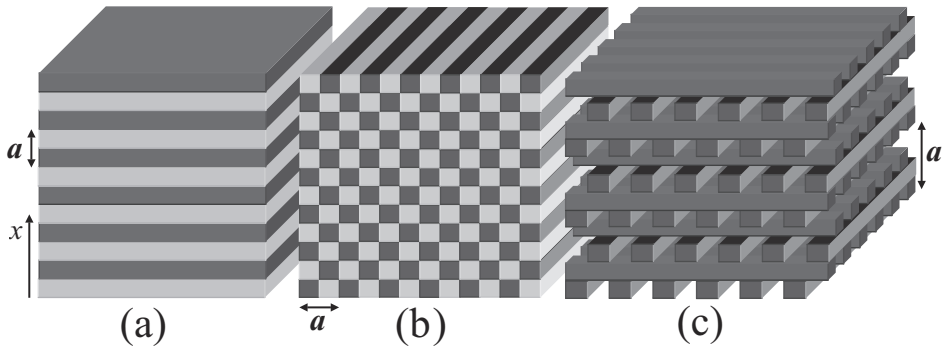

FIGURE 2.2: Schematic illustration of one (a), two (b) and three (c) dimensional (1D, 2D and 3D) periodic structures. Such structures are called photonic crystals, if their periodicity is comparable to the wavelength of light. Symbols a represent the sizes of the crystal unit cells.

2.2 Dispersion of light in periodic structures, photonic bands

Materials with periodic variations of the dielectric function on length scales comparable to the wavelength of light are called *photonic crystals* (see Figure 2.2). These dielectric composites are very attractive for scientists and engineers because they offer exciting ways to manipulate photons [19, 20]. The spatial variations of the dielectric function cause scattering of light. If these variations are periodic on lengthscales comparable to the wavelength of light, then the interference of the scattered light leads to optical Bragg diffraction: frequency windows, called stopbands, appear in which there are no field modes for certain propagation directions. Of even greater interest are three-dimensional (3D) photonic crystals possessing a photonic bandgap - a frequency range where no field modes exist at all. In two pioneering works, which started the field of photonic crystals in 1987, E. Yablonovitch and S. John pointed out the potential of photonic bandgap materials in inhibition of spontaneous emission and light localization [21, 22].

2.2.1 Wave equation in periodic dielectric media

In order to understand the interaction of electromagnetic waves with photonic crystals, we need to discuss the Maxwell equations. In a medium without charges and currents, the

propagation of light is governed by these four equations:

$$\begin{aligned} \nabla \times \mathbf{E} &= -\frac{\partial \mathbf{B}}{\partial t}, \qquad \nabla \cdot \mathbf{D} = 0, \\ \nabla \times \mathbf{H} &= \frac{\partial \mathbf{D}}{\partial t}, \qquad \nabla \cdot \mathbf{B} = 0, \end{aligned} \tag{2.39}$$

where $\mathbf{E}$ and $\mathbf{H}$ are the electric and magnetic fields, $\mathbf{D}$ and $\mathbf{B}$ are the displacement and magnetic-induction fields. The field $\mathbf{E}$ is related to $\mathbf{D}$ by a constitutive relation, and the same holds for the fields $\mathbf{H}$ and $\mathbf{B}$. The relations between the fields are equal to

$$\begin{aligned} \mathbf{D}(\mathbf{r}) &= \epsilon_0 \epsilon(\mathbf{r}) \mathbf{E}(\mathbf{r}), \\ \mathbf{B}(\mathbf{r}) &= \mu_0 \mathbf{H}(\mathbf{r}). \end{aligned} \tag{2.40}$$

Here $\epsilon(\mathbf{r})$ is a real and frequency independent function within the frequency range of interest. The spatial variation of the dielectric function obeys the periodicity of the photonic crystal, so that $\epsilon(\mathbf{r}) = \epsilon(\mathbf{r} + \mathbf{R})$ for all crystal lattice vectors $\mathbf{R}$. Fields $\mathbf{E}(\mathbf{r})$ and $\mathbf{H}(\mathbf{r})$ can both have complicated temporal and spatial dependencies, yet we can always expand the fields into a series of harmonic modes because of the linearity of the Maxwell equations. Therefore, assuming harmonic dependencies of the $\mathbf{E}(\mathbf{r})$ and $\mathbf{H}(\mathbf{r})$ fields with temporal frequency ω and reminding ourselves that $\epsilon_0 \mu_0 = c^{-2}$, we combine Eqs. 2.39 and 2.40 into the wave equations:

$$\nabla \times [\nabla \times \mathbf{E}(\mathbf{r})] = \epsilon(\mathbf{r}) \frac{\omega^2}{c^2} \mathbf{E}(\mathbf{r}) \quad \text{and} \tag{2.41}$$

$$\nabla \times \left[\epsilon(\mathbf{r})^{-1} \nabla \times \mathbf{H}(\mathbf{r}) \right] = \frac{\omega^2}{c^2} \mathbf{H}(\mathbf{r}). \tag{2.42}$$

These wave equations together with the divergence equations in (2.39) completely determine $\mathbf{E}(\mathbf{r})$ and $\mathbf{H}(\mathbf{r})$. In order to find the field modes at a certain frequency for a given by the photonic crystal $\epsilon(\mathbf{r})$, one needs to solve these complicated differential equations. The situation is called an *eigenvalue problem*: a series of operations is performed on a function, say, $\mathbf{E}(\mathbf{r})$, and if $\mathbf{E}(\mathbf{r})$ is an allowed field mode, the result is the original function $\mathbf{E}(\mathbf{r})$ multiplied by a constant called *eigenvalue*. For nonmagnetic materials, it is more convenient to solve the wave equation for $\mathbf{H}(\mathbf{r})$ field because the operator $\nabla \times \epsilon(\mathbf{r})^{-1} \nabla \times$ is Hermitian, and consequently all its eigenvalues ω^2/c^2 are real [19].

Because of the periodic dielectric function $\epsilon(\mathbf{r})$ in photonic crystals, the field modes of the eigenvalue problem Eq. 2.42 should satisfy the Bloch theorem [23]:

$$\mathbf{H}_\mathbf{k}(\mathbf{r}) = e^{i\mathbf{k}\cdot\mathbf{r}} \mathbf{u}_\mathbf{k}(\mathbf{r}). \tag{2.43}$$

These Bloch modes are fully described by the wavevector $\mathbf{k}$ and the periodic function $\mathbf{u_k}(\mathbf{r})$, which has the periodicity of the crystal lattice so that $\mathbf{u_k}(\mathbf{r}) = \mathbf{u_k}(\mathbf{r} + \mathbf{R})$. To solve Eq. 2.42, the inverse dielectric function and the Bloch modes are expanded in a Fourier series over the reciprocal-lattice vectors $\mathbf{G}$:

$$\epsilon(\mathbf{r})^{-1} = \eta(\mathbf{r}) = \sum_{\mathbf{G}} \eta_{\mathbf{G}} e^{i\mathbf{G}\cdot\mathbf{r}} \quad \text{and} \quad \mathbf{H_k}(\mathbf{r}) = \sum_{\mathbf{G}} \mathbf{u}_{\mathbf{k},\mathbf{G}} e^{i(\mathbf{k}+\mathbf{G})\cdot\mathbf{r}}. \tag{2.44}$$

Substituting these expressions into the H-field wave equation in Eq. 2.42, we obtain a linear set of eigenvalue equations:

$$-\sum_{\mathbf{G}'} \eta_{\mathbf{G}-\mathbf{G}'}(\mathbf{k}+\mathbf{G}) \times [(\mathbf{k}+\mathbf{G}') \times \mathbf{u}_{\mathbf{k},\mathbf{G}'}] = \frac{{\omega_\mathbf{k}}^2}{c^2} \mathbf{u}_{\mathbf{k},\mathbf{G}}, \quad \forall \mathbf{G}. \tag{2.45}$$

This infinite equation set with the known parameters $\mathbf{G}$ and $\eta_{\mathbf{G}-\mathbf{G}'}$ determines all allowed frequencies $\omega_\mathbf{k}$ for each value of the wave vector $\mathbf{k}$, subject to the transversality requirement $\nabla \cdot \mathbf{H_k}(\mathbf{r}) = 0$. Due to the periodicity of $\mathbf{u_k}(\mathbf{r})$, we can restrict $\mathbf{k}$ to the first Brillouin zone. Therefore, for every vector $\mathbf{k}$, there is an infinite number of modes with discretely spaced frequencies. All the modes are labeled with the band number n in order of increasing frequency and described as a family of continuous functions, $\omega_n(\mathbf{k})$. The information borne by these functions is called the *photonic band structure*. Knowledge of the band structure of a photonic crystal gives practically all the information on how the crystal interacts with electromagnetic waves. Therefore, the search for the structures with photonic bandgaps has raised a great interest in solving the photonic band-structure problem [19]. The eigenvalues $\omega_n(\mathbf{k})$ can be approximated if the infinite equation set in Eq. 2.45 is reduced by truncating the set the reciprocal lattice vectors. This truncation is quite a difficult task because of the poor convergence of the Fourier transform of the sharply varying dielectric function [24]. Numerical methods to determine the components of the truncated Fourier transforms and to resolve the eigenmatrices are described in Refs. [24–27]. The expansion of the dielectric function assumes infinitely extending perfect periodic structures. Nevertheless, this approach known as the H-field plane-wave method, is widely used due to its principal simplicity and applicability to a great variety of 3D periodic structures. The plane-wave method results in good approximations to the dispersion relation in real periodic structures: calculated photonic band structures are found to correspond to reflection and transmission experiments on photonic crystals.

2.2.2 1D photonic crystal, origin of photonic stopgap

As an example, we will now resolve the H-field wave equation set for the two lowest bands of the simplest case of photonic crystals: a 1D periodic structure (see Figure 2.2a). We consider a multilayered structure consisting of materials with different dielectric functions alternating with the period a. The structure is infinite and periodic in the x-direction and homogeneous in the other two directions. We also consider the light propagating in the x-direction. The dielectric function can be written as

$$\epsilon(x) = \epsilon_1 + (\epsilon_2 - \epsilon_1) f(x), \tag{2.46}$$

where *f(x)* equals 0 or 1, depending on whether x is inside the region of ϵ_1 or ϵ_2. Since we consider only low-energy bands, we take into account only two dominant reciprocal-lattice vectors: $G = 0$ and $G = 1$ in units of $2\pi/a$. The Fourier components of the inverse dielectric function are equal to

$$\eta_G = \frac{1}{a} \int_{-a/2}^{a/2} \epsilon(x)^{-1} e^{-iGx} dx. \tag{2.47}$$

The field modes in the Bloch form are:

$$H_{n,k}(x) = e^{-iGx} u_{n,k}(x), \tag{2.48}$$

where $u_{n,k}(x) = u_{n,k}(x + X)$ whenever X is an integer multiple of the period a. The Fourier components of $u_{n,k}(x)$ for $G = 0$ and 1 are denoted as u_0 and u_1, respectively. The equation set Eq. 2.45 then becomes:[6]

$$\begin{aligned} \frac{\omega_n(k)^2}{c^2} u_0 &= \eta_0 k^2 u_0 + \eta_1 k(k+1) u_1, \\ \frac{\omega_n(k)^2}{c^2} u_1 &= \eta_{-1} k(k+1) u_0 + \eta_0 (k+1)^2 u_1. \end{aligned} \tag{2.49}$$

This equation set yields a quadratic equation for $\omega_n(k)^2/c^2$, two solutions of which are

$$\frac{\omega_n(k)^2}{c^2} = \frac{1}{2}\eta_0[k^2 + (k+1)^2] \pm \frac{1}{2}\left[\eta_0^2[k^2 - (k+1)^2]^2 + 4\eta_{-1}\eta_1 k^2 (k+1)^2\right]^{1/2}. \tag{2.50}$$

Here we should bear in mind that k and G have opposite signs, so that if $k > 0$ then $G =$ -1.[7] Next, we substitute expressions for η_G, namely $\eta_0 = \frac{1}{2}(\epsilon_1^{-1} + \epsilon_2^{-1})$ and $\eta_1 = \eta_{-1} = \frac{1}{\pi}(\epsilon_2^{-1} - \epsilon_1^{-1})$, and plot the resulting $\omega_n(k)$.

[6] Note that in Eq. 2.45 the double vector product $(\mathbf{k} + \mathbf{G}) \times [(\mathbf{k} + \mathbf{G}) \times \mathbf{u}_{\mathbf{k},\mathbf{G}}]$ is antiparallel to $\mathbf{u}_{\mathbf{k},\mathbf{G}}$, which therefore compensates the "-" sign in front of the sum.

[7] Due to the Bragg condition $\mathbf{k}_{in} + \mathbf{G} = \mathbf{k}_{out}$ and the momentum conservation $|\mathbf{k}_{out}| = |\mathbf{k}_{in}|$, the projection of $\mathbf{k}_{in}$ on $\mathbf{G}$ is opposite to $\mathbf{G}$. Here, $\mathbf{k}_{in}$ and $\mathbf{k}_{out}$ are wavevectors of incident and Bragg diffracted waves, respectively.

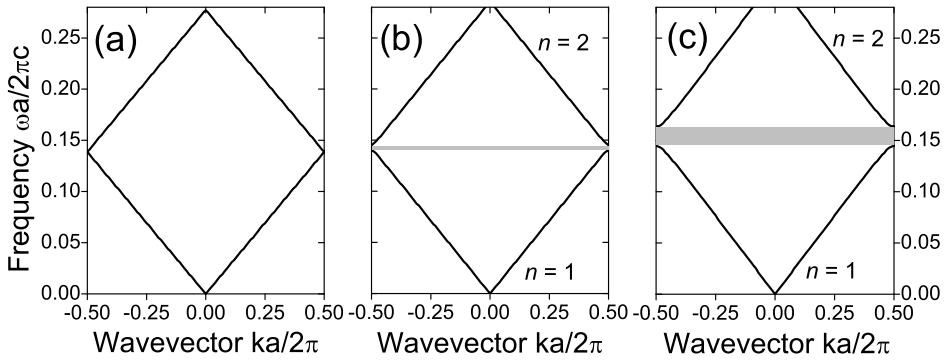

FIGURE 2.3: Photonic band structures for light propagating along the axis of a 1D periodic structure consisting of alternating layers of width $0.5a$ with the dielectric function: (a) $\epsilon_1 = \epsilon_2 = 13$, (b) $\epsilon_1 = 13$ and $\epsilon_2 = 11.6$, and (c) $\epsilon_1 = 13$ and $\epsilon_2 = 8.8$.

Figure 2.3 shows $\omega_n(k)$ for a 1D periodic structure with three different amplitudes of the periodic function $\epsilon(x)$. The plot in Figure 2.3a is for the structure in which all dielectric layers have the same $\epsilon(x) = 13$,[(8)] and the periodicity a is purely fictitious. The resulting k-dependence of the frequency is simply a straight line given by

$$\omega(k) = ck/\sqrt{\epsilon}. \tag{2.51}$$

Because we have restricted k to the first Brillouin zone $[-\frac{\pi}{a}, \frac{\pi}{a}]$, the line folds back into the zone when it reaches the edges. Figure 2.3b is for a multilayer structure where $\epsilon(x)$ of the layers slightly varies. It looks similar to that in Figure 2.3a, but with one important peculiarity: near reduced frequency of 0.14, it reveals a narrow frequency range, in which Eq. 2.50 has no real solutions. At the zone edges, $k = \pm\frac{1}{2}G$, the incident and diffracted waves form standing waves with a wavelength $\lambda = 2a$. Since the standing waves should also satisfy the Bloch theorem, there are only two ways to position them. The first standing wave has its extrema in the centers of the layers with ϵ_1, and the other one, in the centers of the layers with ϵ_2. The wavelengths of these waves are still the same, but they experience different ϵ, therefore their frequencies ω_1 and ω_2 are different. Consequently, there appears a spatial and frequency separation of the two modes with the zone-edge k-vector, which leads to a splitting of the photonic bands $n = 1$ and 2. The frequency range between ω_2 and ω_1 contains no modes for the crystal and is often called a *photonic*

[(8)] For this example we have taken specific values of ϵ for materials used in multilayer devices: $\epsilon \approx 13$, 11.6 and 8.8 are values of the dielectric functions of GaAs, GaAlAs and AlAs, respectively, at $\lambda = 900$ nm.

bandgap. We emphasize here that we shall reserve the term *photonic bandgap* for situations when no modes exist for wave propagation in *all* directions in the 3D space. When a gap in the dispersion occurs only along a certain propagation direction, it will be called a *stopgap*.

As shown in Figure 2.3c, with increasing dielectric contrast, the splitting, *i.e.*, the stop-gap width becomes noticeably larger. The width of the stopgap is determined by the photonic strength S that is a gauge for the interaction between light and a photonic crystal [28]. It can be readily derived from Eq. 2.50 that at $k = \pm\frac{1}{2}G$ the photonic strength S, the relative width of the stopgap, equals

$$S = \Delta\omega/\omega_c = \sqrt{1+\eta_1/\eta_0} - \sqrt{1-\eta_1/\eta_0} \approx \frac{\eta_1}{\eta_0} = \frac{2}{\pi}\frac{|\epsilon_1-\epsilon_2|}{\epsilon_1+\epsilon_2}. \tag{2.52}$$

We can see that S is proportional to the ratio of the dielectric contrast and the geometrically averaged dielectric function. The photonic strength S can be enhanced by optimizing the geometry of the periodic structure: by optimizing the Fourier components of the inverse dielectric function, minimizing η_0 and enhancing η_1. Eq. 2.52 is also valid for 2D and 3D photonic crystals for low-order stopgaps when only two reciprocal-lattice vectors are involved. Large photonic strength S is crucial for opening photonic bandgaps. The larger the strengths S, the wider the stopgaps, and in a 3D photonic crystal with wide stopbands, simultaneous diffraction on different crystal-lattice planes can result in an omnidirectional stopgap: a photonic bandgap.

2.2.3 Dispersion relation in 3D, photonic bandgap

We shall now discuss photonic dispersion in structures where the dielectric function $\epsilon(\mathbf{r})$ is periodic in the three directions, *e.g.*, shown in Figure 2.2c. Such 3D photonic crystals are much more important than 1D and 2D ones because only they can possess a photonic bandgap, which is essential for light localization and ultimate suppression of spontaneous emission. The importance of 3D light confinement can be seen in the example of an emitter interacting with a continuum of the field modes. Indeed, the emitter will always interact with all field modes of its 3D environment, and therefore, no radical suppression of spontaneous emission is possible if the modes in only, say, 2 dimensions are eliminated by a 2D "bandgap". For this advantageous property of 3D photonic crystals, a special price must be paid: fabrication of 3D periodic structures with high photonic strengths is quite a complicated task [20, 29]. An example of 3D photonic crystals that can be relatively easy

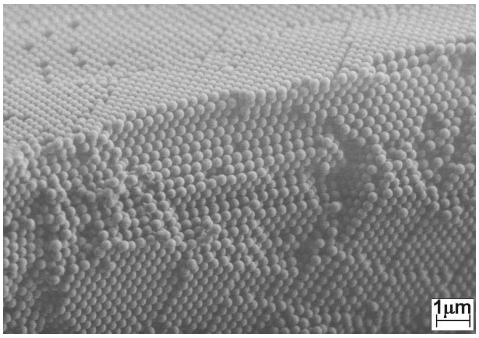

FIGURE 2.4: Electron microscopy image of a polystyrene opal - a 3D colloidal crystal built from polystyrene spheres close-packed in the fcc lattice. Image courtesy of N. Dziomkina.

fabricated in a large scale, is an opal-like structure made by self-assembly of dielectric spheres into the close-packed *fcc* lattice, shown in Figure 2.4. As discussed above, a large photonic strength S requires a high dielectric contrast and a low volume-averaged dielectric function. Therefore, the inverse opals [30–32], *fcc* lattices of close-packed air spheres in the backbone from a material with high ϵ, fulfil these requirements and are suitable for the confinement of light in 3D. For this reason we will discuss in detail interaction of light with an inverse-opal photonic crystal consisting of air spheres and shells from gallium phosphide (GaP). In practice, it is rather difficult to infiltrate opals with GaP, and also with other III-V semiconductors such as InP and GaAs [33, 34]. Nevertheless, GaP has the highest dielectric function in the visible range: $\epsilon \approx 11$ at $\lambda = 600$ nm [35];[(9)] which makes this semiconductor very attractive for photonic applications requiring manipulation with visible light. Therefore, we will consider a calculated photonic band structure for an inverse opal consisting of air spheres covered by dielectric shells with $\epsilon = 11$.

To obtain the dispersion relation for 3D periodic structures, we have solved the eigenvalue problem in Eq. 2.45, similarly to the 1D example, but we must take into account more than just two reciprocal-lattice vectors $\boldsymbol{G}$. First, let us consider a simple case: a photonic band structure for an inverse opal with no dielectric contrast. Absence of the dielectric contrast means that all non-diagonal elements of the eigenvalue matrix are zeros. In Figure 2.5a, we plot the dispersion for an *fcc* periodic structure, in which both dielectrics have $\epsilon = 11$. The frequencies are plotted along lines in the first Brillouin zone

[(9)] The bandgap energy of GaP is 2.24 eV, hence the material does not absorb down to $\lambda \approx 550$ nm.

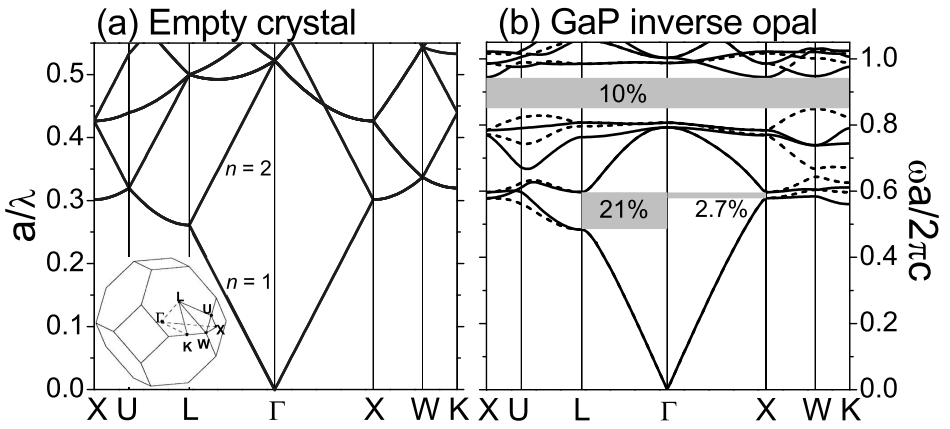

FIGURE 2.5: Calculated photonic band structure for an *fcc* lattice plotted along lines connecting points Γ(k = 0), L, X, U, W, K (see the inset). The wavevector varies across the irreducible Brillouin zone, along the trajectories Γ → L → U → X and Γ → X → W → K. The 3D lattice consists of close-packed spheres ($r = 0.25\sqrt{2}a$, a - cubic lattice parameter) from a dielectric with ϵ_1, surrounded by spherical shells ($1.25r$) from a dielectric with ϵ_2. (a) $\epsilon_1 = \epsilon_2 = 11$ (bulk "GaP", fictitious periodicity). (b) $\epsilon_1 = 1$ and $\epsilon_2 = 11$ (air spheres surrounded by "GaP" shells). Solid curves are for *s*-polarization, and dashed curves are for *p*-polarization. Grey rectangles indicate directions and widths of stopgaps and a bandgap. The calculations were done with a basis of 725 plane waves.

joining high-symmetry points Γ, L, X, U, W, K (see the inset in Fig. 2.5a) that correspond to $(0,0,0)$, $(\frac{1}{2},\frac{1}{2},\frac{1}{2})$, $(1,0,0)$, $(1,\frac{1}{4},\frac{1}{4})$, $(1,\frac{1}{2},0)$ and $(\frac{3}{4},\frac{3}{4},0)$, in units of $2\pi/a$. These lines bound the irreducible part of the Brillouin zone. Because all k-points have their symmetry equivalents in the irreducible Brillouin zone, and the bands have their maxima (or minima) on the high-symmetry lines at surface of the Brillouin zone, it is sufficient to plot the dispersion relation along those lines only. If we consider band 1, we will see that starting from the Γ point the frequency increases linearly with the wavevector with the slope determined by $\omega_1(k) = ck/\sqrt{11}$ similar to the 1D case. After band 1 has reached the L point and moves along the LU line, the frequency change seems to be non-linear. It is merely because the frequency there is proportional to the square of the length of the wavevector along the LU line. The frequency in the other bands behaves in the same way. The higher bands can also be seen as linear functions of the k-vector, which originates at point Γ and moves along the trajectories beyond the first Brillouin zone. For example, for band 2, the

tip of the k-vector goes from the X point via U to L in the same way as for band 1, but then it slides away along the ΓL line toward point Γ of a neighboring Brillouin zone. Because the number of G-vectors, *i.e.*, the number of crystal planes increases quadratically with length of the k-vector, the bands become more densely spaced at higher frequencies. It should be also mentioned that the bands have a double degeneration because the two polarization states are indistinguishable for this empty crystal.

The photonic dispersion changes radically when the dielectric contrast is increased. Figure 2.5b shows the calculated band structure for the inverse opal that consists of air spheres ($\epsilon = 1$) and shells from a dielectric with $\epsilon = 11$. The band structure reveals a wide band splitting in the ΓL direction that corresponds to light diffraction on the (111) set of crystal-lattice planes. This is the lowest-frequency stopgap since ΓL is the shortest path to the surface of the Brillouin zone. Consequently, light at frequencies within this gap and wavevectors $\mathbf{k}_{in}$ parallel to reciprocal-lattice vectors $\mathbf{G}_{111}$ cannot propagate in the crystal. The stopgap shifts to higher frequencies when the angle between $\mathbf{k}_{in}$ and $\mathbf{G}_{111}$ increases. On the opposite side of the diagram, at the point X, we see another stopgap, corresponding to diffraction on the (200) set of lattice planes - the other Bragg plane contouring the first *fcc* Brillouin zone. This stopgap is narrow due to a lower photonic strength *S*: modulation of $\epsilon(\mathbf{r})$ is not optimal in this direction.

In Figure 2.5b we can see that the bands in the LUX and XWK planes are different for waves with mutually orthogonal *p* and *s* polarizations (solid and dashed curves, respectively).[(10)] Because bands 3 and 4 are degenerate at the point W [25], and bands 2 and 3 cross each other near the point U, there is no complete overlap between these (111) and (200) stopgaps. Therefore, no photonic bandgap can be opened at these frequencies for any dielectric contrasts. At frequencies around $a/\lambda = 0.9$, the band diagram reveals a frequency range with no modes for all k-points - a photonic bandgap. Propagation of waves at these frequencies is forbidden irrespective of direction. The bandgap is not only an omnidirectional overlap of stopgaps associated with diffraction on higher-order lattice planes but also a multiple diffraction, *i.e.*, simultaneous coupling of waves with certain k-vectors to many G-vectors [36]. When going back to low frequencies, we can see that the dispersion is linear with the slope determined by the volume-averaged dielectric function. Thus at the low-frequency limit, *i.e*, at long wavelengths compared to the lattice spacing *a*, the light "sees" the crystal as a homogeneous medium.

[(10)] Waves propagating along the ΓX line, *i.e.*, in [100] direction, are *p*-polarized when **E** vector lies in the plane of incidence. When **E** is perpendicular to the incident plane, the wave is *s*-polarized.

In this example, the photon band structure was calculated for a fixed dielectric contrast. This means that the variation of the reduced frequency a/λ is determined only by the change of the lattice parameter a. However, for a specific photonic crystal, one is often interested to know the band structure for a fixed lattice parameter but varying optical frequency ω. In that case, due to possible dispersion of the dielectric function $\epsilon(\omega)$ of the materials constituting the photonic crystal, the dielectric contrast becomes a function of the reduced frequency a/λ.

2.3 Local density of states in photonic crystals

In Section 2.1 (Eq. 2.27) we introduced the local radiative density of electromagnetic states (LDOS). We have already seen in Eq. 2.31 that the radiative rate of spontaneous emission is determined by the LDOS at the emission frequency, projected on the orientation of the transition dipole. Now, by a simple example of a single mode in a cavity, let us first consider the dependence of the LDOS on the profile and orientation of the field mode relative to the emitting dipole. In Figure 2.6a we plotted a field mode $\Lambda_y(x)$ with the Gaussian profile in a cavity with $\epsilon = 1$, which confines light along the x-direction. The field in the mode is polarized in the xy plane and has the wavelength $\lambda = 2\pi c/\omega_d$, where ω_d is the dipole transition frequency. For this single mode, the expression for the LDOS (Eq. 2.27) becomes

$$N_{yy}(x) = \frac{1}{(2\pi)^3}|\mathrm{e}_{d,y}\Lambda_y(x)|^2, \tag{2.53}$$

where $\mathrm{e}_{d,y}$ is a projection of the dipole orientation $\mathbf{e}_d$ on the y-axis. In Figure 2.6b we show the resulting LDOS as a function of the location in the cavity. We see that the density of the mode has maxima and minima which resemble the extrema of the field $\Lambda_y(x)$. For dipoles oriented perpendicularly to the y-axis, the LDOS is zero: such dipoles can not couple to the mode $\Lambda_y(x)$. By this simple example of a single mode, we have demonstrated that the LDOS strongly depends on the location and orientation of the emitting dipole.

Let us now turn our attention to photonic crystals. In the previous section we have seen that interference of scattered waves in photonic crystals strongly modifies propagation of light. We can predict the effect of an infinite photonic crystal by solving the H-field wave equation set in Eq. 2.45 for a given $\epsilon(\mathbf{r})$. Knowing the eigenmodes of the photonic crystal, we can also calculate effects on the radiation dynamics of embedded light sources. In a

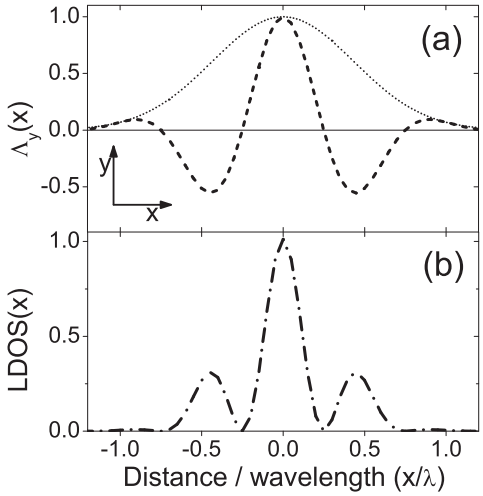

FIGURE 2.6: (a) Cavity field mode $\Lambda_y(x)$ with a Gaussian profile (dotted curve) normalized to its maximum. (b) The density of the mode $\Lambda_y(x)$ normalized to its maximum for a dipole oriented in *y*-direction.

photonic crystal, the eigenmodes $\mathbf{E}_{n,\mathbf{k}}(\mathbf{r}) = \mathbf{\Lambda}_{n,\mathbf{k}}(\mathbf{r})/\sqrt{\epsilon(\mathbf{r})}$ [(11)] are Bloch functions, so that the expression for the LDOS in Eq. 2.27 becomes

$$N(\mathbf{r},\omega,\mathbf{e}_d) = \frac{1}{(2\pi)^3}\sum_n \int_{BZ} d\mathbf{k}\delta(\omega-\omega_{n,\mathbf{k}})|\mathbf{e}_d\cdot\mathbf{E}_{n,\mathbf{k}}(\mathbf{r})|^2, \tag{2.54}$$

where n is the band index. Very often, one studies spontaneous emission from a collection of atoms with randomly-oriented transition dipole moments. In this case, the dipole orientation $\mathbf{e}_d$ is averaged over all solid angles, which results in

$$N(\mathbf{r},\omega) = \frac{1}{6\pi^2}\sum_n \int_{BZ} d\mathbf{k}\delta(\omega-\omega_{n,\mathbf{k}})|\mathbf{E}_{n,\mathbf{k}}(\mathbf{r})|^2. \tag{2.55}$$

Further, in order to describe emission dynamics of atoms randomly distributed in the photonic-crystal unit cell, the LDOS can be integrated over the unit cell:

$$N_{av}(\omega) = \int_{WSC} d\mathbf{r}\rho(\mathbf{r})N(\mathbf{r},\omega), \tag{2.56}$$

where $\rho(\mathbf{r})$ is a density of atoms at certain points in the crystal. We should note here that in such experiments on ensembles of identical atoms in photonic crystals, the ob-

[(11)] The H-field plane-wave method results in the set of eigenmodes $\mathbf{H}_{n,\mathbf{k}}(\mathbf{r})$, which are related to $\mathbf{E}_{n,\mathbf{k}}(\mathbf{r})$ by the Maxwell equations in Eqs. 2.39.

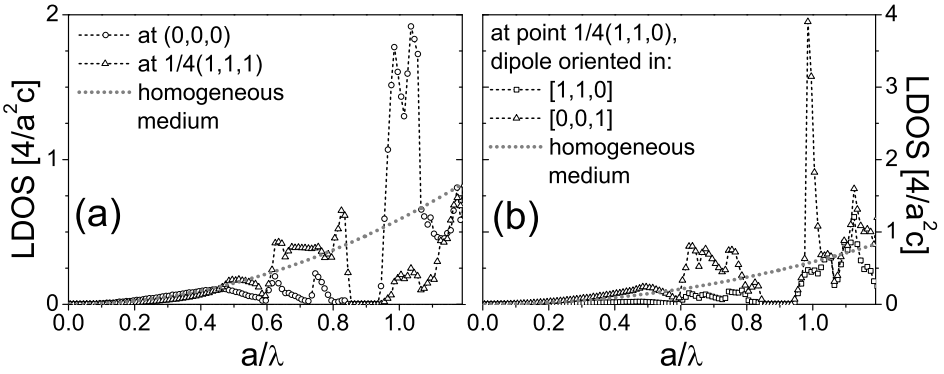

FIGURE 2.7: LDOS calculated with the plane-wave method in the same GaP inverse-opal photonic crystal as in the previous section. (a) LDOS at (0,0,0) [the center of an air sphere] and at $(\frac{1}{4}, \frac{1}{4}, \frac{1}{4})$ shown by connected circles and triangles, respectively. (b) LDOS at $(\frac{1}{4}, \frac{1}{4}, 0)$ [at the window between two air spheres] projected on [1,1,0] and [0,0,1] directions shown by connected squares and triangles, respectively. Dotted curves are for LDOS in a homogeneous medium with ϵ = 3.1. This value of ϵ corresponds to the unit-cell averaged dielectric function in the inverse opal.

served intensity of spontaneous emission does not decay in time as a single-exponential function, as one might naively think. The intensity decay in this case is a distribution of exponential decays, and the average rate constant of the distribution can be compared to that determined with the average LDOS in Eq. 2.56.

To examine the effects of photonic crystals on the LDOS and radiative dynamics of internal sources, we will consider the example of the GaP inverse-opal photonic crystal, whose dispersion relation was discussed in the previous section. In Figures 2.7a and 2.7b we show the LDOS at three different positions in the crystal unit cell: at points (0,0,0), $(\frac{1}{4}, \frac{1}{4}, \frac{1}{4})$ (a) and $(\frac{1}{4}, \frac{1}{4}, 0)$ (b). At the first two points, the LDOS does not depend on the dipole orientation $\mathbf{e}_d$ due to high symmetry, whereas at the third point, the LDOS is strongly orientation-dependent. At frequencies near the lowest-order stopgaps, $a/\lambda \approx 0.6$ [compare to Figure 2.5b], the Bloch modes are eliminated for k-vectors in a solid angle, which can occupy a considerable part of the whole 4π solid angle. This leads to decreased LDOS and spontaneous-emission rate γ, especially when the orientation of the transition dipole $\mathbf{e}_d$ and its position in the unit cell are not favorable for coupling to allowed Bloch modes. At frequencies in the photonic bandgap, $a/\lambda \approx 0.9$, there are no Bloch modes at all: the

LDOS is zero regardless the dipole orientation and position in the unit cell. Consequently, spontaneous emission from a dipole emitter vanishes completely. The decay of the excited state in this case can only occur via possible non-radiative channels and via weaker atom-field interaction processes, such as, *e.g.*, two-photon dipole-quadrupole processes [10]. On the other hand, at frequencies outside the bandgap, the density of Bloch modes is increased leading to enhanced radiative decay rates. Figure 2.7 reveals sharp peaks in the LDOS just above the bandgap, which are called *van Hove* singularities. In this situation, the Weisskopf-Wigner approximation does not hold, which means that the full equation of motion (Eq. 2.28) must be solved. Consequently, the emission decay of a single atom is not exponential as it is in media with smoothly varying LDOS. In several theoretical papers [11, 37–39], it was predicted that near the bandgap edge the decay of spontaneous emission is fractional and has an oscillatory behavior. As we have seen by this realistic example, the strong modification of the LDOS in photonic bandgap materials can lead to ultimate suppressions as well as enhancements of spontaneous emission.

The plane-wave method is a widespread technique to calculate eigenvalues and the local density of eigenmodes in infinite and perfectly-periodic 3D photonic crystals. To calculate the eigenmodes $\mathbf{E}_{\mathbf{k}}(\mathbf{r})$ for a finite structure or in a defect of a periodic structure, one has to use an expansion with an enormous number of plane waves, which therefore makes the task practically not realizable. An alternative approach is to find the LDOS via the Green's tensor $\mathbf{G}(\mathbf{r},\mathbf{r}',\omega)$, which represents the electric field at position $\mathbf{r}$ radiated by three orthogonal dipoles located at $\mathbf{r}'$ [40, 41]. For a scattering system described by dielectric function $\epsilon(\mathbf{r})$, $\mathbf{G}(\mathbf{r},\mathbf{r}',\omega)$ is a solution of the wave equation with a point source:

$$\nabla \times \left[\nabla \times \mathbf{G}(\mathbf{r},\mathbf{r}',\omega)\right] - \epsilon(\mathbf{r})\frac{\omega^2}{c^2}\mathbf{G}(\mathbf{r},\mathbf{r}',\omega) = -\mathbf{I}\delta(\mathbf{r}-\mathbf{r}'), \tag{2.57}$$

where $\mathbf{I}$ is the unitary matrix. Because $\mathbf{G}(\mathbf{r},\mathbf{r}',\omega)$ can be expressed in terms of the Bloch functions:

$$\mathbf{G}(\mathbf{r},\mathbf{r}',\omega) = \frac{c^2\epsilon(\mathbf{r}')}{\epsilon(\mathbf{r})}\sum_n \int_{BZ} d\mathbf{k}\frac{\mathbf{E}^*_{\mathbf{k}}(\mathbf{r}')\mathbf{E}_{\mathbf{k}}(\mathbf{r})}{\omega^2-\omega^2_{\mathbf{k}}}, \tag{2.58}$$

the LDOS can be inferred via evaluating the imaginary part of the Green's tensor when the source point $\mathbf{r}'$ coincides with $\mathbf{r}$:

$$N(\mathbf{r},\omega,\mathbf{e}_d) = -\frac{2\omega}{\pi c^2}\mathrm{Im}\{\mathbf{e}_d^T\cdot[\mathbf{G}(\mathbf{r},\mathbf{r},\omega)]\cdot\mathbf{e}_d\}. \tag{2.59}$$

The same can be done for the dipole-averaged LDOS:

$$N(\mathbf{r},\omega) = -\frac{2\omega}{\pi c^2}\mathrm{Im}\{\mathrm{Tr}[\mathbf{G}(\mathbf{r},\mathbf{r},\omega)]\}. \tag{2.60}$$

The obtained expressions for the projected and dipole-averaged LDOS yield the same results as Eqs. 2.54 and 2.55 that contain the Bloch functions. This approach is advantageous when it is difficult to find the set of Bloch functions. The Green's tensors can be readily calculated for finite structures with various geometries built from particles with known scattering properties, *e.g.*, spheres. Therefore, the Green's-tensor method is ideal for finite-sized opals or inverse opals with or without defects.

Modifications of the spontaneous-emission rates in finite 3D dielectric structures with arbitrary geometries can be inferred using the method of finite-difference time-domain (FDTD). The flexibility of this technique is paid by its computational complexity: the field across the whole structure is required to be evaluated for a single dipole orientation. This makes the method less effective for more-or-less large structures and for cavities where the waves travel for a long time. Nevertheless, the simulations reported in [42, 43] revealed that 3D crystallites built of only a few unit cells are enough for substantial modifications of the emission rates of embedded sources.

2.4 Conclusions

We have reviewed the quantum theory of light-matter interaction, which explains the relaxation process of the atomic excited state via emitting a photon. We have also discussed important approximations necessary to derive the analytic expression for the rate of spontaneous emission. Propagation electromagnetic waves in periodic dielectrics was studied. We explained the origin of the photonic band gap as well as the photonic dispersion relation in 3D photonic crystals. Based on the results from the H-field plane-wave method, we concluded that the LDOS can be radically modified in photonic crystals: the frequency dependence of the LDOS is noticeably different from that in homogeneous media. In addition, in photonic crystals, the LDOS, and therefore, the rate of spontaneous emission are the functions of position in the crystal unit-cell and orientation of the transition dipole moment.

References

[1] M. O. Scully and M. S. Zubairy, *Quantum Optics*, Cambridge University Press, (1997).

[2] P. W. Milonni, *The Quantum Vacuum: an Introduction to Quantum Electrodynamics*, Academic Press, Boston, (1994).

[3] L. Allen and J. H. Eberly, *Optical Resonance and Two-Level Atoms*, Dover Publications, New-York, (1987).

[4] R. Sprik, B. A. van Tiggelen and A. Lagendijk, *Optical Emission in Periodic Dielectrics*, Europhys. Lett. **35**, 265 (1996).

[5] A. Lagendijk, *Vibrational Relaxation Studied with Light*, in: *Ultrashort Processes in Condensed Matter*, 197-238, Edited by W. E. Bron, Plenum, New York, (1993).

[6] S. M. Barnett, B. Hutter, R. Loudon and R. Matloob, *Decay of Excited Atoms in Absorbing Dielectrics*, J. Phys. B: At. Mol. Opt. Phys. **29**, 3763 (1996), and references therein.

[7] F.J.P. Schuurmans, *Light in Complex Dielectrics*, Ph.D. thesis, University of Amsterdam, ISBN: 90-577-6032-0 (1999).

[8] A. Thränhardt, C. Ell, G. Khitrova and H. M. Gibbs, *Relation between Dipole Moment and Radiative Lifetime in Interface Fluctuation Quantum Dots*, Phys. Rev. B **65**, 035327 (2002).

[9] H. A. Bethe, *The Electromagnetic Shift of Energy Levels*, Phys. Rev. **72**, 339 (1947).

[10] S. John and J. Wang, *Quantum Optics of Localized Light in a Photonic Band Gap*, Phys. Rev. B **43**, 12772 (1991).

[11] N. Vats, S. John and K. Busch, *Theory of Fluorescence in Photonic Crystals*, Phys. Rev. A **65**, 043808 (2002).

[12] E. M. Purcell, *Spontaneous Emission Probabilities at Radio Frequencies*, Phys. Rev. **69**, 681 (1946).

[13] D. Kleppner, *Inhibited Spontaneous Emission*, Phys. Rev. Lett. **47**, 233 (1981).

[14] R. G. Hulet, E. S. Hilfer and D. Kleppner, *Inhibited Spontaneous Emission by a Rydberg Atom*, Phys. Rev. Lett. **55**, 2137 (1985).

[15] M. Bayer, T. L. Reinecke, F. Weidner, A. Larionov, A. McDonald and A. Forchel, *Inhibition and Enhancement of the Spontaneous Emission of Quantum Dots in Structured Microresonators*, Phys. Rev. Lett. **86**, 3168 (2001).

[16] K. H. Drexhage, *Influence of a Dielectric Interface on Fluorescence Decay Time*, J. Lumin. **1**, 693 (1970).

[17] E. Snoeks, A. Lagendijk and A. Polman, *Measuring and Modifying the Spontaneous Emission Rate of Erbium Near an Interface*, Phys. Rev. Lett. **74**, 2459 (1995).

[18] V. P. Bykov, *Spontaneous Emission in a Periodic Structure*, Sov. Phys. JETP **35**, 269 (1972); *Spontaneous Emission from a Medium with a Band Spectrum*, Sov. J. Quant. Electron. **4**, 861 (1975).

[19] J. D. Joannopoulos, R. D. Meade and J.N. Winn, *Photonic Crystals: Molding the Flow of Light*, Princenton University Press, (1995).

[20] C. M. Soukoulis, editor, *Photonic Crystals and Light Localization in the* 21^{st} *Century*, Kluwer, Dordrecht, (2001).

[21] E. Yablonovitch, *Inhibited Spontaneous Emission in Solid-State Physics and Electronics*, Phys. Rev. Lett. **58**, 2059 (1987).

[22] S. John, *Strong Localization of Photons in Certain Disordered Dielectric Superlattices*, Phys. Rev. Lett. **58**, 2486 (1987).

[23] N. W. Ashcroft and N. D. Mermin, *Solid State Physics* (Holt, Rinehart and Winston, New York, 1976).

[24] H. S. Sözüer, J. W. Haus and R. Inguva, *Photonic Bands: Convergence Problems with the Plane-Wave Method*, Phys. Rev. B **45**, 13962 (1992).

[25] K. M. Ho, C. T. Chan and C. M. Soukoulis, *Existence of a Photonic Gap in Periodic Dielectric Structures*, Phys. Rev. Lett. **65**, 3152 (1990).

[26] K. Busch and S. John, *Photonic Band Gap Formation in Certain Self-Organizing Systems*, Phys. Rev. E **58**, 3896 (1998).

[27] A. F. Koenderink, *Emission and Transport of Light in Photonic Crystals*, Ph.D. thesis, University of Amsterdam, ISBN: 90-9016903-2 (2003).

[28] W. L. Vos, R. Sprik, A. van Blaaderen, A. Imhof, A. Lagendijk and G. H. Wegdam, *Strong Effects of Photonic Band Structures on The Diffraction of Colloidal Crystals*, Phys. Rev. B. **53**, 16231 (1996).

[29] K. Busch, S. Lölkes, R. B. Wehrspohn and H. Föll, editors, *Photonic Crystals. Advances in Design, Fabrication, and Characterization*, WILEY-VCH Verlag GmbH & Co. KGaA, Weinheim, (2004).

[30] J.E.G.J. Wijnhoven and W. L. Vos, *Preparation of Photonic Crystals Made of Air Spheres in Titania*, Science **281**, 802804, (1998).

[31] A. Blanco, E. Chomski, S. Grabtchak, M. Ibisate, S. John, S. W. Leonard, C. López, F. Meseguer, H. Míguez, J. P. Mondia, G. A. Ozin, O. Toader and H. M. van Driel, *Large-Scale Synthesis of a Silicon Photonic Crystal with a Complete Three-Dimensional Bandgap Near 1.5 Micrometres*, Nature **405**, 437 (2000).

[32] Y. A. Vlasov, X. Z. Bo, J. C. Sturm and D. J. Norris, *On-Chip Natural Assembly of Silicon Photonic Bandgap Crystals*, Nature **414**, 289 (2001).

[33] Y. Lee, T. Kuo, C. Hsu, Y. Su and C. Chen, *Fabrication of 3D Macroporous Structures of II-VI and III-V Semiconductors Using Electrochemical Deposition*, Langmuir **18**, 9942 (2002).

[34] E. Palacios-Lidón, H. M. Yates, M. E. Pemble and C. López, *Photonic Band Gap Properties of GaP Opals with a New Topology*, Appl. Phys. B **81**, 205 (2005).

[35] D. F. Nelson and E. H. Turner, *Electro-optic and Piezoelectric Coefficients and Refractive Index of Gallium Phosphide*, J. Appl. Phys. **39**, 3337 (1968).

[36] H. M. van Driel and W. L. Vos, *Multiple Bragg Wave Coupling in Photonic Band-Gap Crystals*, Phys. Rev. B **62**, 9872 (2000).

[37] S. John and J. Wang, *Quantum Electrodynamics near a Photonic Band Gap: Photon Bound States and Dressed Atoms*, Phys. Rev. Lett. **64**, 2418 (1990).

[38] S. John and T. Quang, *Spontaneous Emission near the Edge of a Photonic Band Gap*, Phys. Rev. A **50**, 1764 (1994).

[39] K. Busch, N. Vats, S. John and B. C. Sanders, *Radiating Dipoles in Photonic Crystals*, Phys. Rev. E **62**, 4251 (2000).

[40] R. C. McPhedran, L. C. Botten, J. McOrist, A. A. Asatryan, C. M. de Sterke and N. A. Nicorovici, *Density of States Functions for Photonic Crystals*, Phys. Rev. E **69**, 16609 (2004).

[41] D. P. Fussell, R. C. McPhedran and C. M. de Sterke, *Three-Dimensional Green's Tensor, Local Density of States, and Spontaneous Emission in Finite Two-Dimensional Photonic Crystals Composed of Cylinders*, Phys. Rev. E **70**, 66608 (2004).

[42] C. Hermann and O. Hess, *Modified Spontaneous-Emission Rate in an Inverted-Opal Structure with Complete Photonic Bandgap*, J. Opt. Soc. Am. B **19**, 3013 (2002).

[43] J. S. Kole, *New Methods for the Numerical Solution of Maxwell's Equations*, Ph.D. thesis, University of Groningen, ISSN: 1570-1530 (2003).

CHAPTER 3

TOOLBOX FOR COMPLETE CONTROL OF SPONTANEOUS EMISSION

We discuss the necessary instruments to control the process of spontaneous emission of light. Photonic crystals are recognized as an ideal tool for radical suppression and also enhancement of spontaneous emission. The rate of spontaneous emission vanishes completely, and light is localized in defects inside photonic crystals with a photonic bandgap. We review the requirements on the crystal symmetry and the dielectric contrast for opening of the bandgap as well as the methods to fabricate such periodic structures on a large scale. Thereafter, optical probes necessary to investigate the interaction of light with real photonic crystals are discussed. These probes include measurements of angle-resolved spectra of reflected and transmitted light as well as emission from internal light sources, both angle- and time-resolved. We also consider the role of unavoidable structural disorder in light propagation through real photonic crystals. We give a detailed description of polystyrene opals and titania inverse opals - photonic crystals used in our emission experiments. Finally, we discuss light sources that can be used as internal fluorescent probes of photonic crystals.

3.1 Experimentally realized structures with photonic bandgaps

It is important to emphasize that photonic bandgaps do not appear in crystals with any lattice symmetry and any dielectric contrast. Existence of photonic bandgaps for reasonable dielectric contrasts were predicted only in a few structures: the diamond [1] and diamond-like structures [2], the so-called Yablonovite [3], the simple cubic (*sc*) structures [4], the face-centered-tetragonal "woodpile" structure [5] and the close-packed *fcc* and *hcp* structures [6]. For all these symmetries, a photonic bandgap appears if the dielectric contrast exceeds a certain threshold.

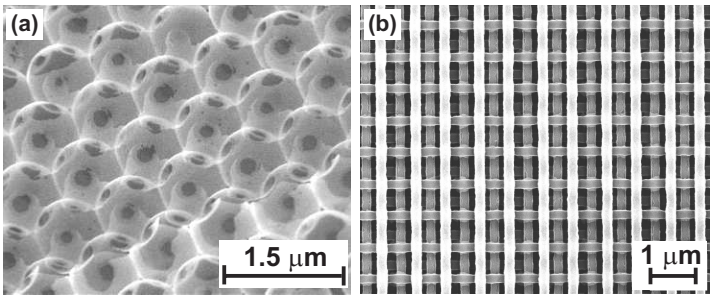

FIGURE 3.1: (a) Scanning electron microscopy (SEM) image of a silicon inverse opal (cut along (111) facet): the crystal consists of air-spheres packed in the fcc lattice and covered by silicon shells. The black holes are windows connecting the spheres. Image courtesy of A. Blanco [9]. (b) SEM image (top view) of a woodpile photonic crystal consisting of four layers of silicon rods. The structure was made by the layer-by-layer assembly described in [14].

We will first consider close-packed periodic structures with the *fcc* crystal symmetry, because they can be made relatively easy on the large scale using self-assembly methods [7–10]. An example of experimentally realizable photonic crystals that can possess a bandgap are silicon inverse opals, which have a refractive-index contrast of about 3.5 in the infrared range [9, 10]. Figure 3.1a shows an SEM image of such inverse-opal photonic crystal made from silicon. The drawback of the *fcc* periodicity is that the photonic bandgap in crystals with this lattice symmetry is caused by high-order diffraction. Consequently, the relevant Fourier components of ϵ are smaller than in the first-order diffraction leading to a narrower gap. For *fcc* photonic crystals built from air spheres, the refractive-index contrast ($\sqrt{\epsilon_1/\epsilon_2}$) should be larger than 2.8 for the bandgap to appear between bands 8 and 9 [4, 6]. The high-order diffraction is also more sensitive to unavoidable structural disorder than the first-order diffraction. Indeed, due to random displacements of the building blocks of the periodic structure, the intensity of the diffraction is reduced by $D \sim e^{u^2/\lambda^2}$, where u is the average displacement from the ideal lattice plane and λ is the Bragg wavelength. D^{-1} is known as the *Debye-Waller factor* [11].

For the diamond-lattice symmetry, the requirement on the dielectric contrast is less strong: the bandgap opens between bands 2 and 3 for refractive-index contrasts larger than 1.9 [5]. In contrast to the case with the *fcc* symmetry, this bandgap corresponds to the first-order diffraction, which is less sensitive to the structural disorder. Moreover, the softer requirement on the dielectric contrast gives a greater choice of materials to

make photonic crystals with wide bandgaps. Therefore structures with the diamond and the diamond-like symmetries are very desired. However, fabrication of such structures with the submicron periodicity and a considerable number of lattice periods is still a challenge. The methods of self-assembly of colloidal particles mainly result in close-packed *fcc* structures. Attempts to use patterned surfaces to grow colloidal crystals with other symmetries than the *fcc* have led to structures with the *sc* symmetry, however, with only a few periods in thickness [12]. The lithographic layer-by-layer methods, on the other hand, result in the desired structures as can be seen in Figure 3.1b. Due to many technological steps, required for fabrication of a single crystal layer, these structures are also limited to only a few lattice periods [13–16].

A very promising method to manufacture the bandgap structures is the photoelectrochemical etching and subsequent focused-ion-beam drilling [17–19]. In the photoelectrochemical etching process, a pattern of pores is created in silicon. Then the structure is cleaved, and a new pattern of pores orthogonal to the first one is drilled with a focused ion beam. The smallest lattice parameter is determined by the minimum feature size of the etch and drill processes and is about 100 nm. This method yields diamond-like "woodpile" crystals with thicknesses of about 20 periods and even larger lateral sizes.

The 3D holographic lithography [20, 21] and the direct laser writing by multi-photon polymerization [22, 23] are two techniques, which can potentially result in photonic-bandgap materials over large volumes. In the 3D holographic lithography, interference of four non-coplanar laser beams in a polymer photoresist generates an intensity distribution in a form of a 3D lattice, in which the reciprocal-lattice vectors are equal to the differences between the wavevectors of the beams. The use of an ultraviolet laser results in a minimum feature size down to 100 nm. In the direct laser writing, a desired 3D pattern is drawn in the photoresist by a focused laser beam. With two-photon polymerization, one can achieve lateral voxel sizes down to 120 nm, and this determines the size of the smallest features. Both these methods result in high-quality periodic structures from the polymer photoresist with thicknesses of 10-80 lattice periods and much greater lateral dimensions. The main deficiency of these techniques is that, in order to obtain high dielectric-contrast replicas from such 3D polymer templates, a complex process of double inversion must be performed [24]. An alternative way to avoid the necessary double inversion of the polymer templates is direct laser writing in chalcogenide glasses that have refractive indices above 2.45 [25]. The direct laser writing method has another advantage: functional defects in the polymer lattice can be introduced in a controlled way.

3.2 Optical characterization of photonic crystals

3.2.1 Observation of stopgaps

Theory for photonic crystals often describes light interaction with perfect infinitely large crystals [1, 6, 26–28]. In practice, however, every structure is finite and has unavoidable disorder. The existence of a photonic bandgap predicted by the theory for ideal periodic structures is questionable for real photonic crystals [29, 30]. Therefore, experimental investigations of fabricated photonic crystals are necessary to reveal if real crystals indeed possess signatures of a bandgap and to understand how they interact with light. Available tests of optical properties of photonic crystals include measurements of angle-resolved spectra of reflected, transmitted and emitted from internal light sources; for examples of such experiments see [31–45]. In a reflection experiment, the crystal is illuminated by external plane waves of a wide spectrum; light at frequencies inside a stopgap is Bragg diffracted and rejected from the crystal. Comparing the spectrum of rejected frequencies to the reflectance from a known reference, *e.g.*, a flat metallic mirror, reveals a stopband - an experimental measure of a stopgap. As an example in Figure 3.2, a reflectivity spectrum measured from a polystyrene opal (a) is compared to a calculated photonic band structure for an opal with a dielectric contrast of 2.53 (b). The reflectivity measured at normal incidence to the (111) crystal-lattice plane reveals two peaks at frequencies where the stopgaps are predicted by the theory. The peak at $a/\lambda = 0.6$ is a manifestation of a stopband due to the first-order Bragg diffraction on the set of (111) lattice planes. The peak at $a/\lambda = 1.1$ is associated with the second-order diffraction on the same lattice-plane set. However, comparison of the reflectivity spectrum with the calculated bands becomes complicated at higher frequencies, because of the bands folded back into the first Brillouin zone [45]. This frequency range already reveals a limitation of reflection experiments, since an increased reflectivity may be also due to flat dispersion bands and not only to absence of bands (as in a stopgap). The reduced reflectivity of the stopbands to less than 100 % is attributed to imperfections of the crystal lattice. This effect of structural disorder will be discussed in the following section.

In angle-resolved experiments, stopbands associated with diffraction on other lattice planes can be studied, *i.e.*, with other k-vectors in the Brillouin zone. Repulsion between stopbands due to simultaneous Bragg diffraction, a prerequisite of a photonic bandgap, was observed in strongly-interacting photonic crystals in angle-resolved reflection [37,

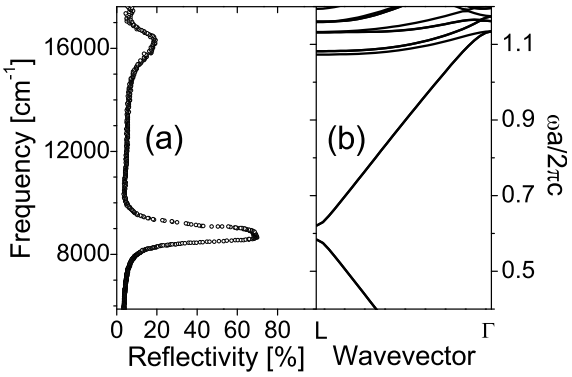

FIGURE 3.2: (a) Measured normal-incidence reflectivity spectrum from a polystyrene opal (r_{sphere} = 241 nm) consisting of hundreds of lattice periods in all directions. (b) Photonic band structure for an fcc crystal built from dielectric spheres with ϵ = 2.53. The bands are plotted versus wavevector on the ΓL line, see the inset in Fig. 2.5.

43] as well as emission experiments [39]. A possible evidence of a photonic bandgap would be to find a range of frequencies where stopbands overlap for all directions. An invariant stopband was observed along high-symmetry directions of the Brillouin zone for the silicon inverse opals [42]. In another experiment, an overlap of stopbands over a wide solid angle was demonstrated in a "woodpile" photonic crystal [44]. However, the angle-resolved reflection (and emission) spectra require a careful analysis: crystals without a photonic bandgap can also reveal omnidirectional stopbands (see, e.g., [38]). The difficulty is that the apparent reflection peaks (troughs in emission and transmission spectra) can be caused by "dark" modes - modes of the crystal, to which coupling of external waves is impeded [46, 47]. Therefore, reflection and transmission experiments do not provide conclusive proofs of the existence of a photonic bandgap.

3.2.2 Role of structural disorder

The measured reflectivity in stopbands is often less than 100 %. In the reflectivity spectrum of the polystyrene opal in Fig. 3.2a, we see features that are not explained by the theory: the experimental peaks are rounded and have maxima lower than 100 %. Ideally, one would expect rectangular peaks with 100 % reflectivity. The rounding, asymme-

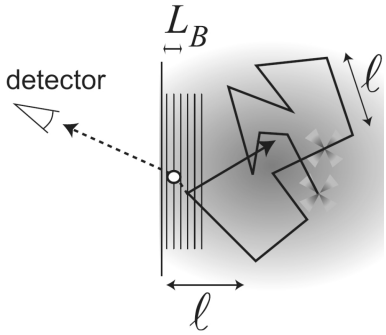

FIGURE 3.3: Schematic representation of emission propagating through a bulk photonic crystal. Directional emission pattern from a light source initially determined by locally available Bloch modes is smeared out by random scattering over a specific length ℓ. At distances from the surface smaller than ℓ, photons escape ballistically from the crystal. The emission is diffracted by the crystal planes and attenuated in the direction of the stopgap if the last scattering event occurs at distances larger than the length L_B necessary for Bragg diffraction to build up.

try and lowered intensity of the peaks are explained by extinction,[(1)] which is due to various structural imperfections: regions with non-crystalline features, grain boundaries, dislocations and other defects peculiar to all types of crystals [48]. It is important to realize that the building blocks of metastructures such as photonic crystals are never identical to each other, in contrast to atoms in atomic crystals. Therefore, imperfections like the size variation, roughness and displacement of the building blocks are always present in *all* photonic crystals [49]. This omnipresent disorder induces random scattering of light and leads to diffuse (Lambertian) reflection of external light, thereby affecting the interference-induced properties of photonic crystals. This explains the decreased attenuation in the stopbands in Fig. 3.2a and why the attenuation at higher frequencies a/λ is noticeably lower than that at the frequencies of the first-order stopband.

In a bulk photonic crystal, due to the defect-induced multiple scattering, the direction of propagation of a coherent light beam coupled to an allowed mode is randomized over a length scale called the *transport mean free path*. This transport mean free path ℓ limits the range of the crystal sizes for photonic applications where the coherency is of importance. A typical value of $\ell = 15\ \mu$m was obtained for polystyrene opals and TiO_2 inverse opals

[(1)] Absorption could also explain these experimental features, but it can be safely neglected in the case with polystyrene and with many other dielectrics.

[50]. This length is equivalent to a distance of about 40 unit cells or 70 lattice planes, which is large enough so that Bragg diffraction can build up. Although propagation of light in the direction of a stopgap is attenuated, there are other directions that are allowed by the crystal. Due to the multiple random scattering, the light propagates in a sort of zigzag way in the direction of the stopgap as sketched in Figure 3.3. If a scattering event occurs close to the crystal surface, the light can be detected unattenuated even in the direction of the stopgap. Consequently, in emission spectra from sources inside large photonic crystals as well as in transmission spectra through such crystals, pronounced stopbands can still be observed, however, their attenuation is considerably decreased by the random scattering. A stopband with nearly 100 % attenuation in the emission spectrum would unambiguously indicate a presence of a photonic bandgap [51]. Indeed, the bandgap attenuates propagation in all directions, thus light emitted in defects is trapped inside the crystal, and the frequencies of the bandgap do not appear in the emission spectrum. A detailed study of emission spectra from light sources embedded in bulk photonic crystals is presented in Chapter 4. Comparing the measured data to a theoretical model, which comprises the photonic band structure and effects of disorder, we explain the attenuation in stopbands as well as the distribution of emitted light exiting a bulk photonic crystal.

3.2.3 Time-resolved emission

Besides controlling propagation of light, photonic crystals can strongly influence the radiation dynamics of embedded emitters, as discussed in Chapter 2. The evolution of the emitter's excited state can be observed in a time-resolved experiment, where the intensity of emitted light is measured after a short excitation pulse. From the slope of the intensity decrease one can extract the radiative lifetime - the inverse of the emission decay rate. The latter is directly related to the LDOS in a photonic crystal and, thus, constitutes a first experimental constraint on this important theoretical concept. Measurements the spontaneous decay rate as a function of the photonic-crystal size can give an unambiguous proof of a bandgap. The bandgap is the frequency range where the LDOS vanishes completely, and thus, it can only exist in infinitely large photonic crystals. If the symmetry of a finite-size crystal allows a bandgap in the infinite-size limit, the decay rate at frequencies inside the gap will decrease exponentially to zero with the increasing crystal size (L): $\lim_{L\to\infty}\gamma = 0$. Otherwise, the limiting value of the decay rate will be finite, for frequencies outside the gap, or if it is not allowed by the structure [52, 53].

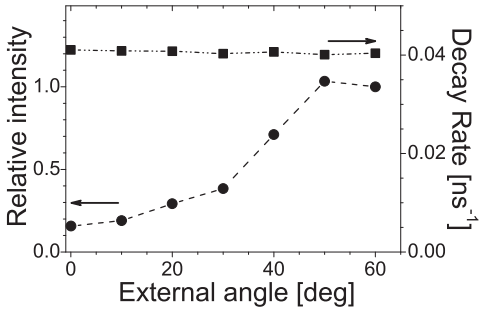

FIGURE 3.4: Measured decay rate (squares) and relative emission intensity (circles) from quantum dots at $\lambda = 610\ nm$ versus the angle from the normal to the sample surface. The measurements were performed on a TiO_2 inverse opal with the lattice parameter $a = 420\ nm$. The curves connecting the data are guides to the eye. The relative intensity is inhibited by a stopband in a wide angular range from $0°$ to $35°$, whereas the decay rate is the same in all directions, as expected. The angle-resolved experiments are discussed in detail in Chapter 4, and the emission decay rates, in Chapter 5.

Analysis of the time-resolved emission is often complicated: the measured decay curves yield the *total* decay rate, which is the sum of the radiative rate γ_{rad} and the decay rate via all non-radiative channels γ_{nrad}. These non-radiative channels are determined by the chemical environment of the emitters. Therefore, the correct interpretation of the time-resolved effects requires a comparison of the data from a photonic crystal to a chemically identical reference. A strong lifetime effect in weak photonic crystals reported in [54] is likely caused by chemical interactions between dye molecules and interfaces in photonic crystals [55]. Because emitters in photonic crystals are often distributed in different environments, both optically and chemically, measured emission decay curves are multi-exponential, which requires advanced modeling to infer the decay-rate distributions. Special attention should be also paid to emission from the host material: the measured decay curves can be distorted by fluorescence of the backbone of the crystal under the short-wavelength excitation. Furthermore, unphysically direction-dependent lifetimes in Ref. [56] are most likely caused by influence of the backbone fluorescence on the measured decay curves. In several other reports [33–35, 40], stopbands in emission spectra were wrongly associated with strong inhibition of spontaneous emission. However, in contrast to the directional stopbands, the radiative decay rate is an angle-integrated property as predicted by theory (Eq. 2.32): the LDOS counts modes with *all* k-vectors.

Figure 3.4 shows an example of angle-resolved emission decay rate and continuous-wave intensity in a photonic crystal: the intensity is strongly direction-dependent as a consequence of Bragg diffraction, but the decay rate is the same for different directions. Therefore, no change of the emission rates can be concluded from measuring a stopband in one particular direction. By measuring the total emitted power from sources with a low quantum efficiency and comparing that power to a homogeneous medium, it is possible to infer modifications of the emission decay rates [57]. However, in order to truly control spontaneous emission, one needs highly-efficient light sources and strongly photonic crystals. In Chapter 5 we describe a lifetime experiment, in which considerable modifications of decay rates of spontaneous emission were observed in the TiO_2 inverse opals and compared to the calculated LDOS.

3.3 Photonic crystals studied in this work

In the experiments described in this thesis, we have studied two types of 3D photonic crystals: polystyrene opals and titania inverse opals. The polystyrene opals are *fcc* crystals of close-packed polystyrene spheres prepared from a colloidal suspension by self-assembly. The titania inverse opals are *fcc* structures of close-packed air spheres in a solid matrix of TiO_2. Polystyrene opals as well as titania inverse opals are transparent for visible light, of a high quality and well characterized [7, 58, 59]. The inverse opals also have a high refractive-index contrast of about 2.7, which makes them the most strongly photonic 3D crystals for optical frequencies. Figure 3.5 shows scanning electron microscopy (SEM) images of surfaces of a polystyrene opal (a) and of an inverse opal from titania (b). Details of the preparation and characterization of the opals and inverse opals can be found in Reference [7]. All the crystals have typical dimensions of 2x2x0.2 mm^3 and contain high-quality domains with diameters larger than 50 μm. These domains have flat faces parallel to the (111) crystal plane, which is evident in Fig. 3.5.

We have calculated the photonic band structures corresponding to the polystyrene opals and titania inverse opals and plotted them in Figure 3.6. The band structure of the opals reveals a 6 % stopgap along the the ΓL direction (Fig. 3.6a), that corresponds to

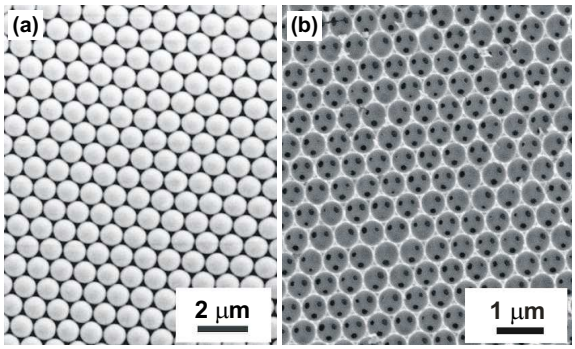

FIGURE 3.5: SEM images (top view) of two photonic crystals with the fcc crystal symmetry: a polystyrene opal (a) and an inverse opal (b). In the inverse opal, the white material is TiO_2 (titania), while the air-spheres appear grey. Neighboring air-spheres are connected by windows, which are seen as the black holes.

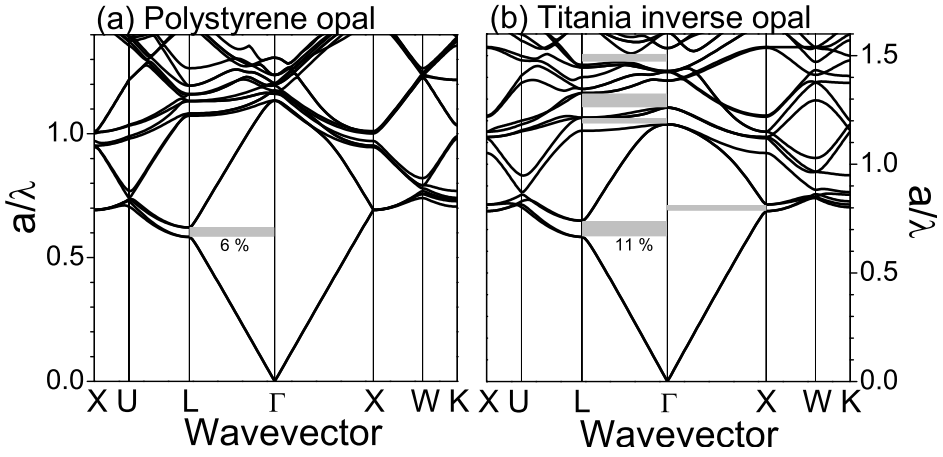

FIGURE 3.6: The photonic band structures plotted along lines connecting points Γ, L, X, U, W, K (see the inset in Fig. 2.5) calculated for two fcc crystals: (a) opal consisting of close-packed spheres with ϵ = 2.53 and (b) titania inverse opal built from air spheres surrounded by dielectric shells (ϵ = 6.5). Parameters of the shell structure for the inverse opals are described in detail in Chapter 6. Grey rectangles indicate stopgaps in the ΓL direction and one stopgap in the ΓX direction for the inverse opal. The calculations were done using 725 plane waves.

Bragg diffraction on the (111) crystal-plane set. Such first-order stopgaps, also called *L-gaps*, are typically seen as reflectivity peaks in normal-incidence measurements, as demonstrated in Fig. 3.2a. Because the inverse opals have a higher photonic strength, as discussed in Section 2.2, the band structure for the inverse opals has brighter features. In Fig. 3.6b we see a broader L-gap as well as other, higher-order stopgaps in the ΓL direction and a narrow stopgap in the ΓX direction. The L-gap in the inverse opals is wider (11 %) than in the opals and occurs at slightly higher frequencies due to a lower volume-averaged refractive index in the inverse opals ($n_{av} = 1.27$) than that in polystyrene opals ($n_{av} = 1.45$).

Prior to investigating emission in our photonic crystals, the stopgaps predicted by the band structures were studied experimentally. First, we inspected the opals and the inverse opals with an optical microscope: samples with large high-quality domains have flat and opalescent (in case when the stopbands are in the visible range) surface regions. Then, using an external broadband light source, reflectivity spectra were recorded from those regions in order to determine the center frequencies and the widths of the stopbands [36, 43]. The reflectivity spectra were recorded using a Fourier-transform spectrometer

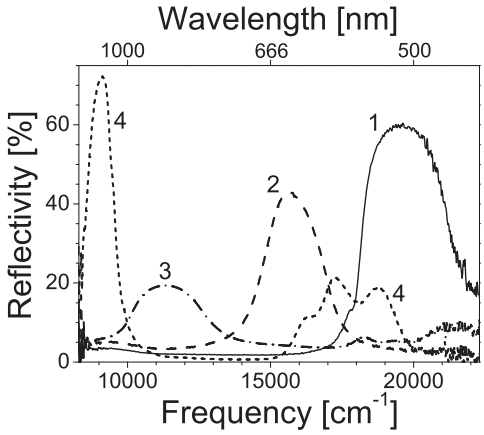

FIGURE 3.7: Normal-incidence reflectivity spectra from titania inverse opals with four different lattice parameters: (1) $a = 370$ nm, (2) $a = 425$ nm, (3) $a = 600$ nm and (4) $a = 755$ nm. The reflectivity peaks represent the first-order stopbands, the frequency ranges of which are determined by the lattice parameter. The relative width of the stopbands $\Delta\omega/\omega$ is about 0.16. Sample 4 clearly shows second-order stopbands within the studied frequency range: between 15500 and 19500 cm^{-1}.

(Biorad FTS-6000). Only samples with reflectivity larger than 15 % were selected for the emission experiments. A typical reflectivity spectrum from the polystyrene opals has been shown in Fig. 3.2a. The reflectivity measurements at normal incidence on the polystyrene opals reveal the first-order stopband with reflectivity up to 80 % and the relative width of about 0.075. In Figure 3.7 we present reflectivity spectra from four titania inverse opals with different crystal lattice parameters. In reflection measurements on the titania inverse opals, the stopbands with reflectivity up to 75 % were observed. The center frequency of the first-order stopband increases with decreasing lattice parameter, and the relative width is unchanged: $\Delta\omega/\omega \approx 0.16$. In earlier studies, it was shown that propagation of light at frequencies within the lowest stopband is forbidden for 55 % of the 4π solid angle [36]. The three stopbands of the higher order (Fig. 3.7, curve 4) are caused by the second-order stopgaps, which have negligible angular dispersion and, hence, are the precursor of a photonic band gap [38].

3.4 Light sources

The ideal light source for emission-lifetime experiments in photonic crystals should meet the following essential requirements: (a) a narrow emission spectrum in order to maximally feel changes of the LDOS, (b) a high magnitude of the transition dipole moment that determines the emitter-field interaction, as discussed in Chapter 2 (Eq. 2.4); (c) a low rate of non-radiative transitions γ_{nrad}, which means a nearly 100 % quantum efficiency; and (d) its optical properties such as energy levels and the transition dipole moment as well as the non-radiative rate γ_{nrad} are insensitive to the chemical environment. We now will briefly review several classes of light sources.

Lanthanides, or rare-earth atoms, show luminescence due to transitions from $4f$ internal atomic levels, which are shielded by the outer electrons. Therefore these transitions are, in principle, not influenced by the environment. The emission spectra of all lanthanides have characteristic sets of sharp peaks [60]. The drawback of these emitters is that the internal-shell transitions are parity forbidden, which results in low values of the transition dipole moment and consequently, low emission rates. The emission lifetimes of such ions are therefore very long: from microseconds to milliseconds. Fluorescent molecules, for comparison, have nanosecond emission lifetimes. For the same reason, the

absorbance of these ions is also poor, and the quantum efficiency of most of lanthanides is rather low.

In contrast to a few kinds of atomic emitters, there is a great variety of organic fluorescent molecules often called *organic dyes* [61, 62]. These organic light sources cover a wide range of wavelengths: from ultraviolet to near infrared. Organic fluorescent probes are available with quantum efficiencies close to 100 %, with short (nanoseconds) as well as long (up to milliseconds) lifetimes. Optical properties of these emitters, however, are strongly influenced by chemical interactions [61, 62]: this property is often used in characterization of complex chemical and biological systems. However, one often encounters difficulties using organic dyes as fluorescent probes in photonic crystals made from strong quenchers such as, *e.g.*, TiO_2 [63]. Furthermore, under influence of excitation light, irreversible modifications of dye molecules often occur, making the molecules nonfluorescent. This *photobleaching* process is the main drawback of the organic dyes, which limits their usage time. Due to complex structure of the molecular vibrational levels, the homogeneous emission linewidth of dye molecules is rather broad: mostly broader than stopbands of photonic crystals. This makes the dyes ideal internal probes of photonic crystals in angle-resolved experiments: the stopbands can be readily inferred from modified shapes of the broad emission spectra. On the other hand, the radiative lifetime of the dyes is determined by an average LDOS over the homogeneous linewidth, and the changes of the lifetime are expected to be small [64, 65].

Semiconductor nanocrystals, also known as *quantum dots*, are a new and very promising type of light sources [66–68]. In contrast to bulk semiconductors, the exciton energy-level structure of the nanocrystals is strongly size- and shape-dependent due to the small sizes of several nanometers. In a bulk semiconductor, when an electron is excited across the bandgap into the conduction band, it leaves a hole in the valence band. By the attractive Coulomb interaction, the excited electron in the conduction band and the hole in the valance band may approach each other and form an electron-hole pair called *exciton*. In case of a bulk CdSe semiconductor, such an electron-hole pair forms a weakly bound exciton or the Wannier exciton [69, 70]. The average electron-hole separation distance is known as the *Bohr radius*, which is about 6 nm in bulk CdSe. If the size of the semiconductor particle is comparable to the Bohr radius, the exciton is confined inside the resulting quantum dot. With a further decrease of the quantum-dot size, the energy gap becomes larger and the valence and conduction bands gradually split to discrete levels, as schematically depicted in Figure 3.8a. This discrete-level energy structure in quantum

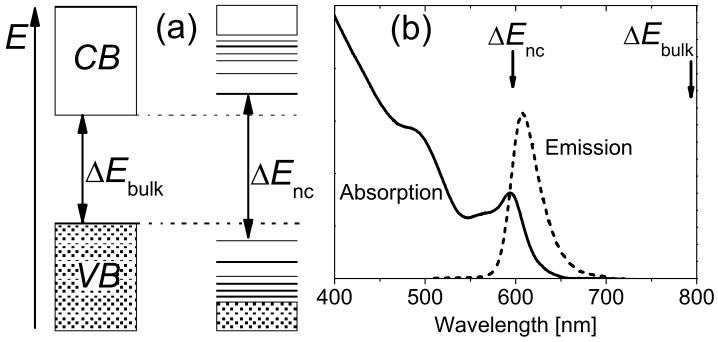

FIGURE 3.8: (a) Schematic band structure of a bulk semiconductor (*left*) and of a nanocrystal (*right*). In the bulk crystal, the energy gap ΔE_{bulk} separates the populated valence band (VB) from the empty conduction band. In the nanocrystal, the energy-level scheme is discrete; the highest occupied and lowest empty levels are separated by the size-dependent gap ΔE_{nc}. (b) Measured absorption (solid curve) and emission (dashed curve) spectra of CdSe-ZnSe core-shell quantum dots with the average diameter of 4.5 nm. The emission is measured at a non-resonant excitation with λ = 450 nm. The inhomogeneous broadening of the absorption and emission peaks as well as the Stokes shift between the peaks are due to a size dispersion of the nanocrystals [70]. Image courtesy of F. van Driel.

dots results in narrow, atom-like emission spectra. For example, at cryogenic temperatures, AlAs/InAs/GaAs quantum dots grown by molecular beam epitaxy (further, MBE quantum dots) and CdSe colloidal quantum dots have relative linewidths $\Delta\omega/\omega$ that are less than $1.5 \cdot 10^{-4}$ [71, 72]. At higher temperatures, the MBE quantum dots become dark due to low exciton binding energies in these dots. The emission linewidth of colloidal quantum dots increases with temperature; and at room temperatures, it is ~ 0.025 [73, 74], which is still small enough to observe the LDOS variations in photonic crystals. On the other hand, because the level spectrum at high energies is still continuous as in bulk semiconductors, the absorbtion spectra of the quantum dots are very broad. This gives freedom to choose the excitation frequencies in the emission experiments on a particular photonic crystal: the frequency should be low to minimize the backbone fluorescence but, on the other hand, it should be outside the stopbands of the photonic crystal. In Figure 3.8b we see wide absorption and narrow lowest-exciton emission spectra from the CdSe quantum dots with the diameter of about 4.5 nm. The observed peaks in the absorption and emis-

sion spectra are inhomogeneously broadened because of the size variation between the quantum dots in the ensemble.

By appropriate selection of materials and sizes of quantum dots, one can tune emission over a wide range of wavelengths. The exciton emission in ZnO quantum dots can be tuned around 380 nm [75–77]. Dots from CdSe and CdTe cover most of the visible range between 460 and 760 nm [78–80]. In the infrared, emission from MBE dots can be tuned within 0.85 - 1.1 μm range [68, 71, 81–83] and from PbSe/PbS dots within 1.1 - 2.2 μm range [84–86]. The radiative lifetimes of different nanocrystals range from picoseconds to microseconds. Quantum dots can be also capped with semiconductors with larger bandgaps and/or with layers of organic materials [78, 87–90]. These capping layers shield the nanocrystals and prevent interactions of excitons with the surface thereby enhancing the quantum efficiency and chemical stability of the quantum dots. Various capping techniques of the MBE quantum dots result in a red shift of emission wavelengths toward the desired for telecommunications λ = 1.55 μm and, furthermore, to the conservation of high radiative recombination efficiency up to room temperature [91–93]. Hence, owing to the narrow and tunable emission spectra and the photostability, quantum dots are widely used as fluorescent sources in light-emitting thin-films devices [94, 95], lasers [68, 96, 97] and biological labels [87, 88]. These highly-efficient emitters are also ideal probes for the lifetime experiments in photonic media: modifications of the radiative lifetimes [98, 99] and even signatures of strong coupling between a quantum dot and a cavity [100–102] were observed in experiments on the MBE dots in microcavities.

In the emission experiments described in this thesis, we used CdSe quantum dots capped with ZnSe prepared by chemical synthesis [78, 103]. The quantum efficiency of an ensemble of these nanocrystals dispersed in chloroform is larger than 50 %: we measured it by comparing the emission and absorbtion yields to the R6G dye, which is a calibrated standard (for details see Ref. [104]). The quantum dots have a size dispersion of 5 % around the average diameter of 4.5 nm, which determines the center wavelength of the emission spectrum at $\lambda \approx 610$ nm (see Fig. 3.8b). Extensive details of preparation and characterization of these high-quality quantum dots can be found in Reference [105].

3.5 Conclusions

We have discussed the crystal symmetries allowing for the photonic bandgap for reasonable dielectric contrasts. Fabrication of photonic crystals possessing the bandgap is a rather complicated task. However, the recent advances in the nano-structuring technologies can make the photonic crystals with the bandgaps at optical frequencies practically realizable. Optical characterization of fabricated photonic crystals is necessary to understand how the latter influence light propagation and to prove existence of the photonic bandgap. Knowledge of the photonic dispersion relation as well as effects of the structural disorder are important for correct interpretation of data obtained in the angle-resolved reflection, transmission and emission experiments. We have introduced the photonic crystals that we use in our emission experiments: polystyrene opals and titania inverse opals. Their optical characteristics are also presented: theoretical (photonic band structures) and experimental (reflectivity spectra). We have discussed different sorts of fluorescent probes that can be used in the emission experiments on photonic crystals. One should be aware of possible chemical effects of materials constituting the photonic crystals on the radiating properties of the embedded emitters. We concluded that organic dyes with their broad emission spectra are very suitable for the angle-resolved experiments, whereas semiconductor quantum dots with very narrow linewidths are ideal probes for the time-resolved experiments on photonic media.

References

[1] K. M. Ho, C. T. Chan and C. M. Soukoulis, *Existence of a Photonic Gap in Periodic Dielectric Structures*, Phys. Rev. Lett. **65**, 3152 (1990).

[2] C. T. Chan, K. M. Ho and C. M. Soukoulis, *Photonic Band-Gaps in Experimentally Realizable Periodic Dielectric Structures*, Europhys. Lett. **16**, 563 (1991).

[3] E. Yablonovitch, T. J. Gmitter and K. M. Leung, *Photonic Band Structure: The Face-Centered-Cubic Case Employing Nonspherical Atoms*, Phys. Rev. Lett. **67**, 2295 (1991).

[4] H. S. Sözüer and J. W. Haus, *Photonic Bands - Simple-Cubic Lattice*, J. Opt. Soc. B **10**, 296 (1993).

[5] K. M. Ho, C. T. Chan, C. M. Soukoulis, R. Biswas and M. Sigalas, *Photonic Band-Gaps in 3-Dimensions: New Layer-by-Layer Periodic Structures*, Solid State Commun. **89**, 413 (1994).

[6] K. Busch and S. John, *Photonic Band Gap Formation in Certain Self-Organizing Systems*, Phys. Rev. E **58**, 3896 (1998).

[7] J.E.G.J. Wijnhoven and W. L. Vos, *Preparation of Photonic Crystals Made of Air Spheres in Titania*, Science **281**, 802804, (1998); J.E.G.J. Wijnhoven, L. Bechger and W. L. Vos, *Fab-*

rication and Characterization of Large Macroporous Photonic Crystals in Titania, Chem. Mater. **13**, 4486 (2001).

[8] A. A. Zakhidov, R. H. Baughman, Z. Iqbal, C. Cui, I. Khayrullin, S. O. Dantas, J. Marti and V. G. Ralchenko, *Carbon Structures with Three-Dimensional Periodicity at Optical Wavelengths*, Science **282**, 897 (1998).

[9] A. Blanco, E. Chomski, S. Grabtchak, M. Ibisate, S. John, S. W. Leonard, C. López, F. Meseguer, H. Míguez, J. P. Mondia, G. A. Ozin, O. Toader and H. M. van Driel, *Large-Scale Synthesis of a Silicon Photonic Crystal with a Complete Three-Dimensional Bandgap Near 1.5 Micrometres*, Nature **405**, 437 (2000).

[10] Y. A. Vlasov, X. Z. Bo, J. C. Sturm and D. J. Norris, *On-Chip Natural Assembly of Silicon Photonic Bandgap Crystals*, Nature **414**, 289 (2001).

[11] A. Guinier, *X-Ray Diffraction in Crystals, Imperfect Crystals, and Amorphous Bodies*, Dover, New-York (1994).

[12] J. P. Hoogenboom, C. Rétif, E. de Bres, M. van den Boer, A. K. van Langen-Suurling, J. Romijn and A. van Blaaderen, *Template-Induced Growth of Close-Packed and Non-Close-Packed Colloidal Crystals during Solvent Evaporation*, Nanolett. **4**, 205 (2004).

[13] S. Y. Lin, J. G. Fleming, D. L. Hetherington, B. K. Smith, R. Biswas, K. M. Ho, M. M. Sigalas, W. Zubrzycki, S. R. Kurtz and J. Bur, *A Three-Dimensional Photonic Crystal Operating at Infrared Wavelengths*, Nature **394**, 251 (1998).

[14] J. G. Fleming and S.-Y. Lin, *Three-Dimensional Photonic Crystal with a Stop Band from 1.35 to 1.95 μm*, Opt. Lett. **24**, 49 (1998).

[15] S. Noda, K. Tomoda, N. Yamamoto and A. Chutinan, *Full Three-Dimensional Photonic Bandgap Crystals at Near-Infrared Wavelengths*, Science **289**, 604 (2000).

[16] K. Aoki, H. T. Miyazaki, H. Hirayama, K. Inoshita, T. Baba, K. Sakoda, N. Shinya and Y. Aoyagi, *Microassembly of Semiconductor Three-Dimensional Photonic Crystals*, Nat. Mater. **2**, 117 (2003).

[17] R. Hillebrand, S. Senz, W. Hergert and U. Gösele, *Macroporous-Silicon-Based Three-Dimensional Photonic Crystal with a Large Complete Band Gap*, J. Appl. Phys. **94**, 2758 (2003).

[18] J. Schilling, J. White, A. Scherer, G. Stupian, R. Hillebrand and U. Gösele, *Three-Dimensional Macroporous Silicon Photonic Crystal with Large Photonic Band Gap*, Appl. Phys. Lett. **86**, 011101 (2005).

[19] L. Woldering, W. Tjerkstra and W. L. Vos, unpublished results.

[20] M. Campbell, D. N. Sharp, M. T. Harrison, R. G. Denning and A. J. Turberfield, *Fabrication of Photonic Crystals for the Visible Spectrum by Holographic Lithography*, Nature **404**, 53 (2000).

[21] Y. V. Miklyaev, D. C. Meisel, A. Blanco, G. von Freymann, K. Busch,W. Koch, C. Enkrich, M. Deubel and M. Wegener, *Three-Dimensional Face-Centered-Cubic Photonic Crystal Templates by Laser Holography: Fabrication, Optical Characterization, and Band-Structure Calculations*, Appl. Phys. Lett. **82**, 1284 (2003).

[22] S. Kawata, H.-B. Sun, T. Tanaka and K. Takada, *Finer Features for Functional Microdevices*, Nature **412**, 697 (2001).

[23] M. Deubel, G. von Freymann, M. Wegener, S. Pereira, K. Busch and C. M. Soukoulis, *Direct Laser Writing of Three-Dimensional Photonic-Crystal Templates for Telecommunications*, Nature Mater. **3**, 444 (2004).

[24] N. Tétreault, G. von Freymann, M. Deubel, M. Hermatschweiler, F. Pérez-Willard, S. John, M. Wegener and G. A. Ozin, *New Route to Three-Dimensional Photonic Bandgap Materi-*

als: Silicon Double Inversion of Polymer Templates, Adv. Mater. **18**, 457 (2006).

[25] S. Wong, M. Deubel, F. Pérez-Willard, S. John, G. A. Ozin, M. Wegener and G. von Freymann, *Direct Laser Writing of Three-Dimensional Photonic Crystals with a Complete Photonic Bandgap in Chalcogenide Glasses*, Adv. Mater. **18**, 265 (2006).

[26] H. S. Sözüer, J. W. Haus and R. Inguva, *Photonic Bands: Convergence Problems with the Plane-Wave Method*, Phys. Rev. B **45**, 13962 (1992).

[27] J. D. Joannopoulos, R. D. Meade and J.N. Winn, *Photonic Crystals: Molding the Flow of Light*, Princenton University Press, (1995).

[28] C. M. Soukoulis, editor, *Photonic Crystals and Light Localization in the 21st Century*, Kluwer, Dordrecht, (2001).

[29] R. Biswas, M. M. Sigalas, G. Subramania, C. M. Soukoulis and K.-M. Ho, *Photonic Band Gaps of Porous Solids*, Phys. Rev. B **61**, 4549 (2000).

[30] Z.-Y. Li and Z.-Q. Zhang, *Fragility of Photonic Band Gaps in Inverse-Opal Photonic Crystals*, Phys. Rev. B **62**, 1516 (2000).

[31] I. I. Tarhan and G. H. Watson, *Photonic Band Structure of FCC Colloidal Crystals*, Phys. Rev. Lett **76**, 315 (1996).

[32] W. L. Vos, R. Sprik, A. van Blaaderen, A. Imhof, A. Lagendijk and G. H. Wegdam, *Strong Effects of Photonic Band Structures on The Diffraction of Colloidal Crystals*, Phys. Rev. B. **53**, 16231 (1996).

[33] S. V. Gaponenko, A. M. Kapitonov, V. N. Bogomolov, A. V. Prokofiev, A. Eychmüller and A. L. Rogach, *Electrons and Photons in Mesoscopic Structures: Quantum Dots in a Photonic Crystal*, JETP Lett. **68**, 142 (1998).

[34] K. Yoshino, S. B. Lee, S. Tatsuhara, Y. Kawagishi, M. Ozaki and A. A. Zakhidov, *Observation of Inhibited Spontaneous Emission and Stimulated Emission of Rhodamine 6G in Polymer Replica of Synthetic Opal*, Appl. Phys. Lett. **73**, 3506 (1998).

[35] A. Blanco, C. López, R. Mayoral, H. Míguez, F. Meseguer, A. Mifsud and J. Herrero, *CdS Photoluminescence Inhibition by a Photonic Structure*, Appl. Phys. Lett. **73**, 1781 (1998).

[36] M. S. Thijssen, R. Sprik, J.E.G.J. Wijnhoven, M. Megens, T. Narayanan, A. Lagendijk and W. L. Vos, *Inhibited Light Propagation and Broad Band Reflection in Photonic Air-Sphere Crystals*, Phys. Rev. Lett. **83**, 2730 (1999).

[37] H. M. van Driel and W. L. Vos, *Multiple Bragg Wave Coupling in Photonic Band Gap Crystals*, Phys. Rev. B **62**, 9872 (2000).

[38] W. L. Vos and H. M. van Driel, *Higher Order Bragg Diffraction by Strongly Photonic FCC Crystals: Onset of a Photonic Bandgap*, Phys. Lett. A **272**, 101 (2000).

[39] H. P. Schriemer, H. M. van Driel, A. F. Koenderink and W. L. Vos, *Modified Spontaneous Emission Spectra of Laser Dye in Inverse Opal Photonic Crystals*, Phys. Rev. A **63**, 011801(R) (2001).

[40] S. G. Romanov, T. Maka, C. M. Sotomayor-Torres, M. Müller and R. Zentel, *Suppression of Spontaneous Emission in Incomplete Opaline Photonic Crystals*, J. Appl. Phys. **91**, 9426 (2002).

[41] J. F. Galisteo-López and W. L. Vos, *Angle Resolved Reflectivity of Single-Domain Photonic Crystals: Effects of Disorder*, Phys. Rev. E **66**, 036616 (2002).

[42] E. Palacios-Lidón, A. Blanco, M. Ibisate, F. Meseguer, C. López and J. Sánchez-Dehesa, *Optical Study of the Full Photonic Band Gap in Silicon Inverse Opals*, Appl. Phys. Lett. **81**, 4925 (2002).

[43] J. F. Galisteo-López, E. Palacios-Lidón, E. Castillo-Martínez and C. López, *Optical Study of the Pseudogap in Thickness and Orientation Controlled Artificial Opals*, Phys. Rev. B **68**,

115109 (2003).

[44] S. Ogawa, M. Imada, S. Yoshimoto, M. Okato and S. Noda, *Control of Light Emission by 3D Photonic Crystals*, Science **305**, 227 (2004).

[45] J. F. Galisteo-López and C. López, *High-Energy Optical Response of Artificial Opals*, Phys. Rev. B **70**, 035108 (2004).

[46] W. M. Robertson, G. Arjavalingam, R. D. Meade, K. D. Brommer, A. M. Rappe and J. D. Joannopoulos, *Measurement of Photonic Band Structure in a Two-Dimensional Periodic Dielectric Array*, Phys. Rev. Lett. **68**, 2023 (1992).

[47] K. Sakoda, *Group-Theoretical Classification of Eigenmodes in Three-Dimensional Photonic Lattices*, Phys. Rev. B **55**, 15345 (1997).

[48] N. W. Ashcroft and N. D. Mermin, *Solid State Physics* (Holt, Rinehart and Winston, New York, 1976).

[49] A. F. Koenderink, A. Lagendijk and W. L. Vos, *Optical Extinction due to Intrinsic Structural Variations of Photonic Crystals*, Phys. Rev. B **72**, 153102 (2005) and references therein.

[50] A. F. Koenderink, M. Megens, G. van Soest, W. L. Vos and A. Lagendijk *Enhanced Backscattering from Photonic Crystals*, Phys. Lett. A. **268**, 104 (2000).

[51] M. Megens, J.E.G.J. Wijnhoven, A. Lagendijk and W. L. Vos, *Light Sources inside Photonic Crystals*, J. Opt. Soc. Am. B **16**, 1403 (1999).

[52] J. S. Kole, *New Methods for the Numerical Solution of Maxwell's Equations*, Ph.D. thesis, University of Groningen, ISSN: 1570-1530 (2003).

[53] A. Lagendijk, A. F. Koenderink and W. L. Vos, private communications.

[54] J. Martorell and N. M. Lawandy, *Observation of Inhibited Spontaneous Emission in a Periodic Dielectric Structure*, Phys. Rev. Lett. **65**, 1877 (1990).

[55] B. Y. Tong, P. K. John, Y.-T. Zhu, Y. S. Liu, S. K. Wong and W R. Ware, *Fluorescence-Lifetime Measurements in Monodispersed Suspensions of Polystyrene Particles*, J. Opt. Soc. Am. B **10**, 356 (1993).

[56] J.-Y. Zhang, X.-Y. Wang, M. Xiao and Y.-H. Ye, *Modified Spontaneous Emission of CdTe Quantum Dots inside a Photonic Crystal*, Opt. Lett. **28**, 1430 (2003).

[57] A. F. Koenderink, L. Bechger, H. P. Schriemer, A. Lagendijk and W. L. Vos, *Broadband Fivefold Reduction of Vacuum Fluctuations Probed by Dyes in Photonic Crystals*, Phys. Rev. Lett. **88**, 143903 (2002).

[58] A. F. Koenderink, M. Megens, G. van Soest, W. L. Vos and A. Lagendijk, *Enhanced Backscattering from Photonic Crystals*, Phys. Lett. A. **268**, 104 (2000).

[59] A. F. Koenderink and W. L. Vos, *Optical Properties of Real Photonic Crystals: Anomalous Diffuse Transmission*, J. Opt. Soc. Am. B **22** , 1075 (2005).

[60] B. Henderson and G. F. Imbush, *Optical Spectroscopy of Inorganic Solids*, Clarendon Press, Oxford, (1989).

[61] N. J. Turro, *Modern Molecular Photochemistry*, University Science Books, California, (1991).

[62] J. R. Lakowicz, *Principles of Fluorescence Spectroscopy* (Second Edition), Kluwer, New-York, (1999).

[63] L. Bechger, A. F. Koenderink and W. L. Vos, *Emission Spectra and Lifetimes of R6G Dye on Silica-Coated Titania Powder*, Langmuir **18**, 2444 (2002).

[64] M. Megens, J.E.G.J. Wijnhoven, A. Lagendijk and W. L. Vos *Fluorescence Lifetimes and Linewidths of Dye in Photonic Crystals*, Phys. Rev. A. **59**, 4727 (1999).

[65] N. Danz, J. Heber, A. Brauer and R. Kowarschik, *Fluorescence Lifetimes of Molecular Dye Ensembles near Interfaces*, Phys. Rev. A **66**, 63809 (2002).

[66] A. P. Alivisatos, *Perspectives on the Physical Chemistry of Semiconductor Nanocrystals*, J. Phys. Chem. **100**, 13226 (1996).

[67] U. Woggon, *Optical Properties of Semiconductor Quantum Dots*, Springer, Berlin (1997).

[68] D. Bimberg, M. Grundmann and N. Ledentsov, *Quantum Dot Heterostructures*, Wiley & Sons Ltd, Chichester, England (1999).

[69] L. E. Brus, *Electron-Electron and Electron-Hole Interactions in Small Semiconductor Crystallites: The Size Dependence of the Lowest Excited Electronic State*, J. Chem. Phys. **80**, 4403 (1984).

[70] A. L. Efros, M. Rosen, M. Kuno, M. Nirmal, D. J. Norris and M. Bawendi, *Band-Edge Exciton in Quantum Dots of Semiconductors with a Degenerate Valence Band: Dark and Bright Exciton States*, Phys. Rev. B **54**, 4843 (1996).

[71] M. Grundmann, J. Christen, N. N. Ledentsov, J. Böhrer, D. Bimberg, S. S. Ruvimov, P. Werner, U. Richter, U. Gösele, and J. Heydenreich, V. M. Ustinov, A. Yu. Egorov, A. E. Zhukov, P. S. Kop'ev and Zh. I. Alferov, *Ultranarrow Luminescence Lines from Single Quantum Dots*, Phys. Rev. Lett. **74**, 4043 (1995).

[72] S. A. Empedocles, D. J. Norris and M. G. Bawendi, *Photoluminescence Spectroscopy of Single CdSe Nanocrystallite Quantum Dots*, Phys. Rev. Lett. **77**, 3873 (1996).

[73] W.G.J.H.M. van Sark, P.L.T.M. Frederix, D. J. van den Heuvel, H. C. Gerritsen, A. A. Bol, J.N.J. van Lingen, C. D. de Mello Donegá and A. Meijerink, *Photooxcidation and Photobleaching of Single CdSe/ZnS Quantum Dots Probed by Room-Temperature Time-Resolved Spectroscopy*, J. Phys. Chem. B. **105**, 8281 (2001).

[74] G. Schlegel, J. Bohnenberger, I. Potapova and A. Mews, *Fluorescence Decay Time of Single Semiconductor Nanocrystals*, Phys. Rev. Lett. **88**, 137401 (2002).

[75] A. van Dijken, E. A. Meulenkamp, D. Vanmaekelbergh and A. Meijerink, *The Kinetics of the Radiative and Nonradiative Processes in Nanocrystalline ZnO Particles upon Photoexcitation*, J. Phys. Chem. B **104**, 1715 (2000).

[76] L. Guo, S. Yanga, C. Yang, P. Yu, J. Wang, W. Ge and G. K. L. Wong, *Highly Monodisperse Polymer-Capped ZnO Nanoparticles: Preparation and Optical Properties*, Appl. Phys. Lett. **76**, 2901 (2000).

[77] V. A. Fonoberov and A. A. Balandin, *Origin of Ultraviolet Photoluminescence in ZnO Quantum Dots: Confined Excitons Versus Surface-Bound Impurity Exciton Complexes*, Appl. Phys. Lett. **85**, 5971 (2004).

[78] B. O. Dabbousi, J. Rodriguez-Viejo, F. V. Mikulec, J. R. Heine, H. Mattoussi, R. Ober, K. F. Jensen and M. G. Bawendi, *(CdSe)ZnS Core-Shell Quantum Dots: Synthesis and Characterization of a Size Series of Highly Luminescent Nanocrystallites*, J. Phys. Chem. B **101**, 9463 (1997).

[79] D. V. Talapin, A. L. Rogach, A. Kornowski, M. Haase and H. Weller, *Highly Luminescent Monodisperse CdSe and CdSe/ZnS Nanocrystals Synthesized in a Hexadecylamine-Trioctylphosphine Oxide-Trioctylphospine Mixture*, Nano Lett. **1**, 207 (2001).

[80] O. Schöps, N. Le Thomas, U. Woggon and M. V. Artemyev, *Recombination Dynamics of CdTe/CdS Core-Shell Nanocrystals*, J. Phys. Chem. B **110**, 2074 (2006).

[81] J.-Y. Marzin, J.-M. Gérard, A. Izraël, D. Barrier and G. Bastard, *Photoluminescence of Single InAs Quantum Dots Obtained by Self-Organized Growth on GaAs*, Phys. Rev. Lett. **73**, 716 (1994).

[82] K. Brunner, G. Abstreiter, G. Böhm, G. Trankle and G. Weimann, *Sharp-Line Photoluminescence and Two-Photon Absorption of Zero-Dimensional Biexcitons in a GaAs/AlGaAs Structure*, Phys. Rev. Lett. **73**, 1138 (1994).

[83] P. M. Petroff, A. Lorke and A. Imamoglu, *Epitaxially Self-Assembled Quantum Dots*, Phys. Today **54**,46 (May 2001).

[84] A. Lipovskii, E. Kolobkova, V. Petrikov, I. Kang, A. Olkhovets, T. Krauss, M. Thomas, J. Silcox, F. Wise, Q. Shen and S. Kycia, *Synthesis and Characterization of PbSe Quantum Dots in Phosphate Glass*, Appl. Phys. Lett. **71**, 3406 (1997).

[85] J. S. Steckel, S. Coe-Sullivan, V. Bulović and M. G. Bawendi, *1.3 μm to 1.55 μm Tunable Electroluminescence from PbSe Quantum Dots Embedded within an Organic Device*, Adv. Mat. **15**, 1862 (2003).

[86] K. R. Choudhury, Y. Sahoo, T. Y. Ohulchanskyy and P. N. Prasad, *Efficient Photoconductive Devices at Infrared Wavelengths Using Quantum Dot-Polymer Nanocomposites*, Appl. Phys. Lett. **87**, 73110 (2005).

[87] M. Bruchez, Jr., M. Moronne, P. Gin, S. Weiss and A. P. Alivisatos, *Semiconductor Nanocrystals as Fluorescent Biological Labels*, Science **281**, 2013 (1998).

[88] W. C. W. Chan and S. Nie, *Quantum Dot Bioconjugates for Ultrasensitive Nonisotopic Detection*, Science **281**, 2016 (1998).

[89] D. V. Talapin, I. Mekis, S. Go1tzinger, A. Kornowski, O. Benson and H. Weller, *CdSe/CdS/ZnS and CdSe/ZnSe/ZnS Core-Shell-Shell Nanocrystals*, J. Phys. Chem. B **108**, 18826 (2004).

[90] L. Feng, X. Kong, K. Chaoa, Y. Suna, Q. Zenga and Y. Zhang, *Efficient Phase Transfer of Hydrophobic CdSe Quantum Dots: From Nonpolar Organic Solvent to Biocompatible Water Buffer*, Mat. Chem. Phys. **93**, 310 (2005).

[91] B. Lambert, A. Le. Corre, V. Drouot, H. L'Haridon and S. Loualiche, *High Photoluminescence Efficiency of InAs/InP Self-Assembled Quantum Dots Emitting at 1.5 - 1.6 μm*, Semicond. Sci. Technol. **13**, 143 (1998).

[92] V. M. Ustinov, N. A. Maleev, A. E. Zhukov, A. R. Kovsh, A. Yu. Egorov, A. V. Lunev, B. V. Volovik, I. L. Krestnikov, Yu. G. Musikhin, N. A. Bert, P. S. Kop'ev, Zh. I. Alferov, N. N. Ledentsov and D. Bimberg, *InAs/InGaAs Quantum Dot Structures on GaAs Substrates Emitting at 1.3 μm*, Appl. Phys. Lett. **74**, 2815 (1999).

[93] H. Y. Liua, M. J. Steer, T. J. Badcock, D. J. Mowbray, M. S. Skolnick, F. Suarez, J. S. Ng, M. Hopkinson and J. P. R. David, *Room-Temperature 1.6 μm Light Emission from InAs/GaAs Quantum Dots with a Thin GaAsSb Cap Layer*, J. Appl. Phys. **99**, 046104 (2006).

[94] M. C. Schlamp, X. Peng and A. P. Alivisatos, *Improved Efficiencies in Light Emitting Diodes Made with CdSe(CdS) Core/Shell Type Nanocrystals and a Semiconducting Polymer*, Appl. Phys. Lett. **82**, 5837 (1997).

[95] S. Coe, W.-K. Woo, M. Bawendi and V. Bulović, *Electroluminescence from Single Monolayers of Nanocrystals in Molecular Organic Devices*, Nature **420**, 800 (2002).

[96] V. M. Ustinov and A. E. Zhukov, *GaAs-Based Long-Wavelength Lasers*, Semicond. Sci. Technol. **15**, Review: 41 (2000).

[97] V. I. Klimov, A. A. Mikhailovsky, S. Xu, A. Malko, J. A. Hollingsworth, C. A. Leatherdale, H.-J. Eisler and M. G. Bawendi, *Optical Gain and Stimulated Emission in Nanocrystal Quantum Dots*, Science **290**, 314 (2000).

[98] J. M. Gérard, B. Sermage, B. Gayral, B. Legrand, E. Costard and V. Thierry-Mieg, *Enhanced Spontaneous Emission by Quantum Boxes in a Monolithic Optical Microcavity*, Phys. Rev. Lett. **81**, 1110 (1998).

[99] M. Bayer, T. L. Reinecke, F. Weidner, A. Larionov, A. McDonald and A. Forchel, *Inhibition and Enhancement of the Spontaneous Emission of Quantum Dots in Structured Microresonators*, Phys. Rev. Lett. **86**, 3168 (2001).

[100] J. P. Reithmaier, G. Sęk, A. Löffler, C. Hofmann, S. Kuhn, S. Reitzenstein, L. V. Keldysh, V. D. Kulakovskii, T. L. Reinecke and A. Forchel, *Strong Coupling in a Single Quantum Dot-Semiconductor Microcavity System*, Nature **432**, 197 (2004).

[101] T. Yoshie, A. Scherer, J. Hendrickson, G. Khitrova, H. M. Gibbs, G. Rupper, C. Ell, O. B. Shchekin and D. G. Deppe, *Vacuum Rabi Splitting with a Single Quantum Dot in a Photonic Crystal Nanocavity*, Nature **432**, 200 (2004).

[102] E. Peter, P. Senellart, D. Martrou, A. Lemaître, J. Hours, J. M. Gérard, and J. Bloch, *Exciton-Photon Strong-Coupling Regime for a Single Quantum Dot Embedded in a Microcavity*, Phys. Rev. Lett. **95**, 067401 (2005).

[103] C. de Mello Donegá, S. G. Hickey, S. F. Wuister, D. Vanmaekelbergh and A. Meijerink, *Single-Step Synthesis to Control the Photoluminescence Quantum Yield and Size Dispersion of CdSe Nanocrystals*, J. Phys. Chem. B **107**, 489 (2003).

[104] A. Irman, *Modification of Spontaneous Emission of Quantum Dots by Photonic Crystals*, Master Thesis, University of Twente (2003).

[105] A. F. van Driel, *Light Sources in Semiconductor Photonic Materials*, Ph.D. thesis, Utrecht University, ISBN: 90-393-4250-4 (2006).

CHAPTER 4

DIRECTIONAL EMISSION SPECTRA FROM PHOTONIC CRYSTALS

We have performed angle-resolved measurements of spontaneous-emission spectra from laser dyes and quantum dots in opal and inverse-opal photonic crystals. Pronounced directional dependencies of the emission spectra are observed: angular ranges of strongly reduced emission adjoin with angular ranges of enhanced emission. It appears that emission from embedded light sources is affected both by the periodicity and by the structural imperfections of the crystals: the photons are Bragg diffracted by lattice planes and scattered by unavoidable structural disorder. Using a model comprising diffuse light transport and photonic band structure, we quantitatively explain the directional emission spectra. This work provides detailed understanding of the transport of spontaneously emitted light in real photonic crystals, which is essential in the interpretation of quantum-optics in photonic bandgap crystals and for applications wherein directional emission and total emission power are controlled.

4.1 Introduction

Control over spontaneous emission is of keen interest for applications, and therefore emission properties of sources such as atoms, dyes and quantum dots are intensively investigated. The decay dynamics of the emitter excited state, as discussed elsewhere in this thesis, are proportional to the local radiative density of states (LDOS). In 3D photonic crystals pronounced variations of the LDOS are predicted even in the absence of a photonic bandgap [1, 2], which give rise to angle-independent variations of the total emission. Recently LDOS effects on spontaneous emission have been experimentally demonstrated: Using 3D photonic crystals, considerable variations of the emission rates in large band widths were obtained in both continuous-wave (cw) total-emission power experiments [3, 4] and in time-resolved lifetime experiments [5, 6]. While lifetime experiments

provide a direct measurement of decay rates, it is important to quantitatively interpret concomitant emission spectra, for instance, to confirm that light sources inside the crystal are probed. Cw experiments, on the other hand, rely on a comparison of angle-integrated spectra with a homogeneous medium. In the latter case a complete understanding of all angle-dependent effects, that is Bragg diffraction, on the propagation of light is crucial. In this Chapter we present such a quantitative analysis.

In contrast to decay rates, emission spectra of sources embedded in photonic crystals are strongly directional [7–12]. Particular frequency ranges of the spectra are suppressed in certain directions forming stopbands, whose center frequencies and the widths are described by the photonic dispersion relation. Besides Bragg diffraction, which is an effect of the order of the periodic structure, light propagating inside the structure also *feels* disorder: polydispersity, roughness and misarrangements of the building blocks [13]. This deviation from perfect periodicity affects the interference-induced properties of photonic crystals. Previous work on the effect of disorder on spontaneous emission includes the realization that disorder determines the depth of stopbands [9, 11]. Furthermore, the first observations of enhanced emission in the range of first and second-order stopbands were also related to disorder-induced redistribution of emitted photons [14]. While the propagation of light from external sources has been studied in great detail [15–17], a quantitative explanation of the behavior of light emission from internal sources has lacked sofar.

Here we present strongly frequency-dependent angular distributions of spontaneous emission from a laser dye in polystyrene opals and from quantum dots in titania inverse opals in the frequency range around the first-order Bragg diffraction (L-gap). We compare the data to a theoretical model that unifies effects of structural disorder and photonic crystal properties [17]. Angle-dependent internal reflection due to the photonic gaps plays a key role in our model. The theory quantitatively explains both the enhancement and reduction of light in certain propagation directions that were observed experimentally. The excellent agreement confirms that the propagation of light in a photonic crystal is well understood for frequencies around the L-gap. Furthermore, we show that by analyzing the exit emission distributions, one can reveal stopbands in the quantum dot spectra. Such an analysis should be performed before any quantum-optical experiments since it unambiguously proves the effect of the photonic crystal on emission. We finally discuss the applicability of photonic crystals to improve the emission efficiency of light sources.

4.2 Experimental details

4.2.1 Samples

We have studied emission from dyes in polystyrene opals and from quantum dots in titania inverse opals. The photonic crystals used in this experiment are described in Chapter 3. We studied 4 polystyrene samples with lattice parameters a = 178 and 365 ± 8 nm and 8 titania samples with lattice parameters a = 370, 420, 500, 580 and 650 ± 15 nm. The polystyrene opals were doped with the laser dye Rhodamine 6G (R6G) by soaking them for 30 minutes in a dilute solution (10^{-6} mol/l) of the dye in ethanol. Afterwards, to remove the dye from the sample surface, the samples were rinsed in ethanol and dried. To estimate an upper bound to the density of the dye, we assume that the infiltrating solution completely fills the air voids in the opals, and that, in the process of drying, the dye molecules distribute uniformly on the surfaces of the spheres inside the opals. Knowing the volume of the air voids in each unit cell of the opals (0.26 a^3) and the dye concentration, we arrive at no more than 10 dye molecules per unit-cell inner surface [(1)] (for opals with lattice parameter a = 365 nm). While this surface density increases linearly with the lattice parameter a, the average distance between the dye molecules remains more than 2 orders of magnitude away from the typical intermolecular distances where reabsorption and energy-transfer processes could play a role [18]. Before emission experiments, we performed a selective photobleaching [(2)] of the dye at the surface of opal photonic crystals in order to ensure that the emission is recorded only from the bulk of the crystal, and not from the crystal surface [9]. The whole surface was illuminated for up to 1 hour by an intense laser beam at the Bragg angle for the pump frequency. At this angle the pump intensity decreases exponentially with depth, which implies that the dye bleaches within the first few crystal layers. However, our experimental results were found to be almost independent of the amount of bleaching, thus indicating that emitters in the bulk of the photonic crystals provide the dominating contribution to the measured emission intensity.

The titania inverse opals were doped with ZnSe-coated CdSe colloidal quantum dots (QDs), which were introduced in Chapter 3. The inverse opals were soaked for 24 hours in a dilute suspension (10^{-7}mol/l) of the QDs in a mixture of 50% chloroform and 50%

[(1)] In an *fcc* structure consisting of spheres of radius r with a lattice parameter $a = \sqrt{8}r$, the inner surface per unit cell A equals $4 \cdot 4\pi r^2 = 2\pi a^2$. Therefore the surface density N_s of the dye is proportional to $0.26a^3/2\pi a^2 \sim a$.
[(2)] Photobleaching is a photoinduced irreversible modification of dye molecules, which makes them non-fluorescent. Typically, it happens because of oxidation of dye molecules that damages them permanently.

butanol. In chloroform only, which is an apolar solvent, the QDs deposit only on the surface of the titania inverse opals. We have found that by adding butanol, a polar solvent, the infiltration was successfully performed. This was checked by selectively probing QDs positioned in the bulk of a test sample that was cut in two pieces. After the infiltration, the samples were rinsed in chloroform and dried. We used the same estimation in order to get the maximum number of QDs per unit cell in the inverse opals. For samples with the largest lattice parameter a = 650 nm, this concentration is 15 QDs per cubic unit cell and is sufficiently low to avoid energy-transfer processes and reabsorption. In order to minimize photooxidation and contamination of the QDs,[3] the inverse opals were infiltrated with the QDs in a nitrogen-purged glove box (Braun) and held in a sealed chamber under a 1.7 mbar nitrogen atmosphere during the optical measurements. No bleaching at the external surface could be performed for the QDs, however a detailed analysis of the angular emission data (see below) demonstrates that light emission from the QDs from the bulk dominates.

4.2.2 Experimental set-up

The light sources inside the crystals were excited by a cw Ar-ion laser (λ = 497 nm) with the power at the sample around 10 μW. At this pump power, we did not observe any effects of bleaching of the dye during the emission experiments. Figure 4.1 shows the experimental set-up used to measure emission from light sources inside photonic crystals. To focus the pump beam on the sample surface a fiber-coupled microscope objective was used. The beam was focused to a spot of about 30 μm in diameter at an incident angle θ_p relative to the surface normal, usually $\theta_p \approx 25°$. In order to acquire emission spectra as a function of the detection angle θ_e relative to the surface normal, the sample was mounted on a rotation stage. The surface normal is parallel to the 111 reciprocal lattice vector G_{111}. In order to illuminate the same area irrespective of θ_e, the fiber-coupled objective (O_1) is mounted on the same rotation stage as the sample. In this way, the angle of incidence θ_p between the pump beam and the surface normal is kept constant. The advantage over previous experiments, where the sample was rotated with respect to both the pump and detection beams, is that the absolute intensity of the angle-dependent spectra

[3] Photooxidation of a QD is a process when oxygen penetrates the ZnSe passivating layer and reacts with the CdSe core, which results in a growth of a quenching oxide layer. Consequently, the QD is gradually bleached due to increased number of quenching states [19]. Because the oxidation also lowers the size of the CdSe core, the emission spectrum shifts to higher frequencies.

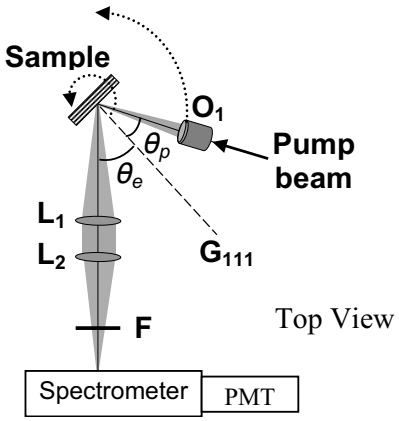

FIGURE 4.1: Scheme of the experimental set-up. The pump beam is focused onto the sample at incident angle θ_p by the objective O_1 (f = 7.3 cm, NA = 0.05). Luminescence within a cone centered at detection angle θ_e relative to the surface normal is collected by the lens L_1 (f = 12 cm) and imaged on the spectrometer slit by the lens L_2 (f = 12 cm). A color filter F prevents scattered pump light from entering the prism spectrometer. The angle θ_e is varied by rotating the rotation stage, which carries the sample holder, the fiber and the objective O_1; whereas the incident angle θ_p is kept fixed.

can be reliably compared. The position of the pump spot on the sample is monitored with a microscope. The emitted light is collected within a cone of 15° full width around the angle θ_e, imaged on the slit of a prism spectrometer (Carl Leiss). The width of the spectrometer slit was set to provide a spectral resolution of ~ 85 cm^{-1} (3 nm). A microchannel plate photomultiplier tube (MCP-PMT, Hamamatsu R3809U) was used to detect the emitted photons. The angle-resolved spectra are usually measured at the detection angles from 0° to 75° at intervals of 15°. The measured spectra are corrected for the dark count of the MCP-PMT. The shapes of the spectra are confirmed to be independent of the pump intensity, and the emitted intensity is linear with the pump power.

4.3 Diffuse light transport in photonic crystals

4.3.1 Escape function

In real photonic structures, defects in the arrangement of the building blocks are always present and cause random multiple scattering of light. This means that all light emitted

in such photonic structures becomes diffuse on length scales equal to the transport mean free path ℓ, which is often much smaller than the thickness of the sample L [13]. For example, our opals and inverse opals have mean free paths of about 15 μm [20], whereas the thickness of the samples is about 200 μm. Thus, even though light generated inside a photonic crystal is diffracted by the crystal planes, this effect is smeared out by the random multiple scattering while the light propagates through the bulk towards the crystal surface (see Fig. 3.3). Only at distances from the crystal-air interface z smaller than ℓ, where the photons emanate ballistically towards the interface after a last scattering event, the effect of Bragg diffraction is not destroyed by the scattering. Hence the diffuse emission acquires a directional dependence only when it exits the crystal [17].

We consider the ratio of the mean free path ℓ to the attenuation length for Bragg diffraction L_B in order to estimate the attenuation of emission caused by Bragg diffraction, as proposed in Ref. [11]. Since the mean free path ℓ is larger than the Bragg attenuation length L_B (typically $\ell/L_B \sim 2-5$ [20]), an attenuation in the stopband equal to $1 - L_B/\ell$ = 50 % to 80 % is predicted, which is in agreement with our observations. As will be discussed later, the stopband attenuations are obtained directly from reflectivity measurements, therefore, the mean free path ℓ is not an explicit parameter in our theoretical model.

In the present work we investigate directional properties of light emitted by sources from 3D photonic crystals and compare to a model of diffuse light transmission through opaque media [21–23] extended to photonic crystals [17]. Based on the diffusion theory, the intensity of light $I(\omega, \mu_e)$ with frequency ω that exits the sample at external angles between $\theta_e = \cos^{-1}(\mu_e)$ and $\cos^{-1}(\mu_e + d\mu_e)$ relative to the surface normal is equal to

$$I(\omega, \mu_e)d\mu_e = I_{tot}(\omega)P(\omega, \mu_e)d\mu_e. \tag{4.1}$$

Here $I_{tot}(\omega)$ is the total spontaneous emission power - the spectrum of the light sources integrated over the exit angles θ_e. For sources with a low quantum efficiency or with homogeneously broadened spectra, $I_{tot}(\omega)$ is proportional to the LDOS, as demonstrated in Ref. [3].[(4)] The distribution $P(\omega, \mu_e)$ is defined as

$$P(\omega, \mu_e) = \mu_e \frac{n_e^2}{n_i^2}\left(\frac{1 + \bar{R}(\omega)}{1 - \bar{R}(\omega)} + \frac{3}{2}\mu_i\right)[1 - R(\omega, \mu_i)], \tag{4.2}$$

where n_e and n_i are average refractive indices outside and inside the sample [25], respectively. μ_e and μ_i are related by Snell's law. $R(\omega, \mu_i)$ is an angle-dependent internal-

[(4)] In Ref. [24], this proportionality was incorrectly related to inhomogeneous broadening.

reflection coefficient that yields an angle-averaged internal-reflection coefficient $\bar{R}(\omega)$:

$$\bar{R}(\omega) = \frac{3C_2(\omega) + 2C_1(\omega)}{3C_2(\omega) - 2C_1(\omega) + 2}\,, \tag{4.3}$$

$$C_n(\omega) = \int_0^1 R(\omega, \mu_i)\mu_i^n d\mu_i\,. \tag{4.4}$$

From diffusion theory, $\bar{R}(\omega)$ determines the so-called extrapolation length that sets the boundary conditions of the diffuse intensity [21–23]. The normalized function $P(\omega, \mu_e)$ describes the distribution of emission intensity over the escape angles and will be called the "escape function". In absence of reflection effects, the escape distribution tends to the well-known Lambertian distribution of diffuse surfaces.

In random media such as powders or macroporous sponges the internal-reflection coefficient $R(\omega, \mu_i)$ is barely frequency dependent [26], and propagation through the interface is well described by Fresnel reflection model assuming an average refractive index. The angular dependence of the escape function $P(\omega, \mu_e)$ agrees well with experiments on random media [22, 23]. For highly dispersive photonic crystals, however, Fresnel model cannot describe the internal reflection since light escaping from a depth $z < \ell$ from the crystal surface is Bragg attenuated for angles and frequencies inside a stopband. We model the strong angle and frequency dependent internal reflection with photonic band structures. At a particular frequency ω^* where a stopband is present, the internal reflectivity $R(\omega^*, \mu_i)$ blocks the emission in the directions of the stopband (a range of μ_i^*'s related to ω^* by the photonic band structure) and therefore reduces the escape function $P(\omega^*, \mu_e^*)$, *cf.* Eq. 4.2. The presence of the stopband raises the angle-integrated reflectivity $\bar{R}(\omega^*)$, which enhances the escape function $P(\omega^*, \mu_e)$ for angles outside the stop band. Thus, the escape function is strongly non-Lambertian in a photonic crystal, showing clear suppressions or enhancements.

4.3.2 Internal-reflection coefficient

To model the internal-reflection coefficient $R(\omega, \mu_i)$, we have taken into consideration calculated photonic band structures. Figure 4.2a shows the photonic band structure for polystyrene opals calculated along the LU and LK lines of the Brillouin zone in the frequency range around the first-order stopgap (L-gap) that is related to optical Bragg diffraction by (111) planes parallel to the sample surface. The emission spectrum of R6G is in the low-frequency limit relative to the stopbands of opals with a lattice parameter

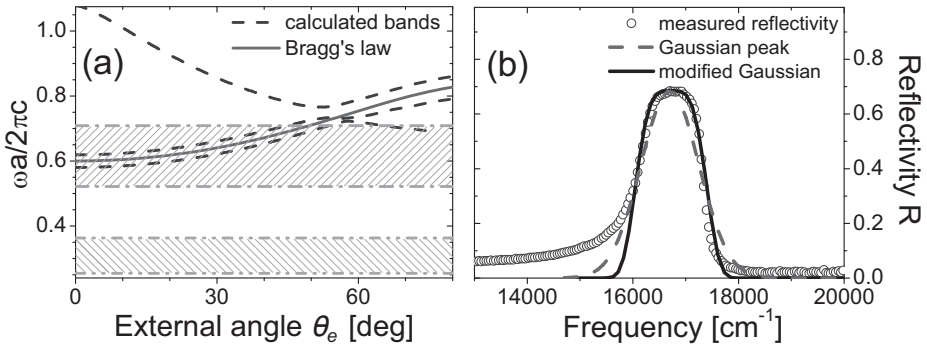

FIGURE 4.2: (a) Photonic band structure for polystyrene opals (dashed curves), center frequency of the stopband vs. detection angle θ_e according to Bragg's law (solid curve), the frequency range of R6G emission is shown for opals with lattice parameters a = 178 and 365 nm (hatched regions between the dash-dot-dotted lines and dash-dotted lines, respectively). (b) Normal-incidence reflectivity spectrum for a polystyrene opal with a lattice parameter a = 365 nm. Circles are measured values, the black solid curve is a fit with the modified Gaussian reflectivity peak (Eq. 4.5), the dashed curve is a fit with a Gaussian reflectivity peak.

a = 178 nm (region confined by the dash-dot-dotted lines). Consequently, this sample is effectively homogeneous for the emission frequencies, and therefore it can serve as a reliable reference. For these non-photonic crystals we used the Fresnel model to describe the internal reflection. In Figure 4.2a one can also see the frequency gap between the two lowest bands (dashed curves), which obeys Bragg's law (solid curve) within the frequency range of R6G emission for the opals with a lattice parameter a = 365 nm (region confined by the dash-dotted lines). Therefore, the angular dependence of the center frequency of the L-gap is modeled with the solid curve, *i.e.*: $\omega_c(\mu_i) = \omega_c(\mu_i = 1)/\mu_i$. To investigate the frequency dependence of the reflectivity, we have performed reflectivity experiments on the samples using external incident plane waves, since this technique reveals the center frequencies and the widths of stopbands [16, 27, 28]. Figure 4.2b shows a normal-incidence reflectivity spectrum measured from an opal with lattice parameter a = 365 nm (circles). The reflectivity peak does not agree well with a Gaussian (dashed curve). As an improved model, we propose a modified Gaussian (Fig. 4.2b, solid curve):

$$R_1(\omega, \mu_i) = A_1(\mu_i) \exp\left[- \frac{(\omega - \omega_c(\mu_i))^4}{2(\Delta\omega(\mu_i))^4} \right], \tag{4.5}$$

where $A_1(\mu_i)$ is the magnitude of the internal-reflection coefficient and $\Delta\omega(\mu_i)$ is the width parameter. This peak shape is seen to fit the measurements well for frequencies > 16000 cm^{-1}. At frequencies below the stopband, *i.e.*, below 16000 cm^{-1}, a deviation from the model is observed. We attribute this deviation to Fresnel reflection, which is important only in the low-frequency limit and therefore is not relevant for the escape function of photonic samples. The width of the L-gap $\Delta\omega(\mu_i)$ hardly varies with μ_i within the range of the dye emission, therefore it is taken to be constant in our model. The magnitude of the internal-reflection coefficient $A_1(\mu_i)$ decreases with μ_i because at larger internal angles $\theta_i = \cos^{-1}(\mu_i)$ the path length for the light to become Bragg attenuated increases with μ_i, and this increases the probability of scattering at $z < L_B$. The value of $A_1(\mu_i)$ at $\mu_i = 1$ is taken from the normal-incidence reflectivity experiments. Thus, for the opals with $a = 365$ nm we have $A_1(\mu_i) = 0.7\mu_i$, see Fig. 4.2b.

Emitted light that is scattered within a depth $L_B < z < \ell$ towards the exit interface can also be redirected by Bragg diffraction by the sets of $(11\bar{1})$ planes, which are oriented at $\theta_i = 70.5°$ to the (111) planes and the surface normal. The internal-reflection coefficient $R_2(\omega, \mu_i)$ for Bragg diffraction by $(11\bar{1})$ lattice planes is modeled similarly to $R_1(\omega, \mu_i)$. Taking into account that we measure emission from many azimuthally variously oriented crystal domains, the reflectivity $R_2(\omega, \theta_i)$ is averaged over the azimuthal angles ϕ between the LK and LU lines, yielding:

$$R_2(\omega, \theta_i) = \frac{3}{\pi} \int_0^{\pi/3} A_2(\theta_i, \phi) \exp\left[- \frac{(\omega - \omega_c(\theta_i, \phi))^4}{2(\Delta\omega(\theta_i))^4} \right] d\phi, \tag{4.6}$$

where $A_2(\theta_i, \phi) = A_2(70.5°, 0°)\cos(\theta_i - 70.5°)\cos(\phi)$ where $A_2(70.5°, 0°) = 0.7$. The total internal-reflection coefficient $R(\omega, \mu_i)$ is calculated as a sum of the $R_1(\omega, \mu_i)$ and $R_2(\omega, \cos(\theta_i - 70.5°))$ modified Gaussian peaks. We expect this model of the angle- and frequency-dependent internal reflectivity to capture the essential frequency dependence of the first-order photonic stopbands in polystyrene opals.

In the case of the titania inverse opals we apply the same escape model to explain our experimental data. However, for calculations of the internal-reflection coefficient $R(\omega, \mu_i)$, Bragg diffraction from other lattice planes must also be included. This difference compared to polystyrene opals appears since titania inverse opals are more strongly photonic and the measurements were performed at higher reduced frequencies ($a/\lambda = \omega a/2\pi c$). Moreover, the resulting stopbands occur at lower detection angles θ_e in these crystals than in the polystyrene opals, as a consequence of the lower average refractive index. Therefore Bragg's law is not a sufficient approximation and is not used to model the angular

dependence of the stopbands in the titania inverse opals. Instead, the full band structure model is employed, in which we take into account multiple Bragg wave coupling [11, 28]. For the inverse opals, this model was already successfully tested on diffuse transmission experiments [17].

4.4 Results and Discussion

4.4.1 Emission from dye in polystyrene opals

Reflectivity measurements at normal incidence of polystyrene opals (Fig. 4.2b) reveal that the relative width of the first-order stopband is $\Delta\omega/\omega \approx 0.075$. For opals with a lattice parameter a = 365 nm this means a stopband in the range 16100 - 17300 cm^{-1} for light escaping the crystal normally to the surface. The dye R6G emits in the range of 15000 - 20000 cm^{-1}, and hence we expect to observe directional-dependent emission of the dye from the opals with a = 365 nm. Figure 4.3a displays the emission spectra at selected detection angles for such doped opals. It is clearly seen that the shapes of the spectra are affected by the photonic crystal. The emission is suppressed by the crystal for $\theta_e = 0°$ in the spectral range from 16000 to 17500 cm^{-1}. With increasing angle θ_e the low-frequency parts of the emission recover, and the suppressed emission range shifts to

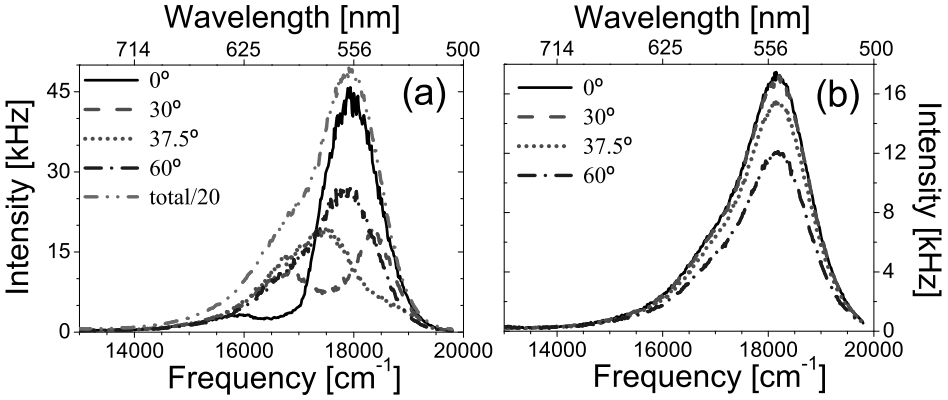

FIGURE 4.3: Emission spectra of R6G in polystyrene opals with lattice parameters a = 365 nm (a) and a = 178 nm (b). The solid curves are obtained at $\theta_e = 0°$, dashed curves at $\theta_e = 30°$, dotted curves at $\theta_e = 37.5°$, and dash-dotted curves at $\theta_e = 60°$. The dash-dot-dotted curve in (a) indicates the total emission spectrum $I_{tot}(\omega)$. Note, the spectra are not scaled to each other.

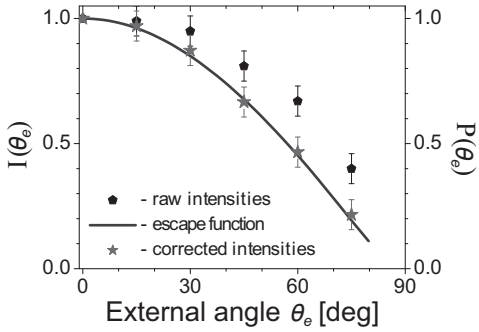

FIGURE 4.4: Angular distribution of the R6G emission from a polystyrene opal with a lattice parameter a = 178 nm. The pentagons indicate the intensity measured at the spectral maximum (ω = 17860 cm^{-1} or λ = 560 nm), the solid curve is the calculated escape function with Fresnel internal-reflection coefficient. Measured intensities corrected for the detection efficiency of the set-up are displayed as stars. All data are normalized at $\theta_e = 0°$.

higher frequencies, as expected from Bragg's law for a photonic stopband from a single set of lattice planes. In contrast, the shape of the spectra from an opal with a lattice parameter a = 178 nm remains unchanged (Fig. 4.3b). The sample is not photonic for the frequency range considered: the frequencies of R6G emission lie far below the first-order stopband in the opal with this lattice parameter.

Before studying spontaneous emission from photonic samples we have verified the applicability of the above-mentioned model of diffuse light transport on the non-photonic, reference samples. We use Fresnel reflection to describe the angular-dependent internal-reflection coefficient, taking an average refractive index $n_{\mathrm{av}} = 1.44$, which is derived from the polystyrene filling fraction $\varphi \approx 74$ % in opals and the refractive index of polystyrene $n = 1.59$. We record the intensity at the maximum of the emission spectrum as a function of the exit angle θ_e relative to the measurement at $\theta_e = 0°$. The relative intensity $I(\theta_e)$ is compared to the escape function $P(\theta_e)$ in Figure 4.4. While the expected decrease with angle is observed, it is clear that the calculated intensity differs systematically from the measured data. This deviation appears to be caused by an angle-dependent detection efficiency as a result of the increase with θ_e of the projection of the spectrometer slit on the sample. Correcting the measured intensity $I(\omega, \mu_e)$ for the detection efficiency $D(\mu_e)$ (see Appendix A) yields the corrected intensity $I_c(\omega, \mu_e) = I(\omega, \mu_e)/D(\mu_e)$ displayed as star symbols in Fig. 4.4. The agreement between the corrected intensity and the calculated

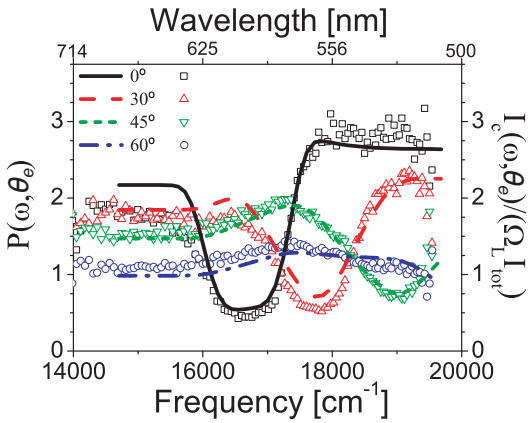

FIGURE 4.5: R6G emission from a polystyrene opal with lattice parameter a = 365 nm. The scatter plots represent the measured spectra corrected for the angular aperture of the collecting lens Ω_L and divided by the total emission spectrum $I_{tot}(\omega)$. The calculated escape functions are plotted with solid curves. The black solid curve and squares are for $\theta_e = 0^0$, red dashed curve and triangles are for $\theta_e = 30^0$, green inverted triangles and short-dashed curve are for $\theta_e = 45^0$ and blue circles with dash-dotted curve are for $\theta_e = 60^0$.

escape function is excellent. With the proper account of the detection efficiency, the angular distribution of emission escaping the reference samples is thus fully understood. In all experimental data presented further, the detection efficiency has been included.

In the case of the photonic samples the exit distribution of emission strongly depends on the frequency ω as mentioned above: $P(\omega, \theta_e) = I_c(\omega, \theta_e)/I_{tot}(\omega)$. The total emission spectrum $I_{tot}(\omega)$ is determined by discretely summing the angle-resolved spectra $I_c(\omega, \theta_e)$ weighted by $2\pi \sin(\theta_e) d\theta_e$ to approximate the integration over 2π solid angle. The spectra from Figure 4.3a divided by the total emission spectrum $I_{tot}(\omega)$ are plotted in Figure 4.5 (symbols) together with the calculated escape function $P(\omega, \theta_e)$ (curves). We observe a good agreement between our experiment and theory. The escape function hardly varies with frequency in the low-frequency region ≤ 15600 cm^{-1}, while it does depend on the detection direction. In contrast, at higher frequencies strong variations are seen compared to the low-frequency range. At the exit angle $\theta_e = 0°$, the escape function is significantly reduced in the spectral range from 16000 to 17500 cm^{-1} by the stopband centered at $\omega = 16700$ cm^{-1} due to internal Bragg diffraction, which is described by the term $[1 - R(\omega, \mu_i)]$ in Eq. 4.2. The change of the center frequency as well as the decrease

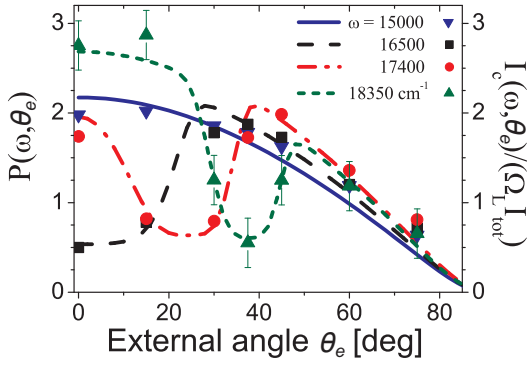

FIGURE 4.6: Intensity ratios $I_c(\theta_e)/I_{tot}$ corrected for the lens aperture Ω_L as a function of the exit angle θ_e for a polystyrene opal with a lattice parameter a = 365 nm for frequencies ω = 15000, 16500, 17400 and 18350 cm^{-1} (blue inverted triangles, black squares, red circles and green triangles). The indicated error-bars are typical for all measurements. The corresponding curves represent the calculated escape distributions (for reduced frequencies $\omega a/2\pi c$ = 0.55, 0.6, 0.64 and 0.67, respectively).

in the attenuation of emission inside the stopband with increasing exit angle θ_e are well described in our model by the frequency and angular dependent internal-reflection coefficient $R(\omega, \mu_i)$. At $\theta_e = 60°$, the stopband has moved out of the spectral range of R6G.

Figure 4.5 also shows a peculiar feature: the frequency ranges where the emission is inhibited along certain directions, adjoin with the ranges where emission is *increased* along the same directions. Such an increase appears at the blue side of the stopband at $\theta_e = 0°$ and 30°, and at the red side of the stopband at $\theta_e = 45°$ and 60°. This enhanced escape probability in the frequency range 16000 - 19500 cm^{-1} along the directions, which do not coincide with the stopband, is reflected in our model for $P(\omega, \mu_e)$ (Eq. 4.2) as an increase of the angle-averaged internal-reflection coefficient $\bar{R}(\omega)$. The good agreement between experiments and theory confirms a qualitative attribution of such enhancements to diffuse escape effects [14]. Moreover it unambiguously demonstrates that our experimental observation of the emission enhancement is not due to Bragg standing wave effects proposed in Reference [29], but is related to diffusion of light.

In Figure 4.6 we compare the experimentally determined intensity distributions (symbols) for several fixed frequencies with the calculated ones (curves) as functions of the exit angle θ_e. The experimental values of $P(\theta_e)$ were obtained by dividing the emission

$I_c(\theta_e)$ by the total emission spectrum I_{tot} and correcting for the angular aperture of the collecting lens Ω_L. For the frequency $\omega = 15000$ cm^{-1}, below the stopband, the distribution follows the Lambertian distribution and is similar to the exit distribution from the non-photonic sample (Fig. 4.4). For the frequencies above the red edge of the stopband we observe strongly non-Lambertian behavior. For the frequency $\omega = 16500$ cm^{-1} emission is suppressed relative to the Lambertian distribution in the range of the exit angles from $\theta_e = 0°$ to $20°$. This range moves to larger exit angles for the frequency $\omega = 17400$ cm^{-1} in qualitative agreement with Bragg's law. For $\omega = 18350$ cm^{-1} the suppression observed around $\theta_e = 40°$ is preceded by a considerable increase of emission in the angle range $0°$ to $20°$. A qualitative explanation of this effect is as follows. Some escape directions are blocked by internal Bragg diffraction, and diffusion eventually distributes this back-reflected light along the remaining directions. Thus, light is more likely to exit the crystal along these allowed directions. From Figures 4.5 and 4.6 we conclude that the escape function is in excellent agreement with the measured angle-dependent spectra. To the best of our knowledge, the current work provides the first quantitative modeling of spontaneous emission spectra in 3D photonic crystals.

4.4.2 Emission from quantum dots in titania inverse opals

The titania inverse opals interact with light more strongly than the polystyrene opals owing to their inverse structure and high refractive-index contrast ($m \approx 2.7$). The concomitant large modifications of the LDOS make these inverse opals very attractive for control of propagation and spontaneous emission of light [3, 5]. Figure 4.7 shows emission spectra of CdSe QDs in a titania inverse opal with lattice parameter $a = 420$ nm for selected detection angles θ_e (curves) and a normal-incidence reflectivity spectrum (circles) from the same inverse opal. No significant changes in the spectral shapes due to internal Bragg diffraction are observed, because the relative spectral width of the QD ensemble ($\Delta\omega/\omega < 0.06$) is considerably smaller than the width of the stopband of the photonic crystal ($\Delta\omega/\omega \approx 0.16$). This shows that the escape distribution $P(\omega, \theta_e)$ does not vary significantly within the frequency range of the QD spectrum. In contrast, a strong angular dependence of the emission intensity is apparent in Fig. 4.7. As a consequence, effects of Bragg diffraction are most convincingly observed by recording the angular dependencies at the spectral maxima of the emission spectra.

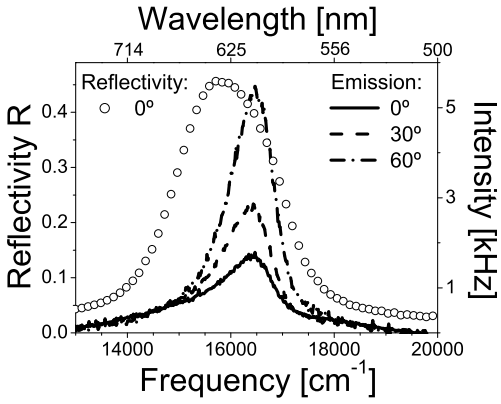

FIGURE 4.7: Normal-incidence reflectivity spectrum (circles) and emission spectra of CdSe quantum dots (curves) in a titania inverse opal with a lattice parameter $a = 420$ nm. The emission spectra are measured at $\theta_e = 0°$, $30°$ and $60°$ (shown by the solid, dashed and dash-dotted curves, respectively).

In Figure 4.8a we present escape distributions from titania inverse opals with lattice parameters $a = 370$ and 420 nm at frequency $\omega = 16390$ cm^{-1}, and with a lattice parameter $a = 500$ nm at $\omega = 15870$ cm^{-1}. Both measured (symbols) and calculated (curves) values are shown. For the crystal with lattice parameter $a = 370$ nm, the center frequency of the QD spectrum lies below the stopband, and thus, the escape function follows the Lambertian distribution. A large deviation from the Lambertian distribution is observed for the QD emission from the crystals with larger lattice parameters. In the crystals with $a = 420$ nm, the emission is strongly reduced in the range of the angles from $\theta_e = 0°$ to $35°$, and it is enhanced at higher exit angles. For the crystals with $a = 500$ nm, the suppression is shifted to the range of $\theta_e = 20°$ to $45°$, as expected for photonic gaps at higher reduced frequency ($a/\lambda = \omega a/2\pi c$), and in excellent agreement with our theoretical predictions. The stopband ranges are noticeably wider than that in the case of the polystyrene opals (Fig. 4.6), which is due to a wider frequency range of the stopband in the titania inverse opals. To the best of our knowledge, this is the first demonstration of photonic crystal bands in the emission spectra of confined excitons in QDs.

Figure 4.8b shows the photonic band structure for a titania inverse opal calculated along the LU line. The hatched regions indicate the stopband caused by Bragg diffraction by (111) lattice planes. In the angular range from $\theta_e = 35°$ to $55°$, multiple Bragg wave

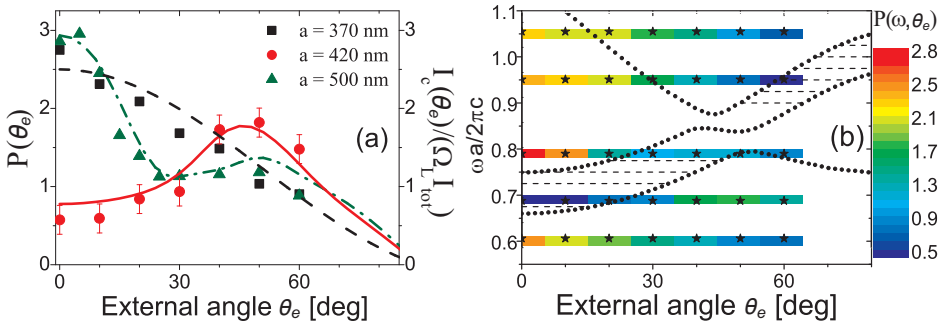

FIGURE 4.8: (a) Escape distribution as a function of the exit angle θ_e for titania inverse opals with lattice parameters a = 370 and 420 nm at ω = 16390 cm^{-1} (λ = 610 nm, black squares and red circles, respectively), and with a lattice parameter a = 500 nm at ω = 15870 cm^{-1} (λ = 630 nm, green triangles). The corresponding curves represent the calculated distributions. (b) Photonic band structure for the inverse opals along the LU line (black dotted curves). The hatched regions indicate the stopband caused by Bragg diffraction by (111) lattice planes. The horizontal bars represent the reduced center frequencies of the QD emission from the crystals with lattice parameters (bottom to top) a = 370, 420, 500, 580 and 650 nm. The colors of the bars indicate the values of the escape function $P(\omega, \theta_e)$ obtained from the measurements at exit angles shown by the stars.

coupling from (111) and (200) diffracted waves takes place [11, 28]. The horizontal bars represent the reduced center frequencies of the QD emission from the inverse opals with lattice parameters a = 370, 420, 500, 580 and 650 nm. The colors of the bars indicate the measured values of the escape function $P(\omega, \theta_e)$. For reduced frequencies around the stopbands, it is seen that inhibited escape probability appears in the angular ranges of the stopbands, whereas enhanced escape is found outside the stopbands. Hence, the photonic crystals are seen to "funnel" light along certain allowed directions.

For experiments on QD emission in photonic crystals, the good agreement between the experimentally obtained escape distributions and the calculated ones confirms that the light emanating from inside the crystals is diffuse. Importantly, it also confirms that the observed emission is dominated by sources inside the bulk of the crystal. We can exclude that light sources on the sample surface contribute significantly: their emission would give rise to an angle-independent component of the intensity, which is not observed by us. Furthermore, observation of stopbands in emission spectra is important for successful lifetime experiments or other quantum-optical studies of light sources in photonic crystals.

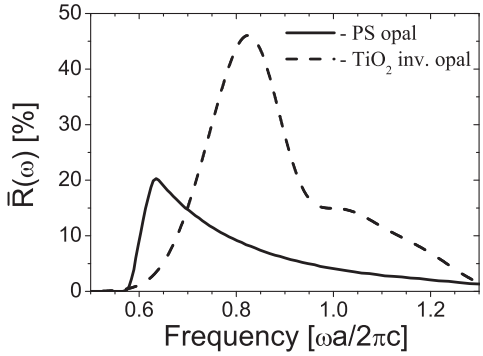

FIGURE 4.9: The angle-averaged internal reflectivity $\bar{R}(\omega)$ for the polystyrene opals (solid curve) and for the titania inverse opals (dashed curve) according to the diffusion model, in which only the first-order Bragg diffraction is taken into account. $\bar{R}(\omega)$ determines the enhancement of the escape probability outside a stopband direction.

The stopbands are evidence that the emission from the light sources is strongly coupled to the photonic crystals, and they are a prerequisite for time-resolved experiments of changes in the emission decay rate caused by a modified LDOS [5].

Based on the close accordance of the experiments with the model, we can extract the angle-averaged internal-reflection coefficient $\bar{R}(\omega)$. Figure 4.9 shows that $\bar{R}(\omega)$ is as large as 50 % for the titania inverse opals and up to 20 % for the polystyrene opals. The internal-reflection coefficient varies strongly with frequency in contrast to the frequency-independent $\bar{R}$ in random media. The coefficient increases with solid angle for Bragg reflection, starting from the low-frequency edge of the L-gap. For the opals, the maximum $\bar{R}$ occurs at the high-frequency edge of the L-gap, where the reflecting stopbands extend over the largest solid angle [27]. For the inverse opals, the maximum $\bar{R}$ occurs at higher reduced frequencies in the range of multiple Bragg wave coupling ($\omega a/2\pi c \sim 0.85$) [11]. The shoulder near 1.0 is attributed to inclusion of (200) reflection condition in our model. In a more elaborate escape-model with additional diffraction conditions, we may expect additional peaks in the angle-averaged reflection coefficient at even higher frequencies. Since the inverse opals interact more strongly with light than the opals, their stopbands are wider and hence the angle-averaged reflectivity is larger, which is in agreement with our observations.

A closer consideration of the reflectivity coefficients can serve to optimize the spontaneous emission yield of light sources (atoms, dyes or quantum dots) embedded inside

thick photonic crystals ($L > \ell$). Such an optimization can be achieved either via the excitation of the sources, via their emission, or both. First, the excitation efficiency can be increased by realizing that increased escape probability also implies an increased probability for excitation light to enter a photonic crystal. Thus, by tuning an excitation beam to frequencies and angles of high escape, the combined action of diffusion and Bragg diffraction retain relatively more excitation light inside the sample, thus increasing the probability for spontaneous emission of the embedded light sources. Secondly, spontaneously emitted radiation is efficiently channeled out of the sample along particular directions. This occurs when the lattice parameter of the photonic crystal is chosen such that the emission frequencies are in the range of enhanced $\bar{R}(\omega)$. A clear example of enhanced escape is apparent in Fig. 4.5 at $\theta_e = 0°$ near 18000 cm^{-1}. In the ultimate case of a photonic bandgap, it has even been predicted that the diffuse emission is extremely directional, see Ref. [17]. Thirdly, one can envision situations where *both* excitation and emission are enhanced: in Fig. 4.8(b) enhanced escape probability occurs both at $\omega a/2\pi c \sim 0.8$ and $\theta_e = 0°$ and at $\omega a/2\pi c \sim 0.7$ and $\theta_e = 50°$. Thus, by tuning the excitation to the former condition and the emission to the latter, the spontaneous emission yield is expected to be enhanced by at least a factor of 2. Further improvements should be feasible in photonic crystals with even larger $\bar{R}$.

4.5 Conclusions

We have presented experimental data on angular resolved emission from light sources embedded in efficient 3D photonic crystals. The experiments were compared in detail to a recently developed model of light transport in real and thick photonic crystals that are influenced by ubiquitous disorder. Our model is based on diffusion of light due to scattering (disorder) combined with angle- and frequency-dependent internal reflections (order). Good quantitative agreement between experiment and theory confirms that the details of the emission spectra are determined by the intricate interplay of order and disorder. Properties of the stopbands, such as their frequency range, magnitude, and angular dependence, are extracted from the experiment by analyzing the emission escape function. The *enhanced* escape probability for emission along directions outside the stopbands is explained by the angle-averaged internal-reflection coefficient $\bar{R}(\omega)$. The diffuse and angle-dependent nature of light escaping from the photonic crystals proves that the light comes

from emitters *inside* the crystals. By measuring the escape functions of the QD emission from the titania inverse opals, we have for the first time revealed clear stopbands in the QD emission spectra, confirming that the confined excitons experience optical confinement. The quantitative agreement between experiment and theory demonstrates that light propagation and spontaneous emission in real 3D photonic crystals is well understood.

References

[1] R. Sprik, B. A. van Tiggelen and A. Lagendijk, *Optical Emission in Periodic Dielectrics*, Europhys. Lett. **35**, 265 (1996).

[2] K. Busch and S. John, *Photonic Band Gap Formation in Certain Self-Organizing Systems*, Phys. Rev. E **58**, 3896 (1998).

[3] A. F. Koenderink, L. Bechger, H. P. Schriemer, A. Lagendijk and W. L. Vos, *Broadband Fivefold Reduction of Vacuum Fluctuations Probed by Dyes in Photonic Crystals*, Phys. Rev. Lett. **88**, 143903 (2002).

[4] S. Ogawa, M. Imada, S. Yoshimoto, M. Okato and S. Noda, *Control of Light Emission by 3D Photonic Crystals*, Science **305**, 227 (2004).

[5] P. Lodahl, A. F. van Driel, I. S. Nikolaev, A. Irman, K. Overgaag, D. Vanmaekelbergh and W. L. Vos, *Controlling the Dynamics of Spontaneous Emission from Quantum Dots by Photonic Crystals*, Nature **430**, 654 (2004).

[6] M. Fujita, S. Takahashi, Y. Tanaka, T. Asano and S. Noda, *Simultaneous Inhibition and Redistribution of Spontaneous Light Emission in Photonic Crystals*, Science **308**, 1296 (2005).

[7] V. N. Bogomolov, S. V. Gaponenko, I. N. Germanenko, A. M. Kapitonov, E. P. Petrov, N.V. Gaponenko, A.V. Prokofiev, A. N. Ponyavina, N. I. Silvanovich and S. M. Samoilovich, *Photonic Band Gap Phenomenon and Optical Properties of Artificial Opals*, Phys. Rev. E **55**, 7619 (1997).

[8] A. Blanco, C. López, R. Mayoral, H. Míguez, F. Meseguer, A. Mifsud and J. Herrero, *CdS Photoluminescence Inhibition by a Photonic Structure*, Appl. Phys. Lett. **73**, 1781 (1998).

[9] M. Megens, J.E.G.J. Wijnhoven, A. Lagendijk and W. L. Vos, *Light Sources inside Photonic Crystals*, J. Opt. Soc. Am. B **16**, 1403 (1999).

[10] Y. A. Vlasov, M. Deutsch and D. J. Norris, *Single-Domain Spectroscopy of Self-Assembled Photonic Crystals*, Appl. Phys. Lett. **76**, 1627 (2000).

[11] H. P. Schriemer, H. M. van Driel, A. F. Koenderink and W. L. Vos, *Modified Spontaneous Emission Spectra of Laser Dye in Inverse Opal Photonic Crystals*, Phys. Rev. A **63**, 011801(R) (2001).

[12] Y. Lin, J. Zhang, E. H. Sargent and E. Kumacheva, *Photonic Pseudo-Gap-Based Modification of Photoluminescence from CdS Nanocrystal Satellites around Polymer Microspheres in a Photonic Crystal*, Appl. Phys. Lett. **81**, 3134 (2002).

[13] A. F. Koenderink, A. Lagendijk and W. L. Vos, *Optical Extinction due to Intrinsic Structural Variations of Photonic Crystals*, Phys. Rev. B **72**, 153102 (2005).

[14] L. Bechger, P. Lodahl and W. L. Vos, *Directional Fluorescence Spectra of Laser Dye in Opal and Inverse Opal Photonic Crystals*, J. Phys. Chem. B **109**, 9980 (2005).

[15] A. F. Koenderink, P. M. Johnson, J. F. Galisteo-López and W. L. Vos, *Three-Dimensional Photonic Crystals as a Cage for Light*, C. R. Physique **3**, 65 (2002).

[16] J. F. Galisteo-López, E. Palacios-Lidón, E. Castillo-Martínez and C. López, *Optical Study of the Pseudogap in Thickness and Orientation Controlled Artificial Opals*, Phys. Rev. B **68**, 115109 (2003).

[17] A. F. Koenderink and W. L. Vos, *Light Exiting from Real Photonic Band Gap Crystals is Diffuse and Strongly Directional*, Phys. Rev. Lett. **91**, 213902 (2003); *Optical Properties of Real Photonic Crystals: Anomalous Diffuse Transmission*, J. Opt. Soc. Am. B **22**, 1075 (2005).

[18] J. R. Lakowicz, *Principles of Fluorescence Spectroscopy* (Second Edition), Kluwer, New-York, (1999).

[19] W.G.J.H.M. van Sark, P.L.T.M. Frederix, D. J. van den Heuvel, H. C. Gerritsen, A. A. Bol, J.N.J. van Lingen, C. D. de Mello Donegá and A. Meijerink, *Photooxcidation and Photobleaching of Single CdSe/ZnS Quantum Dots Probed by Room-Temperature Time-Resolved Spectroscopy*, J. Phys. Chem. B. **105**, 8281 (2001).

[20] A. F. Koenderink, M. Megens, G. van Soest, W. L. Vos and A. Lagendijk, *Enhanced Backscattering from Photonic Crystals*, Phys. Lett. A **268**, 104 (2000).

[21] A. Lagendijk, R. Vreeker and P. de Vries, *Influence of Internal Reflection on Diffusive Transport in Strongly Scattering Media*, Phys. Lett. **136A**, 81 (1989).

[22] J. X. Zhu, D. J. Pine and D. A. Weitz, *Internal Reflection of Diffusive Light in Random Media*, Phys. Rev. A **44**, 3948 (1991).

[23] D. J. Durian, *Influence of Boundary Reflection and Refraction on Diffusive Photon Transport*, Phys. Rev. E **50**, 857 (1994).

[24] I. S. Nikolaev, P. Lodahl and W. L. Vos, *Quantitative Analysis of Directional Spontaneous Emission Spectra from Light Sources in Photonic Crystals*, Phys. Rev. A **71**, 053813 (2005).

[25] The average refractive index of a photonic crystal is estimated as: $n_{\mathrm{av}} = \varphi\, n_m + (1 - \varphi)\, n_{\mathrm{air}}$, where φ is the volume fraction of the solid material, n_m and n_{air} are refractive indices of the solid material and air, respectively.

[26] F.J.P. Schuurmans, D. Vanmaekelbergh, J. van de Lagemaat and A. Lagendijk, *Strongly Photonic Macroporous Gallium Phosphide Networks*, Science **284**, 141 (1999).

[27] M. S. Thijssen, R. Sprik, J.E.G.J. Wijnhoven, M. Megens, T. Narayanan, A. Lagendijk and W. L. Vos, *Inhibited Light Propagation and Broad Band Reflection in Photonic Air-Sphere Crystals*, Phys. Rev. Lett. **83**, 2730 (1999).

[28] H. M. van Driel and W. L. Vos, *Multiple Bragg Wave Coupling in Photonic Band Gap Crystals*, Phys. Rev. B **62**, 9872 (2000).

[29] A. G. Galstyan, M. E. Raikh and Z. V. Vardeny, *Emission Spectrum of a Dipole in a Semi-Infinite Periodic Dielectric Structure: Effect of the Boundary*, Phys. Rev. B **62**, 1780 (2000).

CHAPTER 5

SPONTANEOUS EMISSION OF QUANTUM-DOT ENSEMBLES IN PHOTONIC CRYSTALS CONTROLLED BY LOCAL DENSITY OF STATES

We have measured spontaneous-emission decay rates from an ensemble of CdSe quantum dots in strongly interacting inverse-opal photonic crystals. We have observed considerable modifications of emission decay rates: both inhibition and enhancement are achieved by varying the crystal lattice parameter. The complex decay curves are successfully analyzed in a new way: with a continuous distribution of decay rates. The resulting most-frequent decay rate varies by a factor of 3, whereas the width of the distribution reveals a sixfold modification. The large modification of the distribution width with the lattice parameter is identified with variations of the radiative emission rates from quantum dots at various positions in the unit cell and with variously oriented transition dipoles. This interpretation qualitatively agrees with calculations of the projected local density of states. The mean emission rate varies by a factor of 8, in conformity with the change of the total emitted power. Measurements at different optical frequencies show that the variation of the decay rate with the lattice parameter is larger at higher emission frequencies of the quantum-dot spectrum.

5.1 Introduction

The radiative rate of spontaneous emission of elementary light sources (atoms, molecules or quantum dots) is proportional to the local radiative density of optical states (LDOS), to which the sources with certain orientations of the transition dipole moments couple, as discussed in Chapter 2. This projected LDOS counts the number of electromagnetic states at a given frequency, location and orientation of the transition dipole. Therefore, knowledge of the frequency and position dependence of the LDOS offer a tool to control spontaneous emission from molecules [1], atoms [2, 3], and quantum dots [4–8]. It has

been predicted that photonic crystals possessing a photonic bandgap (PBG) can radically change spontaneous emission [9]. Later, it was theoretically shown that a much weaker requirement than a PBG has to be met to suppress spontaneous emission: sources should be placed at judicious locations in the crystal unit cell where the LDOS vanishes [10]. For emitters with fixed or slowly varying dipole orientations, for instance for dye molecules on substrates [11, 12], the density of modes projected on the dipole orientations should be suppressed. Since the frequency-integrated number of states is conserved, one expects the LDOS to be strongly increased at some frequencies outside such a pseudogap [10, 13–16]. Hence, photonic crystals may completely control the emission rates between absolute inhibition and strong enhancement even in the absence of a PBG.

Most of the theoretical papers on photonic crystals study spontaneous emission from single emitters. However, it is often more practical to measure emission from many light sources. Moreover, control over spontaneous emission from a large number of sources is important for applications such as light-emitting diodes and solar cells. One could expect that the radiation dynamics of an ensemble of emitters, distributed in different locations in the unit cell of a photonic crystal, are not characterized by a single decay rate, but rather by a distribution of decay rates. Due to such multi-exponential decays, analysis of the measurements on ensembles of emitters in photonic crystals becomes more difficult comparing to cases with single emitters.

Inhibition of the radiative decay rate versus frequency has been observed in continuous-wave experiments on sources with a low quantum efficiency [17, 18]. However, time-resolved control of the spontaneous-emission lifetimes is only possible with much more efficient sources. Indeed, both enhanced and inhibited decay rates have been observed from highly-efficient emitters in 3D inverse opals [5] and also in 2D slab structures [6–8, 19]. To our knowledge, all experimental work to date concerns the frequency dependence of the LDOS and of the emission rate in photonic crystals, but the position and orientation dependencies remain open issues. In this chapter we present a study of the position and orientation dependencies of the LDOS: we distributed an ensemble of identical light sources over a well-defined set of positions in the unit cell and measured the time-resolved emission. We propose a novel method to interpret the emission data with a continuous distribution of emission rates. The width of the distribution is proportional to the distribution of the LDOS over all positions $\mathbf{r}_i$ (see Fig. 5.1) and dipole orientations sampled by sources with fixed emission frequency ω. The mean emission rate reveals a striking variation of a factor of 8 with varying crystal lattice spacing. These obser-

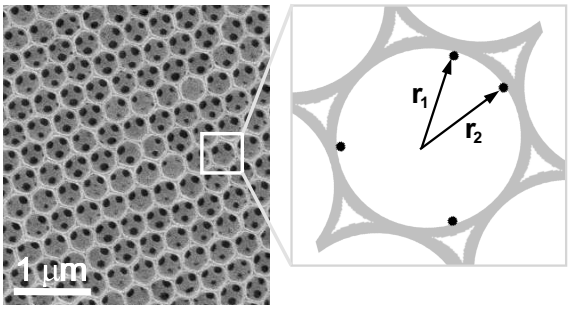

FIGURE 5.1: (*Left*) Electron-microscope image of the (111) surface of an inverse opal consisting of air spheres in TiO_2 with lattice parameter a = 455 nm. (*Right*) Schematic representation of quantum dots (black spots) inside an air sphere (white) on the internal titania-air surfaces at symmetry-inequivalent positions $\mathbf{r}_i$.

vations are in qualitative agreement with intricate calculations of the LDOS. This is the first experimental evidence for position- and orientation-dependent emission rates in 3D photonic crystals.

5.2 Experimental details

5.2.1 Samples

We have studied time-resolved spontaneous emission in titania inverse opals introduced in Chapter 3 and similar to the samples studied in the angle-resolved experiment in Chapter 4. We investigated emission in 18 different samples with lattice parameters ranging from a = 255 to 760 nm.[(1)] As light sources we used CdSe-ZnSe core-shell colloidal quantum dots (QDs) because of their high fluorescence quantum efficiency and narrow homogeneous spectral width. The QD ensemble dispersed in chloroform has a quantum efficiency of more than 50% and a size dispersion of 5 % around the average diameter of 4.5 nm, as discussed in Chapter 3. The average diameter determines the center frequency of the emission spectrum at $\omega \approx 16400$ cm^{-1} ($\lambda \approx 610$ nm). The spectral widths of the QD ensemble is about $\Delta\omega/\omega \approx 0.075$ (see, *e.g.*, Fig. 3.8b). The relative homogeneous linewidth of a single QD at room temperature $\Delta\omega/\omega \approx 0.025$ is due to the electron-phonon

[(1)] The values of the lattice parameters have random deviations of about 3 % due to size dispersion of spheres in opals and the shrinkage of the inverse opals during the preparation [20].

interactions, as calculated in Ref. [21] and measured in Ref. [22]. The rest of the emission linewidth is inhomogeneously broadened by the size dispersion in the QD ensemble. The process of the liquid infiltration of the photonic crystals with the QDs is described in Chapter 4. After the infiltration, the QDs precipitate on the internal surfaces of the air spheres inside the inverse opals, with an estimated low density of four QDs per air sphere, as sketched in Figure 5.1. During the optical experiments, the inverse opals were held in a sealed chamber under a 1.7 mbar nitrogen atmosphere, in order to minimize the probability of the photooxidation of the QDs.

5.2.2 Time-resolved experiment

The quantum dots inside the photonic crystals were excited at λ = 447 nm with a pulsed diode laser (Picoquant, LDH-440) with a pulse duration of 90 ps and a repetition rate of 10 MHz. The energy on the sample was below 20 nJ/pulse to avoid double excitations of the QDs. The excitation beam was focused by a microscope objective (N.A. = 0.05, focal length of 73 mm) to a spot diameter of $\sim$ 30 μm at an incident angle of $\sim$ 25° relative to the surface normal, which is parallel to the 111 reciprocal lattice vector. The position of the excitation spot on the sample was monitored with a microscope. To detect the QD emission, we used the same set-up that is described in Chapter 4. The emitted light was collected within a cone of 15° full width and imaged on the slit of the prism spectrometer with spectral resolution better than 85 cm^{-1} (3 nm).

To measure the arrival time of the photons emitted after the laser pulse, we use the time-correlated single-photon counting technique [23, 24]. The signal from the photomultiplier tube (average count rate $\sim$ 10 kHz) is sent to a time-to-amplitude converter (Tennelec, TC 864) that produces a 'start' signal to indicate that a photon has been detected and thereby to initiate a voltage ramp. The synchronization signal from the pump laser is used as a 'stop' signal, and the voltage difference that builds up between 'start' and 'stop' events is a measure of the emission time of the QD excited state after excitation. A multichannel analyzer converted the voltage to a time channel using an analog-to-digital converter. The decay curves are histograms of the arrival time of a single photon emitted after the laser pulse, obtained over many excitation-emission cycles with a time resolution better than 100 ps. The slope of the decay curves yields a fluorescence decay rate $\gamma = \gamma_{rad} + \gamma_{nrad}$, which is the sum of the spontaneous-emission decay rate γ_{rad} and the non-radiative rate γ_{nrad} that depopulate the excited states of the QDs.

5.3 Experimental results

The CdSe-ZnSe core-shell quantum dots are new and exciting type of light sources whose emission properties can be tuned to satisfy needs of experimentalists. However, emission properties of these light sources are sensitive to oxygen: as discussed earlier, photoinduced reaction of the QDs with oxygen leads to the “blue shift" of the emission frequency and to the quenching of fluorescence. In our emission experiments on QDs in the low-pressure nitrogen atmosphere, we did not observe any significant effects of photooxidation such as bleaching of the QDs and the blue shift of the emission spectrum. In contrast, in some samples, the emission intensity was found to *increase* during the experiment, while the excitation intensity was constant. An example of this effect is shown in Figure 5.2a (squares). This process, called photoenhancement or photobrightening of the QD fluorescence, is not yet understood [25]. It was observed that the photobrightening is reversible and attributed to chemical modifications of the QD surfaces induced by non-resonant excitation, which improve the fluorescence efficiency. We have observed that the photobrightening affects the emission dynamics of the QDs: a strong increase of the emission intensity correlates with a considerable decrease of the ensemble-averaged decay rate of the QDs in an inverse opal as shown in Figure 5.2b. Only a few samples from the whole

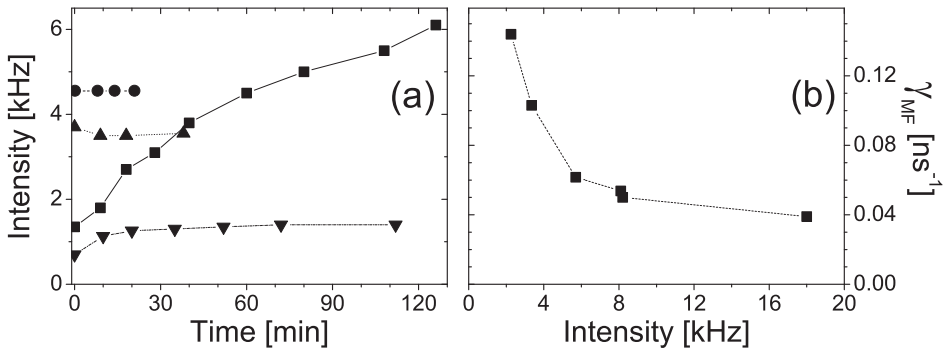

FIGURE 5.2: (a) Intensity I at the QD spectral maximum versus time after the beginning of the emission experiment. Some samples reveal noticeable photoenhancement as an inverse opal with lattice parameter a = 890 nm (squares). In contrast, the intensity from many other samples is stable, as in inverse opals with a = 320 nm (circles, I/2), a = 755 nm (triangles, I/10) and a = 425 nm (inverted triangles). (b) Most-frequent decay rate γ_{MF} (see Eq. 5.2) for the sample with a = 890 nm as a function of the emission intensity during the photoenhancement process.

series revealed this effect, and we observed no correlation between the lattice parameter of the inverse opals and the occurrence of the photobrightening. We only found that the probability of this effect increases if the samples infiltrated with the QDs are kept for a long time, even in the nitrogen atmosphere: there were more samples with photobrightening among those, which were measured after 5 to 7 days after the infiltration, than those, measured within 3 days after the infiltration. In our experiments, we want to compare the decay rates of the QDs in photonic crystals with different lattice parameters. This comparison is impeded if the decay rates change during the experiment. Therefore, we disregarded the samples, which showed the photobrightening, and will further present data on the samples, in which the emission intensity stabilized within several minutes [see, *e.g.*, Figure 5.2a (circles, triangles and inverted triangles)].

In Fig. 5.3 we show time-resolved spontaneous emission from the QDs in inverse opals with three different lattice parameters a, *i.e.*, at different reduced frequencies a/λ. The data were collected at $\lambda = 615$ nm within a narrow range $\Delta\lambda = 3$ nm, to select the same population of QDs with identical emission properties on each sample. For inverse opals with $a = 255$ nm, $\lambda = 615$ nm is in the low-frequency limit, where the frequency dependence of the LDOS is known to be proportional to ω^2 [10, 15]. We see that spontaneous emission in a sample with $a = 425$ nm is inhibited compared to the reference. Conversely, in a sample with $a = 540$ nm, the decay rate is enhanced. It is important to notice that in contrast to atoms in vacuum, emission from sources embedded in solid-state systems as photonic crystals can be distorted by the fluorescence from the the backbone material. In our experiment, the fluorescence of the titania backbone distorts the signal at short times [see Fig. 5.3a (curve 4)]. We have carefully removed the TiO_2 signal from the measured decay curves since we know its spectrum and decay curve from measurements on an undoped inverse opal; the backbone has a countrate less than 12 % of the QD signal. We exclude the possibility that QDs at the sample surface contribute any measurable signal since: a) QDs on the surface were rinsed off after infiltration, b) the excitation intensity is maximum inside the samples at a distance of several Bragg attenuation lengths from the surface due to light diffusion, and c) and analysis of the angle-resolved measurements described in Chapter 4 reveals an excellent agreement with theory for sources emitting in the bulk of photonic crystals. We have also verified that the excitation beam is not Bragg diffracted. Therefore, Fig. 5.3 demonstrates time-resolved emission from an ensemble of QDs controlled by photonic crystals, over a much larger time range than in previous experiments [5–8, 19].

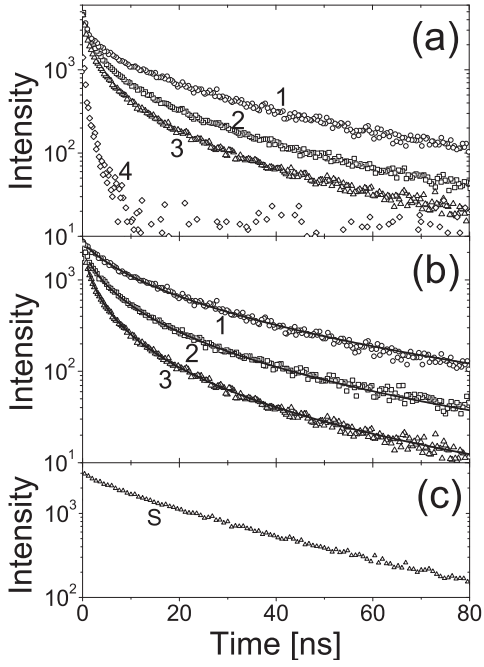

FIGURE 5.3: (a) Fluorescence decay curves recorded at ω = 16260 cm^{-1} (λ = 615 nm) and T = 295 K from QDs in inverse opals with lattice parameters: a = 425 nm (1), a = 255 nm (2) and a = 540 nm (3). Curves 2 and 3 are overlapped at 0 ns with curve 1. Curve 4 represents a decay from the backbone emission at the same frequency. This decay curve contains 1/15 of the total counts of curve 1. (b) Curves 1, 2 and 3 represent the same measurements as in (a) with the backbone emission subtracted. Solid lines are fits of the log-normal distribution of decay rates to the data. The goodness of fit χ^2_{red} varies from 1.1 to 1.4, close to the ideal value 1. (c) Curve S shows a nearly single-exponential decay from the QDs in a homogeneous medium (in chloroform).

An important feature in Figure 5.3b is that the decay curves from the QDs in the inverse opals are multi-exponential, which can be due to four possible reasons:

i. The QDs experience different LDOS, since they are distributed over symmetry-inequivalent positions and random dipole orientations in the unit cell (see Fig. 5.1).

ii. It has been predicted that single QDs reveal non-exponential decay due to van Hove singularities in the LDOS [26]; however, this requires single-dot experiments, which is not the case here.

iii. It has recently been identified that colloidal QDs are not true two-level systems [27]. Nevertheless, it was observed that the emission decay of the QDs was closely single-exponential, as confirmed in Fig. 5.3c.

iv. It was suggested that temporal fluctuations of the environment surrounding the QDs induce a distribution of non-radiative decay channels [28, 29]. In our experiment, the non-radiative rates hardly vary from sample to sample because QDs from the same batch are used, and the photonic crystals are chemically identical.[(2)] We indeed observe only minute differences of decay-curve slopes among the samples with the same lattice parameters.

Therefore, we attribute the observed variations of the multi-exponential decay curves to a distribution of radiative decay rates as a result of a spatial and orientational variation of the LDOS.

5.4 Modeling of multi-exponential decay curves

To interpret complex, non-single-exponential decay curves, we propose a new line of attack by modeling the decay curves with a continuous distribution of decay rates:

$$I(t) = I_0 \int_{\gamma=0}^{\infty} \phi(\gamma) e^{-\gamma t} d\gamma, \tag{5.1}$$

where $\phi(\gamma)$ represents a distribution of decay rates γ with dimension of time [30]. We use the log-normal distribution function:

$$\phi(\gamma) = A \ \exp\!\left(-\frac{\ln^2(\gamma/\gamma_{\mathrm{MF}})}{w^2}\right), \tag{5.2}$$

where γ_{MF} is the most-frequent decay rate corresponding to the maximum of $\phi(\gamma)$, w is a dimensionless width parameter that determines the distribution width at $1/e$:

$$\Delta\gamma = 2\gamma_{\mathrm{MF}} \sinh w. \tag{5.3}$$

A in Eq. 5.2 is the normalization constant, so that $\int_{\gamma=0}^{\infty} \phi(\gamma) d\gamma = 1$. The distribution function $\phi(\gamma)$ enables us to model intrinsically multi-exponential decay curves, which is essential when treating an ensemble of emitters. The important features of our analysis

[(2)] Because the QDs in chloroform have different chemical environment from the inverse opals, we do not compare emission from the QDs in chloroform (Fig. 5.3c) with emission from the QDs in the inverse opals.

are that the distribution containing the physical information is readily available, that it is specified in terms of only two free parameters, γ_{MF} and $\Delta\gamma$, and that the *log*-form of the distribution function excludes unphysical negative decay rates. Another multi-exponential model is the stretched exponential that has been employed to single QDs [28, 29]. The stretched exponential model, however, does not match our data, which again confirms that the variations we observe are due to LDOS effects in photonic crystals and not to complex emission properties of the QDs. In Fig. 5.3(b) it is seen that the log-normal distribution model (solid curves) provides an excellent description of the experimental data.

5.5 Photonic-crystal effects on emission decay rates

5.5.1 Decay rates vs. crystal lattice parameter

We will first consider the resulting decay rates of QDs measured at fixed emission frequency in the inverse opals with different lattice parameters. In this way, we can study radiative-decay dynamics from QDs having identical internal properties as a function of the reduced frequency, which is an important parameter of the LDOS. Fig. 5.4 shows the resulting decay-rate distributions for three lattice parameters. It is remarkable that the log-normal provides an excellent explanation for all reduced frequencies a/λ studied, which

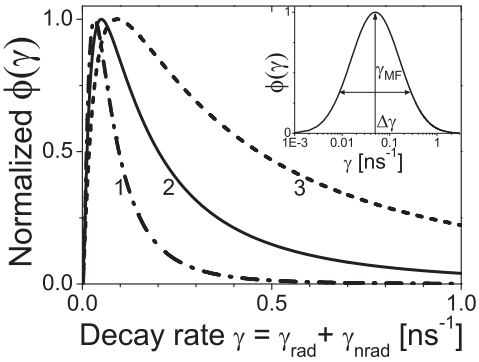

FIGURE 5.4: Decay distributions $\phi(\gamma)$ for the inverse opals with lattice parameters a = 425 nm (1), a = 255 nm (2) and a = 540 nm (3), corresponding to the data shown in Fig. 5.3. Inset shows $\phi(\gamma)$ for a = 255 nm in the semi-log scale. Clear modifications of $\Delta\gamma$ and γ_{MF} with varying lattice parameter of the inverse opals are seen.

will be seen below to agree with calculations. Compared to the low-frequency reference (a = 255 nm), the maximum of the distribution $\phi(\gamma)$ is shifted to lower decay rates for the crystal with a = 425 nm, and to higher rates for the crystal with a = 540 nm. These shifts are a clear demonstration of a photonic-crystal effect of the inverse opals on the ensemble of embedded emitters. In Fig. 5.4, we see a dramatic change of the width $\Delta\gamma$ of the distribution. The large width of each distribution is identified with the variation of the radiative emission rates due to orientational and positional $\mathbf{r}_i$ dependencies of the LDOS at each lattice parameter. Consequently, the decay rates of individual QDs are much more strongly modified by the photonic crystal than the most-frequent rate γ_{MF} of the ensemble.

In Fig. 5.5(a,b) we have plotted the resulting values for $\Delta\gamma$ and γ_{MF} versus reduced frequency. Let us briefly consider γ_{MF}: because the non-radiative part of the total decay rates does not change with the lattice parameter, the change of γ_{MF} - $\gamma_{\mathrm{MF}}^{ref}$ is purely radiative and related to an averaged photonic-crystal LDOS. We compare the experimental data to the calculated LDOS (dashed curve) that is averaged over several symmetry-inequivalent locations on the internal TiO_2-air interfaces and over random dipole orientations. The measured variation of γ_{MF} is in good agreement with the DOS. Both inhibited and enhanced decay rates are observed, and the experimental variation in γ_{MF} amounts to a factor of 3. Now, if we consider the change of the distribution width $\Delta\gamma$, we see that the data show a striking variation of a factor of 6, which is much larger than the change of γ_{MF}. Already in the low-frequency limit, $a/\lambda = 0.4$, there is a spatial variation of the radiative rate ($\Delta\gamma \geq 0$), because the QDs distributed over inequivalent positions in the unit cell couple to different electric fields [32]. At the frequencies of the L-gap, $a/\lambda \approx 0.7$, the radiative rate γ_{rad} is inhibited in most places in the unit cell that are occupied by the QDs, as confirmed by a low continuous-wave (cw) countrate of only $\approx$ 2.5 kHz. Therefore, the observed narrow width $\Delta\gamma = 0.1$ ns^{-1} is a measure of the distribution width of non-radiative rates. In contrast, at $a/\lambda = 0.88$, $\Delta\gamma$ is strongly increased; here the cw countrate is $\approx$ 56 kHz at similar experimental conditions, in agreement with an enhanced γ_{rad}. We therefore conclude that the large widths $\Delta\gamma$ are determined by a broad distribution of radiative emission rates $\Delta\gamma_{rad}$ that are proportional to a broad distribution of the projected LDOS at fixed frequency.

We have performed intensive computations to find the LDOS at various positions in the unit cell of the inverse opals. Details on the calculations of the LDOS are presented in Chapter 6. The LDOS shown in Figure 5.5c was calculated at two representative positions in the unit cell at the TiO_2-air interface, for dipole orientations parallel and perpendicular

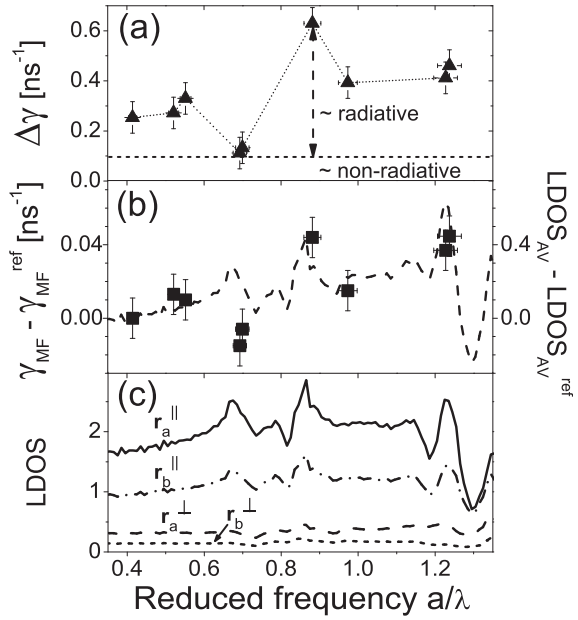

FIGURE 5.5: (a) Width of the decay-rate distribution $\Delta\gamma$ vs. lattice parameter at fixed emission wavelength (triangles, dashed curve is guide to the eye). (b) Difference between γ_{MF} measured on a photonic sample and $\gamma_{\mathrm{MF}}^{ref}$ = 0.05 ns^{-1} of the low-frequency reference (squares). Error bars are estimated from the largest difference between data on samples with similar a. Dashed curve represents the difference between the averaged LDOS in the inverse opals [31] and the averaged LDOS for the low-frequency reference (LDOS$^{\mathrm{ref}}$ $\approx$ 0.7 at a/$\lambda \approx$ 0.41). The averaging was performed over all dipole orientations and over five points on the internal TiO_2-air interfaces: at points **a**, **b**, **c**, **d** (shown in Fig. 6.5) and **r**=(0.23,0.23,0.14). (c) LDOS at two positions on the internal TiO_2-air surfaces projected on dipole orientations parallel ($\parallel$) or normal ($\perp$) to the internal surface: at $\mathbf{r}_{\mathrm{a}} = \frac{1}{4\sqrt{3}}(1,1,2)$ and at $\mathbf{r}_{\mathrm{b}} = \frac{1}{2\sqrt{6}}(1,1,1)$.

to the TiO_2-air interface. The resulting LDOS in Fig. 5.5c reveals a strong dependency on the position in the crystal unit cell (compare curves 1 and 2) and on the dipole orientation (compare curves 1 and 3). It is remarkable that in the relevant a/λ range the frequency dependence of the LDOS is the same at both positions **r** and both dipole orientations, and even at all other studied positions and orientations (see also Fig. 6.6). This result agrees with the observation that all measured decay curves are successfully modeled with the same shape of the decay-rate distribution. Because the LDOS for dipoles perpendicular to the interface is inhibited and nearly constant at all reduced frequencies whereas the

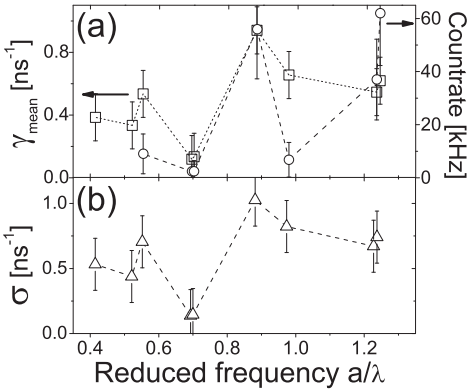

FIGURE 5.6: (a) Mean decay rate γ_{mean} of the decay-rate distribution $\phi(\gamma)$ (empty squares) and *cw* countrate at the maximum of the QD spectrum (empty circles) vs. lattice parameter. (b) Standard deviation σ for the distribution $\phi(\gamma)$. Dashed lines are guides to the eye.

LDOS for parallel dipoles has strong variations, we propose that the width of the LDOS distribution has a similar frequency dependence as the LDOS itself. This notion agrees with the observation that $\Delta\gamma$ tracks the behavior of γ_{MF}. A quantitative comparison of our data to the calculated LDOS is compounded, since, as discussed above, knowledge on the relation between γ_{rad} and γ is required to infer the the radiative decay-rate distribution from the γ_{rad}-weighted distribution $\phi(\gamma)$ [30]. Qualitatively, the calculated LDOS reflects the main features of our experiments.

From the modeled emission decay curves, we have also calculated the mean decay rate γ_{mean} and the standard deviation σ corresponding to the log-normal shape of the decay-rate distribution $\phi(\gamma)$.[(3)] The resulting dependencies of γ_{mean} and σ on the reduced frequency, shown in Figure 5.6, reveal a similar trend to γ_{MF} and $\Delta\gamma$. The modifications of these parameters are, however, noticeably larger: the changes of both γ_{mean} and σ amount to a factor of 8. The modification of the mean decay rate corresponds to the observed large variation of the *cw* countrate [see Figure 5.6a (circles)]: for emitters with the quantum efficiency lower than 100 %, an enhancement of the radiative rate leads to an increased quantum efficiency and, consequently, to an increase of the total emitted power. A suppression of the radiative rates conversely leads to a decrease of the emitted power.

[(3)] In the calculation of γ_{mean} and σ, the integration performed from γ = 0.0125 to 5 ns^{-1} is consistent with the time resolution and the range of the decay histograms.

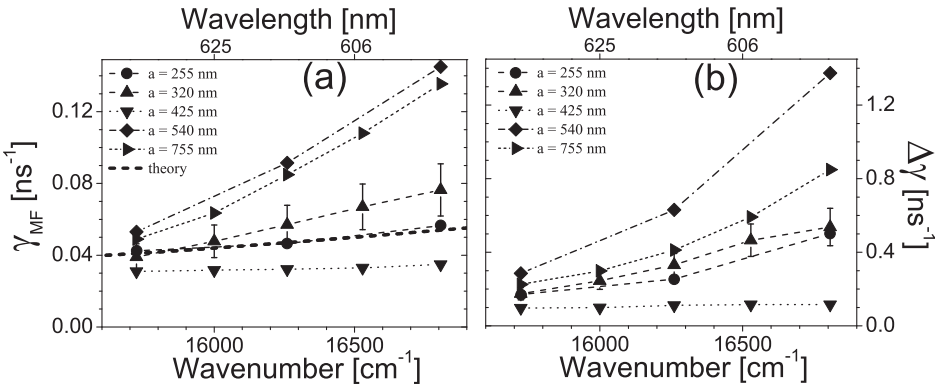

FIGURE 5.7: Most-frequent decay rate γ_{MF} and distribution width $\Delta\gamma$ determined using the log-normal distribution (Eq. 5.2) for QD emission in inverse opals with lattice parameters a = 255, 320, 425, 540 and 755 nm. The lines connecting the data points are guides to the eye. The error bars shown for a = 320 nm are typical for all samples and estimated from the largest difference between data on samples with similar a. The dashed curve in (a) represents calculated decay rates of the QDs in a homogeneous medium: calculations made in Ref. [27] were overlapped with γ_{MF} for sample with a = 255 nm by adding a constant non-radiative part, which yields then the ensemble-average quantum efficiency of $\sim$ 30 %.

5.5.2 Frequency dependence of emission decay rates

We will now consider the frequency dependence of the most-frequent decay rate γ_{MF} and the distribution width $\Delta\gamma$. Figure 5.7 shows the data for γ_{MF} (a) and $\Delta\gamma$ (b) for five inverse opals with different lattice parameters. For each sample we observe an increase of γ_{MF} and $\Delta\gamma$ with increasing emission frequency. The frequency behavior of γ_{MF} in the low-frequency reference sample (a = 255 nm, circles) is in agreement with the supralinear increase of the radiative decay rate of CdSe QDs that was observed in a homogeneous medium (dashed curve) [27]. Such behavior is the result of the frequency dependence of an ideal two-level exciton with a thermal occupation of dark excitonic states. This good agreement is also an experimental argument to exclude the possibility of resonant energy-transfer processes between the QDs.[(4)] As previously discussed, the distribution of the non-radiative rates γ_{nrad} in the QD ensemble is the same for all our inverse opals. We also exclude any significant variations of γ_{nrad} with changing optical frequency within the

[(4)] In Chapter 4, based on the low density of QDs of at most four dots per air sphere, we concluded that reabsorption and energy-transfer processes are negligible.

narrow frequency range of the QD emission. While the non-radiative relaxation occurs mostly via acceptor levels at the surface of a QD [28, 33], there is only a 10 % variation of the surface area among QDs in the ensemble with a 5 % size dispersion. Therefore, the observed modifications of γ_{MF} and $\Delta\gamma$ in the inverse opals with different lattice parameters are due to changes in the radiative decay rate γ_{rad}.

In Fig. 5.7 one can see that the frequency dependence of the QD decay rates is different in inverse opals with different lattice parameters. In the inverse opal with a = 425 nm, both γ_{MF} and $\Delta\gamma$ are nearly constant. In contrast, for example, γ_{MF} and $\Delta\gamma$ strongly increase with frequency in the inverse opal with a = 540 nm. Such frequency behavior, dependent on the lattice parameter, means that the variation of the decay rate with the lattice parameter is larger at higher emission frequencies of the spectrum of the QD ensemble. A possible explanation of this effect could be the above-mentioned supralinear increase of the radiative decay rate in the QDs. Indeed, if the transition dipole moment in the CdSe QDs is proportional to ω^{-1}, as shown in Ref. [27], then using Equation 2.32 we can relate the radiative decay rate γ_{rad} to the LDOS $N(\omega)$ at a specific emission frequency ω as:

$$\gamma_{rad} \propto \omega^{-2}\omega N(\omega) \propto \omega^{-1}\alpha(a)\omega^2 = \alpha(a)\omega, \tag{5.4}$$

where we rewrite $N(\omega)$ as the lattice-parameter dependent LDOS modulation $\alpha(a)$ multiplied by the parabolic absolute-frequency dependence ω^2. In Eq. 5.4, we see that the effect of photonic crystal on the decay rates of the QDs is enhanced at higher emission frequencies. However, the small frequency change within the narrow spectrum of the QD ensemble can only give a 7 % increase of the decay-rate modification and does not explain the large ($\sim$ 360 %) increase of the relative variation with the lattice parameter. Another explanation of the frequency-dependent effect of the photonic crystal can be the fact that the modeling of the emission decay curves results in decay-rate distributions weighted by the radiative rate γ_{rad} [30]. For emitters with the quantum efficiency below 100 % (the quantum efficiency of the studied QDs is $\sim$ 50 %), any variation of γ_{rad} changes the quantum efficiency. Consequently, in the time-resolved emission experiment, QDs with higher γ_{rad} emit more photons, and hence, the intensity decay from such QDs has a higher probability to be detected than the decay from QDs with low γ_{rad}. This means that a certain increase of γ_{rad} leads to an even larger shift of the decay-rate distribution $\phi(\gamma)$.

To the best of our knowledge, no one has yet studied absolute-frequency dependence of spontaneous-emission rates of QDs, as opposed to the reduced frequency. For CdSe

QDs in homogeneous media, the first study of the dependence of decay rates on optical frequencies was reported in Ref. [27]. To understand the frequency dependent decay rates of QD ensembles in photonic crystals, we need to know how the radiative rate γ_{rad} is distributed. To infer the genuine decay-rate distributions of a QDs ensemble, detailed knowledge of the relation between the total decay rates γ and the corresponding radiative rates γ_{rad} is required. At present, this is a Herculean challenge due to fluctuations of both non-radiative [28, 29] and radiative decay rates in the QD ensemble in photonic crystals.

5.6 Conclusions

We have studied dynamics of spontaneous emission from quantum-dot ensembles in inverse-opal photonic crystals. The measured modifications of decay rates are qualitatively explained by newly calculated projected LDOS in the inverse opals. Our results demonstrate that large inhibitions and enhancements of spontaneous emission can be achieved with properly positioned and oriented efficient dipolar light sources inside 3D photonic crystals, at room temperatures and in large volumes limited only by the crystal size. For the complementary case of a single quantum dot with a certain dipole orientation in a 2D slab, recent results obtained experimentally [6] and theoretically [34] are in accordance with our observations. We have also studied the decay rates as functions of optical frequency within the QD emission spectrum. We observe that the variation of the decay rate with the lattice parameter is larger at higher emission frequencies of the QD spectrum. Understanding of this effect as well as a quantitative comparison of our data to the calculated LDOS require detailed knowledge on the relation between γ_{rad} and γ, *i.e.*, the knowledge of γ_{nrad} in the QD ensemble.

References

[1] K. H. Drexhage, *Influence of a Dielectric Interface on Fluorescence Decay Time*, J. Lumin. **1**, 693 (1970).

[2] D. Kleppner, *Inhibited Spontaneous Emission*, Phys. Rev. Lett. **47**, 233 (1981).

[3] P. Goy, J. M. Raimond, M. Gross and S. Haroche, *Observation of Cavity-Enhanced Single-Atom Spontaneous Emission*, Phys. Rev. Lett. **50**, 1903 (1983).

[4] J. M. Gérard, B. Sermage, B. Gayral, B. Legrand, E. Costard and V. Thierry-Mieg, *Enhanced Spontaneous Emission by Quantum Boxes in a Monolithic Optical Microcavity*, Phys. Rev. Lett. **81**, 1110 (1998).

[5] P. Lodahl, A. F. van Driel, I. S. Nikolaev, A. Irman, K. Overgaag, D. Vanmaekelbergh and W. L. Vos, *Controlling the Dynamics of Spontaneous Emission from Quantum Dots by Photonic Crystals*, Nature **430**, 654 (2004).

[6] A. Badolato, K. Hennessy, M. Atature, J. Dreiser, E. Hu, P. M. Petroff and A. Imamoglu, *Deterministic Coupling of Single Quantum Dots to Single Nanocavity Modes*, Science **308**, 1158 (2005).

[7] A. Kress, F. Hofbauer, N. Reinelt, M. Kaniber, H. J. Krenner, R. Meyer, G. Böhm and J. J. Finley, *Manipulation of the Spontaneous Emission Dynamics of Quantum Dots in Two-Dimensional Photonic Crystals*, Phys. Rev. B **71**, 241304 (2005).

[8] D. Englund, D. Fattal, E. Waks, G. Solomon, B. Zhang, T. Nakaoka, Y. Arakawa, Y. Yamamoto and J. Vučković, *Controlling the Spontaneous Emission Rate of Single Quantum Dots in a Two-Dimensional Photonic Crystal*, Phys. Rev. Lett. **95**, 013904 (2005).

[9] E. Yablonovitch, *Inhibited Spontaneous Emission in Solid-State Physics and Electronics*, Phys. Rev. Lett. **58**, 2059 (1987).

[10] R. Sprik, B. A. van Tiggelen and A. Lagendijk, *Optical Emission in Periodic Dielectrics*, Europhys. Lett. **35**, 265 (1996).

[11] R. Vallée, N. Tomczak, H. Gersen, E.M.H.P. van Dijk, M. F. García Parajó, G. J. Vancso and N. F. van Hulst, *On the Role of Electromagnetic Boundary Conditions in Single Molecule Fluorescence Lifetime Studies of Dyes Embedded in Thin Films*, Chem. Phys. Lett. **348**, 161 (2001).

[12] M. Kreiter, M. Prummer, B. Hecht and U. P. Wild, *Orientation Dependence of Fluorescence Lifetimes near an Interface*, J. Chem. Phys. 117, 9430 (2002).

[13] T. Suzuki and P. K. L. Yu, *Emission Power of an Electric-Dipole in the Photonic Band-Structure of the Fcc Lattice*, J. Opt. Soc. Am. B **12**, 570 (1995).

[14] S. Barnett and R. Loudon, *Sum Rule for Modified Spontaneous Emission Rates*, Phys. Rev. Lett. **77**, 2444 (1996).

[15] K. Busch and S. John, *Photonic Band Gap Formation in Certain Self-Organizing Systems*, Phys. Rev. E **58**, 3896 (1998).

[16] R. Wang, X.-H. Wang, B.-Y. Gu and G.-Z. Yang, *Local Density of States in Three-Dimensional Photonic Crystals: Calculation and Enhancement Effects*, Phys. Rev. B **67**, 155114 (2003).

[17] A. F. Koenderink, L. Bechger, H. P. Schriemer, A. Lagendijk and W. L. Vos, *Broadband Fivefold Reduction of Vacuum Fluctuations Probed by Dyes in Photonic Crystals*, Phys. Rev. Lett. **88**, 143903 (2002).

[18] S. Ogawa, M. Imada, S. Yoshimoto, M. Okato and S. Noda, *Control of Light Emission by 3D Photonic Crystals*, Science **305**, 227 (2004).

[19] M. Fujita, S. Takahashi, Y. Tanaka, T. Asano and S. Noda, *Simultaneous Inhibition and Redistribution of Spontaneous Light Emission in Photonic Crystals*, Science **308**, 1296 (2005).

[20] J.E.G.J. Wijnhoven, L. Bechger and W. L. Vos, *Fabrication and Characterization of Large Macroporous Photonic Crystals in Titania*, Chem. Mater. **13**, 4486 (2001).

[21] X.-Q. Li and Y. Arakawa, *Optical Linewidths in an Individual Quantum Dot*, Phys. Rev. B **60**, 1915 (1999).

[22] W.G.J.H.M. van Sark, P.L.T.M. Frederix, D. J. van den Heuvel, H. C. Gerritsen, A. A. Bol, J.N.J. van Lingen, C. D. de Mello Donegá and A. Meijerink, *Photooxcidation and Photobleaching of Single CdSe/ZnS Quantum Dots Probed by Room-Temperature Time-Resolved Spectroscopy*, J. Phys. Chem. B. **105**, 8281 (2001).

[23] L. M. Bollinger and G. E. Thomas, *Measurement of the Time Dependence of Scintillation Intensity by a Delayed-Coincidence Method*, Rev. Sci. Instrum. **32**, 1044 (1961).

[24] J. R. Lakowicz, *Principles of Fluorescence Spectroscopy* (Second Edition), Kluwer, New-York, (1999).

[25] M. Jones, J. Nedeljkovic, R. J. Ellingson, A. J. Nozik and G. Rumbles, *Photoenhancement of Luminescence in Colloidal CdSe Quantum Dot Solutions*, J. Phys. Chem. B **107**, 11346 (2003).

[26] N. Vats, S. John and K. Busch, *Theory of Fluorescence in Photonic Crystals*, Phys. Rev. A **65**, 043808 (2002).

[27] A. F. van Driel, G. Allan, C. Delerue, P. Lodahl, W. L. Vos and D. Vanmaekelbergh, *Frequency-Dependent Spontaneous Emission Rate from CdSe and CdTe Nanocrystals: Influence of Dark States*, Phys. Rev. Lett. **95**, 236804 (2005).

[28] G. Schlegel, J. Bohnenberger, I. Potapova and A. Mews, *Fluorescence Decay Time of Single Semiconductor Nanocrystals*, Phys. Rev. Lett. **88**, 137401 (2002).

[29] B. R. Fisher, H.-J. Eisler, N. E. Stott and M. G. Bawendi, *Emission Intensity Dependence and Single-Exponential Behavior in Single Colloidal Quantum Dot Fluorescence Lifetimes*, J. Phys. Chem. B **108**, 143 (2004).

[30] The fluorescence intensity *I(t)* is determined by how fast the concentration of excited emitters decreases, and is proportional to the time-derivative of the concentration. As a result, $\phi(\gamma)$ describes the distribution of the concentration of emitters with a certain decay rate γ, weighted by the corresponding radiative rate γ_{rad}. For more details see Appendix B or e-print physics/0607043.

[31] The LDOS in the inverse opals is divided by the LDOS in a homogeneous medium with the same average refractive index (n = 1.27).

[32] H. Miyazaki and K. Ohtaka, *Near-Field Images of a Monolayer of Periodically Arrayed Dielectric Spheres*, Phys. Rev. B **58**, 6920 (1998).

[33] M. G. Bawendi, P. J. Carroll, W. L. Wilson and L. E. Brus, *Luminescence Properties of CdSe Quantum Crystallites: Resonance Between Interior and Surface Localized States*, J. Chem. Phys. **96**, 946 (1992).

[34] A. F. Koenderink, M. Kafesaki, C. M. Soukoulis and V. Sandoghdar, *Spontaneous Emission in the Near Field of Two-Dimensional Photonic Crystals*, Opt. Lett. **30**, 3210 (2005).

CHAPTER 6

CALCULATIONS OF LOCAL DENSITY OF STATES IN TITANIA INVERSE OPALS

We investigate the local density of states (LDOS) in TiO_2 inverse-opal photonic crystals. We used a recognized technique to calculate optical properties of periodic structures, known as the H-field plane-wave expansion method. To check the validity of our program code, we compared our computations with the known DOS in vacuum and with earlier results on the LDOS in 3D periodic structures. We calculated the LDOS in many different positions in the TiO_2 inverse opals. With the aim of finding a theoretical explanation of our experimental observations described in Chapter 5, we calculated the LDOS in several positions on the internal TiO_2-air interface. We find that the LDOS in the inverse opals strongly depends on the crystal lattice parameter as well as on the position and orientation of emitting dipoles. Near the first-order stopgap, the frequency-dependent shape of the LDOS is surprisingly similar at all investigated positions and dipole orientations. This is in agreement with the experimental observations. We identify special locations, frequencies and dipole orientations, where TiO_2 inverse opals have exciting features important for quantum electrodynamics such as strongly enhanced and inhibited LDOS and van Hove singularities.

6.1 Plane-wave expansion method

Knowledge of the LDOS is important for controlling spontaneous decay rates, as discussed in Chapter 5. The H-field plane-wave expansion method is an effective tool to compute the band structures and the LDOS in photonic crystals [1–4]. According to the Bloch theorem, which is the base of the plane-wave method, the Bloch modes of a photonic crystal can be expressed as a product of plane waves and functions describing the periodicity of the crystal lattice. These known periodic functions are expanded into Fourier series and inserted into the wave equation, which results in the infinite equation set given by Eq. 2.45. To compute the eigenfrequencies $\omega_n(\mathbf{k})$ and the expansion coefficients

of the eigenmodes $\mathbf{u}_{\mathbf{G}}^{n,\mathbf{k}}$, the infinite equation set is truncated: the reciprocal-lattice vectors $\mathbf{G}$ are restricted to a finite set $\mathcal{G}$ with N_G elements. This results in a $3N_G$ dimensional equation set:

$$-\sum_{\mathbf{G}'\in\mathcal{G}} \eta_{\mathbf{G}-\mathbf{G}'}(\mathbf{k}+\mathbf{G})\times[(\mathbf{k}+\mathbf{G}')\times\mathbf{u}_{\mathbf{G}'}^{n,\mathbf{k}}] = \frac{\omega_n(\mathbf{k})^2}{c^2}\mathbf{u}_{\mathbf{G}}^{n,\mathbf{k}}, \quad \forall\ \mathbf{G}\in\mathcal{G}. \tag{6.1}$$

The transversality of the H-field gives an additional condition: $(\mathbf{k}+\mathbf{G})\cdot\mathbf{u}_{\mathbf{G}}^{n,\mathbf{k}} = 0$, which eliminates one component of $\mathbf{u}_{\mathbf{G}}^{n,\mathbf{k}}$. Following Ref. [3], for each $\mathbf{k}+\mathbf{G}$ one needs to find two orthogonal unit vectors $\mathbf{e}_{\mathbf{k}+\mathbf{G}}^{1,2}$ that form an orthogonal triad with $\mathbf{k}+\mathbf{G}$. By expressing the eigenmode expansion coefficients in the plane normal to $\mathbf{k}+\mathbf{G}$ as $\mathbf{u}_{\mathbf{G}}^{n,\mathbf{k}} = u_{\mathbf{G},1}^{n,\mathbf{k}}\mathbf{e}_{\mathbf{k}+\mathbf{G}}^{1} + u_{\mathbf{G},2}^{n,\mathbf{k}}\mathbf{e}_{\mathbf{k}+\mathbf{G}}^{2}$, we remove one third of the unknowns. Equation set 6.1 becomes

$$\sum_{\mathbf{G}'\in\mathcal{G}} \eta_{\mathbf{G}-\mathbf{G}'}|\mathbf{k}+\mathbf{G}||\mathbf{k}+\mathbf{G}'|\begin{pmatrix} \mathbf{e}_{\mathbf{k}+\mathbf{G}}^{2}\cdot\mathbf{e}_{\mathbf{k}+\mathbf{G}'}^{2} & -\mathbf{e}_{\mathbf{k}+\mathbf{G}}^{2}\cdot\mathbf{e}_{\mathbf{k}+\mathbf{G}'}^{1} \\ -\mathbf{e}_{\mathbf{k}+\mathbf{G}}^{1}\cdot\mathbf{e}_{\mathbf{k}+\mathbf{G}'}^{2} & \mathbf{e}_{\mathbf{k}+\mathbf{G}}^{1}\cdot\mathbf{e}_{\mathbf{k}+\mathbf{G}'}^{1} \end{pmatrix}\begin{pmatrix} u_{\mathbf{G}',1}^{n,\mathbf{k}} \\ u_{\mathbf{G}',2}^{n,\mathbf{k}} \end{pmatrix}$$

$$= \frac{\omega_n(\mathbf{k})^2}{c^2}\begin{pmatrix} u_{\mathbf{G},1}^{n,\mathbf{k}} \\ u_{\mathbf{G},2}^{n,\mathbf{k}} \end{pmatrix}, \quad \forall\ \mathbf{G}\in\mathcal{G}. \tag{6.2}$$

To find the Fourier coefficients $\eta_{\mathbf{G}-\mathbf{G}'}$, we used the method of Ref. [1]: the coefficients are computed by first Fourier-transforming the dielectric function $\epsilon(\mathbf{r})$, truncating and inverting the resulting matrix. This approach considerably improves the convergence of the plane-wave method [5]. The results obtained with $N_G = 725$ deviate by less than 0.5 % from the converged band structures [4]. Solving Equation set 6.2 gives the frequencies $\omega_n(\mathbf{k})$ and H-field eigenmodes $\mathbf{H}_{n,\mathbf{k}}(\mathbf{r})$ in the photonic crystal. Then, using the Maxwell equations (Eqs. 2.39), the E-fields $\mathbf{E}_{n,\mathbf{k}}(\mathbf{r})$ are obtained from

$$\mathbf{E}_{n,\mathbf{k}}(\mathbf{r}) = \frac{1}{\omega_n(\mathbf{k})\epsilon_0}\sum_{\mathbf{G},\mathbf{G}'\in\mathcal{G}} \eta_{\mathbf{G}'-\mathbf{G}}|\mathbf{k}+\mathbf{G}|(u_{\mathbf{G},1}^{n,\mathbf{k}}\mathbf{e}_{\mathbf{k}+\mathbf{G}}^{2} - u_{\mathbf{G},2}^{n,\mathbf{k}}\mathbf{e}_{\mathbf{k}+\mathbf{G}}^{1})e^{i(\mathbf{k}+\mathbf{G}')\cdot\mathbf{r}}. \tag{6.3}$$

To compute the LDOS (Eq. 2.54), the integration over $\mathbf{k}$ needs to be discretized. The expression for the LDOS is then written as

$$N(\mathbf{r},\omega,\mathbf{e}_d) = \sum_{n,\mathbf{k}} \delta(\omega-\omega_{n,\mathbf{k}})|\mathbf{e}_d\cdot\mathbf{E}_{n,\mathbf{k}}(\mathbf{r})|^2, \tag{6.4}$$

where the number of k-points should be as large as possible for a better calculation accuracy. In our computations, the k-space of the first Brillouin zone is represented by an equidistant grid consisting of 291416 k-points. The LDOS histograms are plotted versus the reduced frequency $a/\lambda = \omega a/2\pi c$, where a is the cubic lattice parameter. The frequency resolution of the histograms in our calculations is 10 points per $\Delta a/\lambda = 0.1$.

To calculate the LDOS in 3D periodic structures is a very complicated and time-consuming task. The chosen degree of the k-space discretization (291416 k-points) and the number of plane-waves (N_G = 725) are in balance between the accuracy and time of the calculations. Using a personal computer Pentium (R)4CPU 3.2 GHz and 1 GB RAM, it takes about 7 days to compute the LDOS at several positions in the 3D structures using the above-mentioned settings. In calculations of the total density of states (DOS)[(1)], it is possible to narrow the integration over **k** down to the irreducible Brillouin zone. Furthermore, it is not necessary to compute the E-fields. These two factors drastically reduce the computational burden. The expression for the LDOS contains the term $|\mathbf{E}_{n,\mathbf{k}}(\mathbf{r})|$, and it is important to realize that in photonic crystals $\mathbf{E}_{n,\mathbf{k}}(\mathbf{r})$ varies under the lattice point-group operations so that $|\mathbf{E}_{n,\alpha[\mathbf{k}]}(\mathbf{r})| \neq |\mathbf{E}_{n,\mathbf{k}}(\mathbf{r})|$, as shown in Ref. [6]. Unfortunately, in several previous reports on the LDOS, this symmetry property was not appreciated, resulting in erroneous effects, see Ref. [6]. Hence, we perform the integration over the entire Brillouin zone to obtain the correct LDOS.

6.2 Comparison with previous results

To test our computations, we compared our results with earlier ones: we have calculated the DOS and LDOS in vacuum and in an *fcc* crystal consisting of dielectric spheres with ϵ_1 = 7.35 in a medium with ϵ_2 = 1.77. The spheres occupy 25 vol % of the crystal, as in Refs [3, 6]. In Figure 6.1 we present the total DOS in the photonic crystal and compare our result (empty circles) to that from Ref. [3] (curve with dots). We can reproduce the earlier calculations of the total DOS: both results shown in Fig. 6.1 are in excellent agreement, with deviations smaller than 2 %. Figure 6.2a shows the LDOS in vacuum with an averaged dipole orientation: the projected LDOS for three mutually orthogonal orientations is summed. In this case the LDOS should be obviously equal to the DOS. However, for the purpose of testing, we have calculated the LDOS in several positions in the unit cell of the fictitious crystal with zero dielectric contrast. The resulting LDOS is identical in all the positions and increases parabolically with frequency in agreement with the theory (Eq. 2.37): the random deviations, due to the finite k-space discretization, amount less than 3.5 %.

[(1)] The DOS is the unit-cell and dipole-orientation average of the LDOS defined as $N(\omega) = \sum_n \int_{BZ} d\mathbf{k}\delta(\omega - \omega_{n,\mathbf{k}})$.

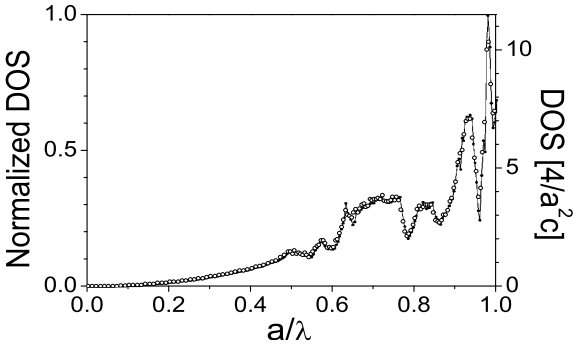

FIGURE 6.1: DOS in an *fcc* crystal consisting of spheres with ϵ = 7.35 in a medium with ϵ = 1.77 with a filling fraction of the spheres of 25 vol %. The solid dotted curve represents calculations from Ref. [3].

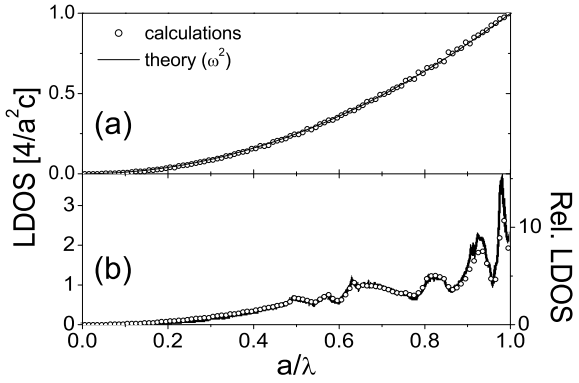

FIGURE 6.2: (a) Dipole-averaged LDOS in vacuum (empty circles) compared to the analytically derived ω^2 behavior (curve). (b) Dipole-averaged LDOS in the same photonic crystal as in Fig. 6.1 at a position $(\frac{1}{4}, \frac{1}{4}, 0)$. The empty circles are for our calculations, and the solid curve represents results from Ref. [6]. The relative LDOS is the ratio of the LDOS to that in vacuum at a/λ = 0.495.

In Figure 6.2b we demonstrate the LDOS in the same photonic crystal as in Fig. 6.1 at a point equidistant from two spheres. In this calculation, we used the same number of reciprocal-lattice vectors $N_G = 965$ as in Ref [6]. We find that our calculations (empty circles) are in good agreement with the LDOS calculated previously (solid curve). The small deviations at high frequencies are perhaps due to a lower frequency resolution $\Delta a/\lambda$ in our calculations: larger frequency steps resulted in a smoothing of the sharp peaks in the LDOS.

6.3 LDOS in TiO_2 inverse opals

To calculate the LDOS in our TiO_2 inverse-opal photonic crystals, we modeled the position dependence of the dielectric function $\epsilon(\mathbf{r})$ as shown in Figure 6.3. We assumed an infinite *fcc* lattice of air spheres with radius $r = 0.25\sqrt{2}a$ (a is the cubic lattice parameter).

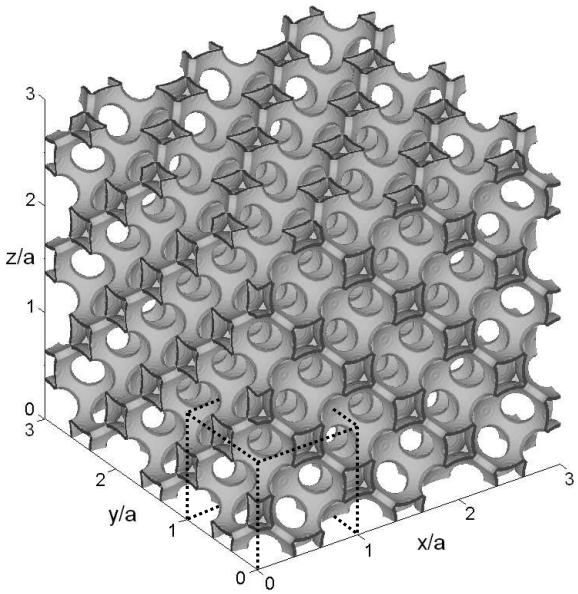

FIGURE 6.3: Model of the inverse-opal structure (3x3x3 unit cells): an fcc lattice of air spheres of radius $r = 0.25\sqrt{2}a$ with a being the cubic lattice parameter. The spheres are covered by shells with $\epsilon = 6.5$ and outer radius $1.09r$. Neighboring air spheres are connected by windows of radius $0.4r$. The black cleaved edges are (100) facets. The dashed lines indicate the boundaries of a cubic unit cell.

The spheres are covered by overlapping dielectric shells ($\epsilon = 6.5$) with outer radius $1.09r$. Neighboring air spheres are connected by cylindrical windows of radius $0.4r$. These parameters are inferred from SEM observations and correspond to a volume fraction of TiO_2 of about 10.7 %, which is consistent with the structural characterization of the inverse opals [7]. Moreover, the photonic band structure calculated using this model agrees with reflectivity measurements in the ranges of both the first-order and second-order Bragg diffraction [8].

Henceforth, we will consider the relative LDOS, which is the ratio of the LDOS in a photonic crystal to that in a homogeneous medium with the same average refractive index. The LDOS in a homogeneous medium is equal to $n_{av}(a/\lambda)^2/3$, where $n_{av} = 1.27$. In Figure 6.4a we plot the resulting LDOS at three positions in the unit cell: in $\mathbf{r}$ = (0,0,0), $\frac{1}{4}(1,1,1)$ and ($\frac{1}{2}$,0,0). Due to the high symmetry of these points, the LDOS there does not depend on the dipole orientation.

The first observation in Fig. 6.4a is that the LDOS strongly varies with reduced frequency revealing troughs and peaks caused by the lowest-order L-gap near $a/\lambda = 0.7$ and by higher-order stopgaps at $a/\lambda > 1.15$. In position $\mathbf{r}$ = (0,0,0) there is a sharp, factor-of-three enhancement at $a/\lambda \approx 1.35$ within a very narrow frequency range. On the other hand, at a/λ around 1.25, the mode density has a wide inhibition at $\mathbf{r}$ = ($\frac{1}{2}$,0,0).

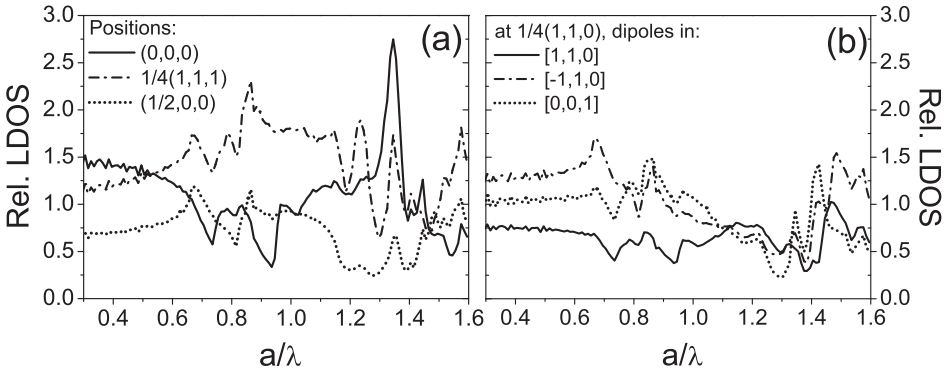

FIGURE 6.4: Relative LDOS in the inverse opal shown in Fig 6.3 at three different positions: (a) $\mathbf{r}$ = (0,0,0) [the center of an air sphere, solid curve], $\mathbf{r} = \frac{1}{4}(1,1,1)$ [among three air spheres, dash-dotted curve] and $\mathbf{r}$ = ($\frac{1}{2}$,0,0) [midway between two spheres along [1,0,0] direction, dotted curve]; (b) $\mathbf{r} = \frac{1}{4}(1,1,0)$ [in the window between two spheres] projected on [1,1,0], [-1,1,0] and [0,0,1] directions shown by solid, dash-dotted and dotted curves, respectively.

The second observation from Fig. 6.4a is that the LDOS at all reduced frequencies differs considerably among these three positions.

The third observation is that, at another position with less symmetry, there is a clear dependency on the dipole orientation as can be seen in Figure 6.4b. We should emphasize here that for emitters with fixed or slowly varying dipole orientations (*e.g.*, dye molecules and quantum dots on solid surfaces), the emission rate is determined by the optical modes that are projected on the dipole orientations. Therefore, knowledge of the projected LDOS is important for controlling spontaneous-emission rates as well as for interpreting the data from experiments on emitters in photonic media.

At low frequencies, $a/\lambda < 0.5$, the relative LDOS hardly varies with frequency, which means that the mode density is proportional to ω^2, as in a homogeneous medium. Still, the position-dependence of the LDOS is also apparent at the low frequencies. The reason is that the photonic Bloch modes exhibit local variations of the electromagnetic fields related to local variations of the dielectric function. Thus, the LDOS is position-dependent even at low frequencies relative to the crystal periodicity.

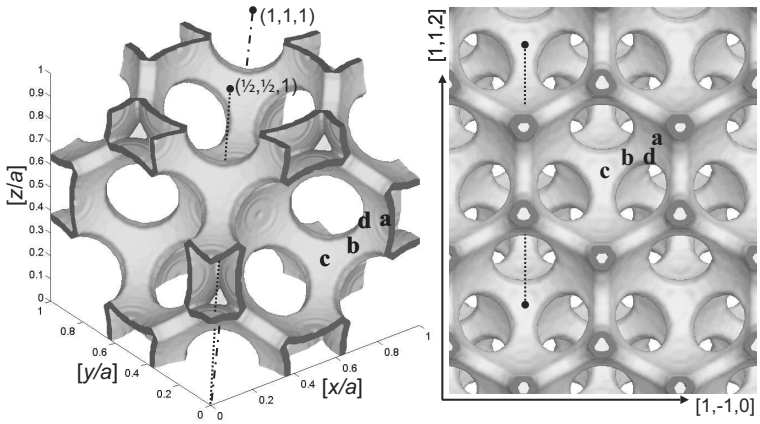

FIGURE 6.5: (*Left*) View of a single unit cell of the modeled inverse opal. (*Right*) Cut of the inverse opal along (111) facet. The letters indicate different positions at the TiO_2-air interface equivalent to: **a** = $\frac{1}{2\sqrt{2}}$(1,0,0), **b** = $\frac{1}{4\sqrt{3}}$(1,1,2), **c** = $\frac{1}{2\sqrt{6}}$(1, 1, 1) and **d** = (0.33,0.13,0). The dash-dotted line (*Left*) shows the main diagonal of the cubic unit cell. The dotted line (*Left* and *Right*) indicates [1,1,2] direction that belongs to the (111) crystal plane.

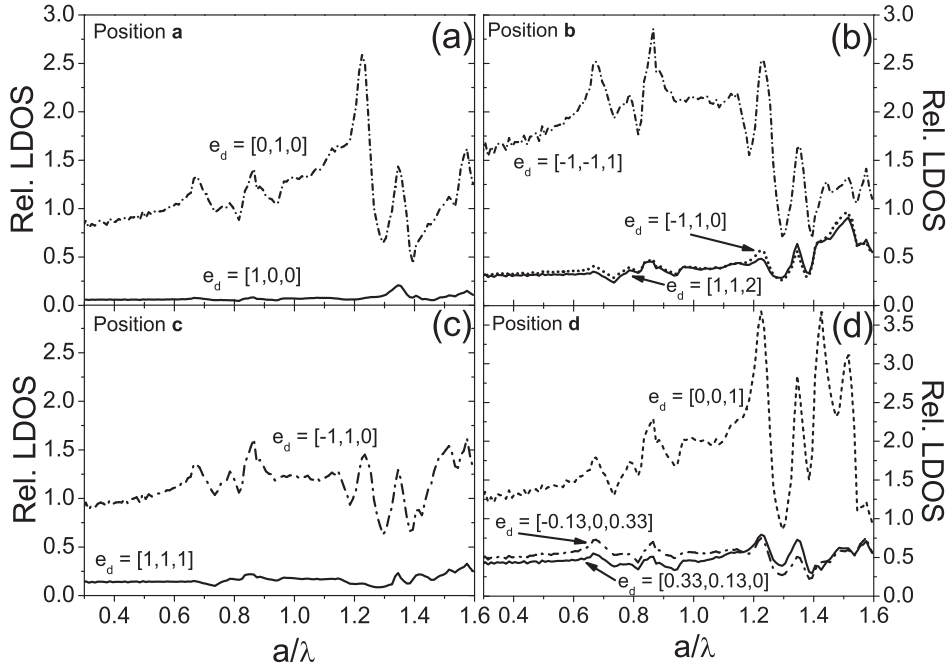

FIGURE 6.6: Relative LDOS in the inverse opal at four different positions on the TiO_2-air interface shown in Fig. 6.5. At each position the LDOS is projected on three mutually orthogonal dipole orientations $\mathbf{e}_d$. (a) point **a** for $\mathbf{e}_d$ = [1,0,0] and [0,1,0]. LDOS at $\mathbf{e}_d$ = [0,0,1] and [0,1,0] is the same. (b) point **b** for $\mathbf{e}_d$ = [1,1,2], [-1,1,0] and [-1,-1,1]. (c) point **c** for $\mathbf{e}_d$ = [1,1,1] and [-1,1,0]. LDOS at $\mathbf{e}_d$ = [-1,-1,2] is equal to that at $\mathbf{e}_d$ = [-1,1,0]. (d) point **d** for $\mathbf{e}_d$ = [0.33,0.13,0], [-0.13,0,0.33] and [0,0,1].

In the time-resolved emission experiments described in Chapter 5, we studied radiative decay rates of the quantum dots, which were distributed at the internal TiO_2-air interfaces of the inverse opals. To compare our experimental data to the theory, we have calculated the LDOS at several symmetry-inequivalent positions on the internal interfaces. Figure 6.5 shows a single unit cell (*Left*) and a (111) facet (*Right*) of the modeled inverse opal. The plot in Fig. 6.5(*Right*) is convenient for comparison with SEM images of the real inverse opals, which often reveal the crystal surface cut along the (111) plane (*e.g.*, see Fig. 3.5).

We have calculated the LDOS at the indicated positions **a**, **b**, **c** and **d** for three mutually orthogonal orientations of the emitting dipole $\mathbf{e}_\mathrm{d}$, where the first orientation is chosen along the vector pointing from (0,0,0) toward the corresponding point. Figures 6.6a - 6.6d show that at all those points the resulting LDOS varies with the reduced frequency and strongly depends on both the position and orientation of the dipole. Furthermore, the plots reveal that for the dipoles perpendicular to the TiO_2-air interface, the LDOS is noticeably inhibited (by factors of 2 to 8) at all reduced frequencies compared to dipoles parallel to the interface.

In the reduced frequency range up to $a/\lambda = 1.1$, the dependence of the LDOS on the lattice parameter is very similar at all the positions and dipole orientations. This result is remarkable because it nicely agrees with the observation made in Chapter 5: the complex decay curves of quantum-dot emission from the inverse opals are explained by a single shape (log-normal) of the decay-rate distribution for all reduced frequencies studied.

At higher frequencies we see large variations of the LDOS versus lattice parameter, position and dipole orientation. The LDOS at position **a** shows a steep slope at $a/\lambda \approx 1.2$, where it abruptly changes by a factor of 4. Positions **b** and **d** show similarly steep LDOS variations within a narrow a/λ range. Such sharp peaks in the LDOS (van Hove singularities) are very desirable for realization of strong emitter-field coupling and non-exponential decay dynamics of emission from single sources. At $a/\lambda \approx 1.3$ the LDOS is inhibited for all the positions and dipole orientations (also in Fig. 6.4). The lowest LDOS that we find is inhibited 18 times compared to the homogeneous medium. It is remarkable because this trough in the LDOS found for many locations and dipole orientations is due to stopgaps with little dispersion and is a precursor of a photonic bandgap [8].

To consider the spatial distribution of the LDOS in the inverse opals, we have performed calculations along characteristic directions in the unit cell. Figure 6.7 shows variation of the LDOS at four key frequencies along the [1,1,1] direction: the main diagonal

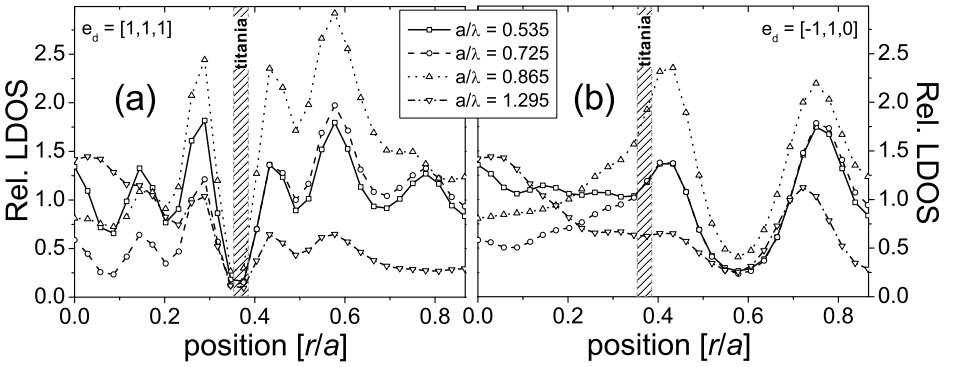

FIGURE 6.7: Relative LDOS at four key frequencies, a/λ = 0.535, 0.725, 0.865 and 1.295, in the inverse opal as a function of the distance r from (0,0,0) point along [1,1,1] direction. The LDOS is projected on two dipole orientations $\mathbf{e}_d$: (a) [1,1,1] and (b) [-1,1,0]. LDOS at $\mathbf{e}_d$ = [-1,-1,2] and [-1,1,0] is equal. The hatched boxes indicate the position of the TiO_2 shell. For $r/a \in [\frac{\sqrt{3}}{2}, \sqrt{3}]$ the LDOS is mirror-symmetric to that in the presented region.

of the cubic unit cell. The LDOS at those frequencies depends on position and has clear minima and minima along the diagonal. The LDOS projected on the [1,1,1] direction is strongly (> 5x) suppressed near the TiO_2 shell ($r/a \approx 0.353$) at all the frequencies (Fig. 6.7a). This agrees with the LDOS at position **c** on the shell shown in Fig. 6.6c. On the other hand, the mode density for [1,1,1] dipole orientation is enhanced at $r/a \approx 0.28$ and 0.57: almost 2.5 and 3 times, respectively. For orientations in the [-1,1,0] and [-1,-1,2] directions, the LDOS is inhibited at $r/a \approx 0.57$ for all the frequencies, as seen in Fig. 6.7b. This position $r/a = 1/\sqrt{3} \approx 0.57$ lies in the (111) lattice plane - the most close-packed plane in the *fcc* crystal lattice. It is therefore interesting to consider the LDOS behavior in that plane.

In Figure 6.8 we show the LDOS at the four frequencies along a line that lies in the (111) plane and connects the centers of two spheres: (0,0,0) and $(\frac{1}{2}, \frac{1}{2}, 1)$ as shown in Fig. 6.5 by the dotted lines. We see that for the dipole orientation $\mathbf{e}_d$ = [1,1,2], the LDOS at all four frequencies is strongly inhibited in the node amid three air-spheres (r/a around 0.4) and is enhanced just outside the node. The LDOS projected on the [-1,1,0] direction does not show any sharp features besides the suppression in the node. For the dipole oriented perpendicularly to the (111) plane ($\mathbf{e}_d$ = [-1,-1,1]), the LDOS is enhanced at two frequencies a/λ = 0.535 and 0.725, and is even more strongly enhanced at a/λ = 0.865.

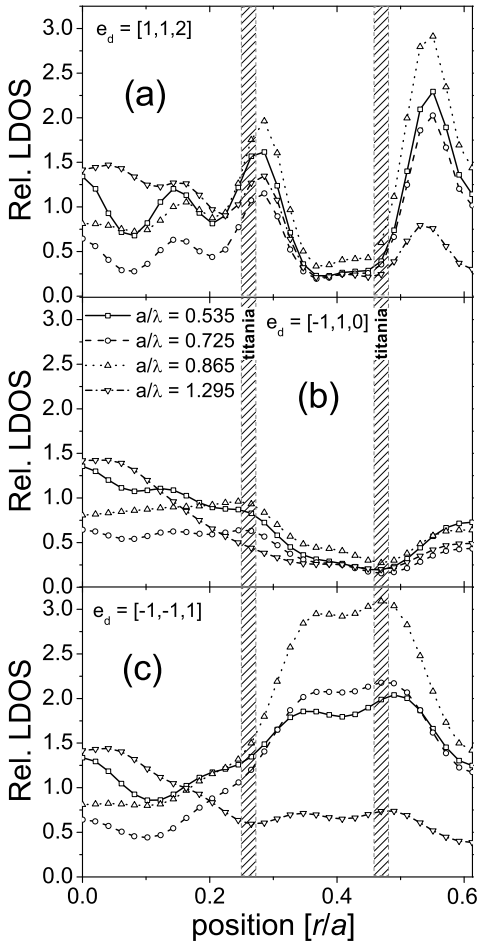

FIGURE 6.8: Relative LDOS in the inverse opal as a function of the distance r from (0,0,0) point along [1,1,2] direction for the same frequencies as in Fig. 6.7. The LDOS is projected on three dipole orientations $\mathbf{e}_\mathrm{d}$: (a) [1,1,2], (b) [-1,1,0] and (c) [-1,-1,1]. The hatched boxes indicate the TiO_2 shells. For $r/a \in [\frac{1}{2}\sqrt{\frac{3}{2}}, \sqrt{\frac{3}{2}}]$ the LDOS is mirror-symmetric to the LDOS in the presented r/a region.

6.4 Conclusions

We have managed to perform intensive calculations of the local density of states (LDOS) in the TiO_2 inverse opals, using the H-field plane-wave expansion method. To check the validity of our program code, we have compared our computations with the theoretically known DOS in vacuum and with the earlier results on the LDOS. We have calculated the projected LDOS in various positions in the TiO_2 inverse opals, aiming to find a theoretical explanation of the experimental results described in Chapter 5. The results of our numerical calculations revealed a surprisingly strong dependence of the LDOS on the orientation of the emitting dipoles. At frequencies near the first-order stopgap, the dependence of the LDOS on the crystal lattice parameter is preserved at all investigated positions and dipole orientations, in agreement with the experiment. We have identified conditions where the LDOS is strongly enhanced, strongly inhibited and where the van Hove singularities appear. These predictions mean that the TiO_2 inverse opals can have a great potential for studies of quantum electrodynamics of embedded light sources.

References

[1] K. M. Ho, C. T. Chan and C. M. Soukoulis, *Existence of a Photonic Gap in Periodic Dielectric Structures*, Phys. Rev. Lett. **65**, 3152 (1990).

[2] H. S. Sözüer, J. W. Haus and R. Inguva, *Photonic Bands: Convergence Problems with the Plane-Wave Method*, Phys. Rev. B **45**, 13962 (1992).

[3] K. Busch and S. John, *Photonic Band Gap Formation in Certain Self-Organizing Systems*, Phys. Rev. E **58**, 3896 (1998).

[4] A. F. Koenderink, *Emission and Transport of Light in Photonic Crystals*, Ph.D. thesis, University of Amsterdam, ISBN: 90-9016903-2 (2003).

[5] R. D. Meade, A. M. Rappe, K. D. Brommer, J. D. Joannopoulos and O. L. Alerhand, *Accurate Theoretical Analysis of Photonic Band-Gap Materials*, Phys. Rev. B **48**, 8434 (1993).

[6] R. Wang, X.-H. Wang, B.-Y. Gu and G.-Z. Yang, *Local Density of States in Three-Dimensional Photonic Crystals: Calculation and Enhancement Effects*, Phys. Rev. B **67**, 155114 (2003).

[7] J.E.G.J. Wijnhoven, L. Bechger and W. L. Vos, *Fabrication and Characterization of Large Macroporous Photonic Crystals in Titania*, Chem. Mater. **13**, 4486 (2001).

[8] W. L. Vos and H. M. van Driel, *Higher Order Bragg Diffraction by Strongly Photonic FCC Crystals: Onset of a Photonic Bandgap*, Phys. Lett. A **272**, 101 (2000).

CHAPTER 7

MODIFICATION OF RADIATIVE RATES OF DYE IN OPAL PHOTONIC CRYSTALS

This chapter presents a time-resolved study of spontaneous emission from Rhodamine 6G dye in opal photonic crystals. We have measured fluorescence lifetimes of the dye by varying both optical frequency and crystal lattice parameter of polystyrene opals. The observed fluorescence lifetimes are nearly frequency independent within the dye emission spectrum. This effect is attributed to a broad homogeneous linewidth of the dye, which means that dye molecules probe the local density of states (LDOS) in the photonic crystals averaged over all frequencies of the homogeneous spectrum. Fluorescence lifetimes of the dye are modified when the crystal lattice parameter is changed: we observe 16 % enhancement and 10 % inhibition of spontaneous emission, which is explained by the varying LDOS in the opals. The changes of spontaneous emission induced by the polystyrene opals are considerably smaller than the effects measured in the titania inverse opals. This agrees with much weaker changes of the LDOS in the opals with respect to those in the inverse opals.

7.1 Introduction

Since 1987, when the potential of photonic crystals in inhibition of spontaneous emission was firstly pointed out [1], there has been a lot of efforts to observe modified emission rates in photonic crystals. Early emission experiments were performed on opal photonic crystals: these crystals consisting of close-packed *fcc* lattices of monodisperse spheres from silica or polystyrene can be relative easily fabricated by self-assembly. Already in 1990, the first report appeared [2], where the emission decay of a dye in an ordered aqueous suspension of polystyrene spheres was inhibited by a factor of 1.75 compared to a disordered reference sample. In another emission experiment on dye molecules dissolved in the same suspension systems [3], a similar inhibition of the decay rate was observed. However, in the second work, the authors ascribed the observed large modification to

variations of the chemical environment of the dye molecules. They showed that changes of the chemical environment can lead to large effects on the fluorescence lifetimes. Later, in the measurements of the fluorescence of dyes in silica opals filled with a polymer, multi-exponential decays containing both accelerated and inhibited rates were observed [4] and compared to the dye fluorescence in a polymer film. The resulting accelerated and inhibited rates differed by a factor of 2 and were attributed to a redistribution of the density of states across the emission spectrum. This explanation was disputed in Ref. [5]: the studied opals had a low dielectric contrast and could only weakly modify spontaneous emission. The large factor-of-two difference is most likely caused by influence of the fluorescence from the backbone materials: the excitation of the dye in that experiment was performed in the UV range, and the detected emission was not spectrally resolved.

In the meantime, with the appearance of highly-efficient quantum dots and periodic structures with high dielectric contrasts, the scientific interest was diverted away from dyes and opals. In experiments on the quantum dots and wells embedded in strongly photonic crystals, considerable modifications of spontaneous-emission rates have been recently achieved [6–10]. The quantum dots, however, are very sensitive to water and oxygen and have features that are not well understood (blinking, photobrightening), as discussed elsewhere in this thesis. Furthermore, despite high brightness and resistance to bleaching of the quantum dots, difficulties in targeting of proteins in live cells are the main limitation of using these sources as fluorescent labels. In contrast, there is a great variety of highly-efficient in water organic molecules (dyes) that are widely used as fluorescent probes in studies of biological samples [11, 12]. It is, therefore, interesting to investigate if the radiative properties of the dyes can be controlled with photonic crystals.

7.2 Experiment

We have investigated dynamics of spontaneous emission from dye molecules embedded in opal photonic crystals. The measurements were performed on opals from polystyrene colloids with different cubic-lattice parameters ranging from 178 ± 3 nm to 922 ± 25 nm, a total of 7 samples. The opals were doped with Rhodamine 6G (R6G) - a well-known dye that has a high quantum efficiency of about 95 % [13, 14]. The process of the dye infiltration is described in detail in Chapter 4. The dye molecules are distributed on the surfaces of the polystyrene spheres constituting the opals. The excitation of the dye was

performed at as low as possible frequencies to avoid fluorescence from the backbone of the photonic crystals. We found that the polystyrene backbone fluoresces when wavelengths shorter than 450 nm are used for excitation. Therefore, we used a pulsed LED (Picoquant, PLS 500), which emits at λ = 502 nm in a bandwidth of 32 nm and has a pulse width of 600 ps. The time between consecutive pulses was set to 50 ns. The pump beam was focused to a spot of about 1 mm in diameter on the sample surface. The scattered pump light was filtered out. We used the same set-up that is described in Chapter 4 to detect R6G emission from the photonic crystals. The time-resolved fluorescence intensity was measured at different frequencies within narrow bands of $\Delta\omega \approx 85$ cm^{-1} using the time-correlated single-photon counting, similarly to the experiment on quantum dots described in Chapter 5. Due to the high quantum efficiency of R6G, the decay of the excited state is dominated by the radiative process, and the measured decay rate (inverse lifetime) γ_{tot} is nearly equal to the radiative decay rate γ_{rad}.

7.3 Experimental results

Propagation of emitted light in photonic crystals is affected by the stopbands, as we could see in the angle-resolved study of emission spectra presented in Chapter 4. The stopbands also change the LDOS, which has effects on the dynamics of spontaneous emission of light sources embedded in photonic crystals. In Figure 7.1 we plotted emission spectra of R6G dye in polystyrene opals with different lattice parameters. The spectra from the opals with lattice parameters a = 365 and 682 nm are modified by the first- and second-order Bragg diffraction, respectively. In contrast, in the opal with a = 178 nm, the emission frequencies of R6G are in the low-frequency limit, and therefore, no stopbands are observed.

In the time-resolved experiments, we study influence of the opal photonic crystals on the fluorescence decay of R6G by varying the crystal lattice spacing and detecting the fluorescence at different emission frequencies. Figure 7.2 shows examples of the time-resolved traces of R6G emission in polystyrene opals with three different lattice parameters. The decay curves were recorded at the maximum of the R6G spectrum at λ = 556 nm. The apparent difference in the slopes of these decay curves indicates a modified radiative lifetime. Spontaneous emission in opals with lattice parameters a = 365 and 682 nm, which reveal effects of Bragg diffraction within R6G emission spectrum, is inhibited comparing to the low-frequency opal.

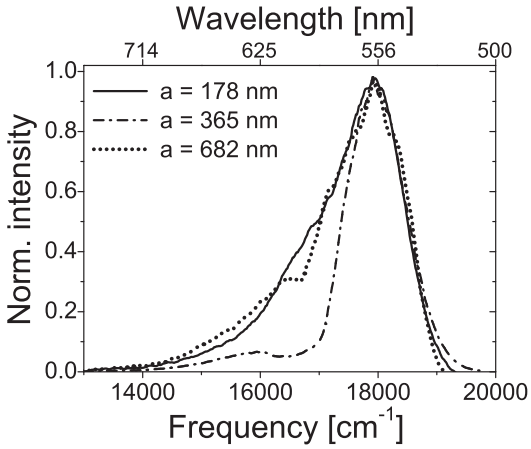

FIGURE 7.1: Normalized emission spectra of R6G in polystyrene opals with three different lattice parameters: a = 178 nm (solid curve), a = 365 nm (dash-dotted curve) and a = 682 nm (dotted curve). In the opal with a = 178 nm, the frequencies of R6G emission lie far below the first-order stopband. Emission from the opal with a = 365 nm reveals the first-order stopband, whose angle-dependence is presented in Chapter 4. Spectrum from the opal with a = 682 nm shows effects of the second-order Bragg diffraction that presented in more detail in Ref. [15].

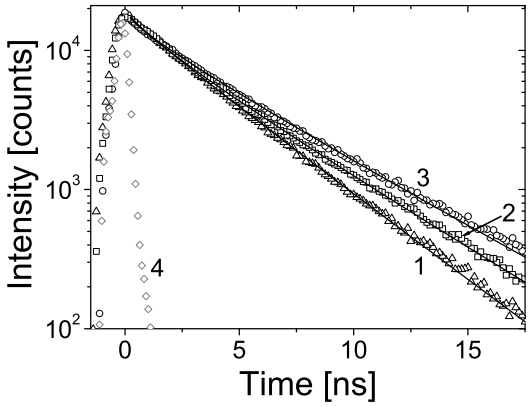

FIGURE 7.2: Fluorescence decay curves recorded at ω = 17985 cm^{-1} (λ = 556 nm) from R6G dye in polystyrene opals with lattice parameters a = 178 nm (1), 365 nm (2) and 682 nm (3), together with the instrument response convoluted with the excitation pulse (4). Curves 1 and 2 are overlapped at 0 ns with curve 3. Solid lines are fits with the stretched-exponential model.

The decay curves shown in Fig. 7.2 are not strictly single-exponential, whereas the decay of R6G emission in homogeneous media is explicitly mono-exponential. The slight deviation from pure mono-exponential decay is because the dye molecules at different positions on the polystyrene spheres couple to different LDOS and, hence, reveal different lifetimes. Effects of reabsorption and fluorescence quenching, which can also lead to non-exponential decays, are excluded due to a very low (10^{-6} mol/l) doping concentration of the dye, as discussed in the previous chapters. Thus, to infer the fluorescence lifetimes (inverse decay rates), we needed to model the measured decay curves. It is reasonably to assume that the decrease of the number $n(t)$ of excited dye molecules in the opals is characterized by a narrow distribution of lifetimes. This excited-state behavior can be modeled by the stretched exponential [(1)] - a widely-used model with only two adjustable parameters (see, *e.g.*, [16]) that is defined as

$$n(t) = n_0 \exp(-t/\tau)^{\beta}. \tag{7.1}$$

Here β is the stretch parameter that varies between 0 and 1, and τ is the time when $n(t)$ decreases e-times. The stretch parameter β is qualitatively related to a lifetime distribution: β near 1 corresponds to a very narrow distribution, and smaller β, to a broad distribution. The corresponding fluorescence decrease proportional to the time-derivative of $n(t)$ (see Appendix B or [17]) is then modeled as

$$I(t) = I_0(\beta/t)(t/\tau)^{\beta} \exp(-t/\tau)^{\beta}. \tag{7.2}$$

The main advantage of this model is that the average lifetime τ_{av} can be readily calculated:

$$\tau_{\mathrm{av}} = (\tau/\beta)\,\Gamma(1/\beta), \tag{7.3}$$

where Γ is the Gamma-function. We have modeled all measured fluorescence decay traces with the stretched exponential (Eq. 7.2): the results of modeling are shown by the solid curves in Fig. 7.2. The stretch parameter β is close to 1, varying between 0.92 and 0.99. From the obtained parameters τ and β, we have calculated the average fluorescence lifetime using Eq. 7.3.

7.3.1 Fluorescence lifetime in opals vs. frequency

In Figure 7.3 we present the frequency dependence of the average lifetime τ_{av} for R6G emission in several opals with different lattice parameters. The data from all samples

[(1)] The analysis of the R6G decay curves was done before we had learned modeling with decay-rate distributions.

reveal a slight (< 8 %) decrease of τ_{av} with increasing emission frequency, which is in agreement with previous results [18–20]. These small lifetime changes compared to expected ω^3-behavior can be explained if the spectral width of R6G is dominated by homogeneous line broadening. Indeed, spectra of dye molecules including R6G are homogeneously broadened because of a splitting of electronic energy levels due to interaction with molecular vibrational and rotational modes: the excited level consists of a ladder of sublevels $|a_i\rangle$ and the ground level, of a similar ladder of sublevels $|b_i\rangle$ [21, 22]. After excitation, a molecule quickly relaxes to the lowest excited electronic level $|a_1\rangle$ in a picosecond time scale. From this level, fluorescent transitions occur to different sublevels $|b_i\rangle$ of the ground electronic level. If, in a photonic crystal, a certain transition $|a_1\rangle \rightarrow |b_1\rangle$ is inhibited due to a low LDOS at the frequency of this transition, the excited state will decay via another $|b_2\rangle$ sublevel at a different frequency within the homogeneous linewidth of the dye. Therefore, modifications of the fluorescence lifetime in dyes can only be observed if the homogeneous linewidth is narrower than (or at least comparable to) features in the frequency dependence of the LDOS.

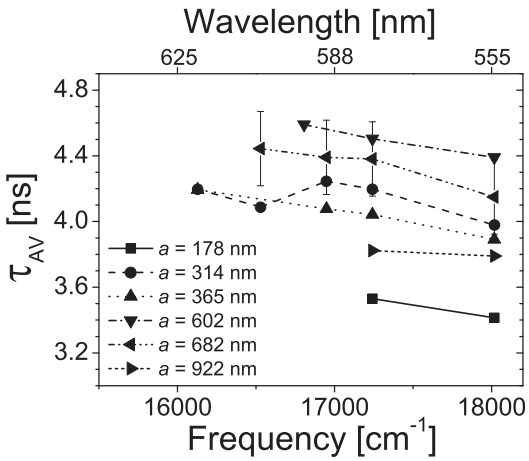

FIGURE 7.3: Average fluorescence lifetime τ_{av} vs. detection frequency obtained using the stretched exponential (Eq. 7.2) for R6G emission in polystyrene opals with lattice parameters a = 178, 314, 365, 602, 682 and 922 nm. The error bars shown for a = 682 nm are typical for all samples and estimated from the difference between data on samples with similar a. The lines connecting the data points are guides to the eye.

7.3.2 Decay rates vs. crystal lattice parameter

It is remarkable that the fluorescence lifetime is different in opals with different lattice parameters, as seen in Fig. 7.3. This indicates that the LDOS in the opals is modified in frequency ranges comparable or larger than the homogeneous linewidth of R6G. Figure 7.4a shows the measured decay rates (squares) of R6G versus reduced frequency $\omega a/2\pi c$, *i.e*, at fixed emission frequency ω = 17985 cm^{-1} and varying crystal lattice para-

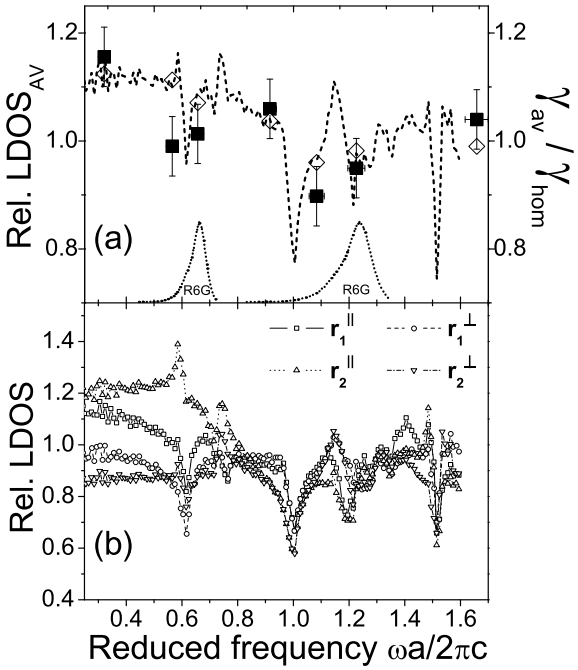

FIGURE 7.4: (a) Decay rates of R6G (squares) measured at ω = 17985 cm^{-1} and normalized to the rate in a homogeneous medium γ_{hom} = 0.254 ns^{-1}. Dipole- and position-averaged relative LDOS (dashed curve). The averaging was performed over five points on the internal surfaces: at $\mathbf{r}_1 = \frac{1}{2\sqrt{2}}(1,0,0)$, $\mathbf{r}_2 = \frac{1}{2\sqrt{6}}(1,1,1)$, $\mathbf{r}_3 = \frac{1}{4\sqrt{3}}(1,1,2)$, $\mathbf{r}_4$=(0.33,0.13,0) and $\mathbf{r}_5$=(0.23,0.23,0.14). Normalized rates (diamonds) calculated from the averaged LDOS using Eq. 7.4. Dotted curves indicate R6G emission spectrum plotted vs. reduced frequency for in opals with a = 365 and 682 nm. (b) Relative LDOS at two positions on internal opal surfaces, $\mathbf{r}_1$ and $\mathbf{r}_2$, projected on dipole orientations parallel (||) or normal ($\perp$) to internal polystyrene-air interfaces.

meter a. The decay rates are normalized to $\gamma_{\text{hom}} = 0.254$ ns^{-1},[2] which is the decay rate in a homogeneous medium with refractive index $n = 1.45$.

In order to find if the observed modifications of spontaneous-emission rates ($\gamma_{\text{av}} = 1/\tau_{\text{av}}$) agree with theory, we have calculated the LDOS in different positions on the internal surfaces of the opals, where dye molecules can be located. In Figure 7.4b we plotted the relative LDOS[3] at two illustrative positions in the opal, projected on two dipole orientations: parallel and perpendicular to the sphere surface. The plots clearly demonstrate variation of the LDOS with the reduced frequency, location as well as orientation of emitting dipoles. In our experiment we detected fluorescence from dyes that are randomly oriented and randomly distributed on the internal surface of the opals. Consequently, the measurements are compared to the LDOS that is averaged over several symmetry-inequivalent locations on the spheres constituting the opals and over random dipole orientations. The reduced-frequency dependence of the resulting averaged LDOS [Fig. 7.4a (dashed curve)] is in a good agreement with the experimental data.

However, due to the broad homogeneous linewidth of R6G, the decay rate of the dye is determined by the LDOS at all frequencies of its emission spectrum (dotted curves in Fig. 7.4a). In the experiments on quantum dots (Chapter 5), we could directly compare the measured decay rates to the calculated LDOS because the homogeneous linewidth of those emitters ($\Delta\omega/\omega \approx 0.025$) is narrow with respect to the LDOS features in the inverse opals. In case of R6G, we concluded that the emission spectrum ($\Delta\omega/\omega \approx 0.09$) is homogeneously broadened. The decay rate of emitters with a homogeneous spectrum $S(\omega)$ coupled to the LDOS $N(\omega, a)$ is therefore calculated as:

$$\gamma(a) = A \int_0^\infty \omega S(\omega) N(\omega, a) d\omega, \tag{7.4}$$

where A is a constant parameter that includes the transition dipole moment of R6G, and a is the lattice parameter of the photonic crystal. It can be recognized that this expression is a generalized form of Eq. 2.32. By inserting the spectrum of R6G and the LDOS (in units of $[4/a^2c]$) in Eq. 7.4, we calculated decay rates for opals with specific lattice parameters, which were then normalized to the calculated rate in a homogeneous medium with $n = 1.45$. The predicted decay rates still vary with the lattice parameter and are not smoothed

[2] This value is obtained knowing that R6G dissolved in ethanol ($n = 1.36$) has the quantum efficiency of 95 % and the decay rate of 0.25 ns^{-1} [14].

[3] As in the previous chapters, the LDOS is related to the LDOS in a homogeneous medium with refractive index $n = 1.45$, which is the effective refractive index of the polystyrene opals.

by the homogeneous emission spectrum because the latter has the width comparable to the widths of troughs and peaks in the LDOS.

From the observed modifications of the emission decay rates, which are also in agreement with theory, we conclude that the dynamics of spontaneous emission from dye molecules can be controlled by photonic crystals. The observed 15 % enhancement and 10 % inhibition of spontaneous emission in the opals are, however, rather comparing to the eight-fold modifications of emission rates from quantum dots in the inverse opals reported in Chapter 5. This observation is in accordance with the small changes of the LDOS in the polystyrene opals (Fig. 7.4a), which are much weaker than the LDOS variations as a function of reduced frequency, position and orientation of emitting dipoles in the titania inverse opals (see, *e.g.*, Fig. 6.6).

7.4 Conclusions

We have studied time-resolved spontaneous emission from Rhodamine 6G dye in opal photonic crystals made from polystyrene. The observed fluorescence lifetimes hardly vary with changing optical frequencies within the dye emission spectrum. This effect is attributed to a broad homogeneous linewidth of the dye, which means that dye molecules probe the LDOS in the photonic crystals that is averaged over all frequencies of the homogeneous spectrum. By changing the crystal lattice parameter, we do observe some modifications of the lifetimes, which testifies that the LDOS features in the opals are still broader than the homogeneous linewidth of the dye. The variations of the emission decay rates induced by the polystyrene opals are in agreement with the calculated changes of the LDOS integrated over the dye emission spectrum. The observed effects on spontaneous emission from the dye in the opals are considerably smaller than the effects measured in the titania inverse opals, which is in accordance with the large homogeneous linewidths of the dye compared to quantum dots, and with much weaker predicted changes of the LDOS in the opals with respect to the strong LDOS modifications predicted for the inverse opals.

References

[1] E. Yablonovitch, *Inhibited Spontaneous Emission in Solid-State Physics and Electronics*, Phys. Rev. Lett. **58**, 2059 (1987).

[2] J. Martorell and N. M. Lawandy, *Observation of Inhibited Spontaneous Emission in a Periodic Dielectric Structure*, Phys. Rev. Lett. **65**, 1877 (1990).

[3] B. Y. Tong, P. K. John, Y.-T. Zhu, Y. S. Liu, S. K. Wong and W R. Ware, *Fluorescence-Lifetime Measurements in Monodispersed Suspensions of Polystyrene Particles*, J. Opt. Soc. Am. B **10**, 356 (1993).

[4] E. P. Petrov, V. N. Bogomolov, I. I. Kalosha and S. V. Gaponenko, *Spontaneous Emission of Organic Molecules Embedded in a Photonic Crystal*, Phys. Rev. Lett. **81**, 77 (1998).

[5] M. Megens, H. P. Schriemer, A. Lagendijk and W. L. Vos, *Comment on "Spontaneous Emission of organic Molecules Embedded in a Photonic Crystal"*, Phys. Rev. Lett. **83**, 5401 (1999).

[6] P. Lodahl, A. F. van Driel, I. S. Nikolaev, A. Irman, K. Overgaag, D. Vanmaekelbergh and W. L. Vos, *Controlling the Dynamics of Spontaneous Emission from Quantum Dots by Photonic Crystals*, Nature **430**, 654 (2004).

[7] A. Badolato, K. Hennessy, M. Atature, J. Dreiser, E. Hu, P. M. Petroff and A. Imamoglu, *Deterministic Coupling of Single Quantum Dots to Single Nanocavity Modes*, Science **308**, 1158 (2005).

[8] A. Kress, F. Hofbauer, N. Reinelt, M. Kaniber, H. J. Krenner, R. Meyer, G. Böhm and J. J. Finley, *Manipulation of the Spontaneous Emission Dynamics of Quantum Dots in Two-Dimensional Photonic Crystals*, Phys. Rev. B **71**, 241304 (2005).

[9] D. Englund, D. Fattal, E. Waks, G. Solomon, B. Zhang, T. Nakaoka, Y. Arakawa, Y. Yamamoto and J. Vučković, *Controlling the Spontaneous Emission Rate of Single Quantum Dots in a Two-Dimensional Photonic Crystal*, Phys. Rev. Lett. **95**, 013904 (2005).

[10] M. Fujita, S. Takahashi, Y. Tanaka, T. Asano and S. Noda, *Simultaneous Inhibition and Redistribution of Spontaneous Light Emission in Photonic Crystals*, Science **308**, 1296 (2005).

[11] S. Weiss, *Fluorescence Spectroscopy of Single Biomolecules*, Science **283**, 1676 (1999).

[12] B. N. G. Giepmans, S. R. Adams, M. H. Ellisman and R. Y. Tsien, *The Fluorescent Toolbox for Assessing Protein Location and Function*, Science **312**, 217 (2006).

[13] R. F. Kubin and A. N. Fletcher, *Fluorescence Quantum Yields of Some Rhodamine Dyes*, J. Lumin. **27**, 455 (1982).

[14] D. Magde, R. Wong and P. G. Seybold, *Fluorescence Quantum Yields and Their Relation to Lifetimes of Rhodamine 6G and Fluorescein in Nine Solvents: Improved Absolute Standards for Quantum Yields*, Photochem. Photobiol. **75**, 327 (2002).

[15] L. Bechger, P. Lodahl and W. L. Vos, *Directional Fluorescence Spectra of Laser Dye in Opal and Inverse Opal Photonic Crystals*, J. Phys. Chem. B **109**, 9980 (2005).

[16] C. P. Lindsey and G. D. Patterson, *Detailed Comparison of the Williams-Watts and Cole-Davidson Functions*, J. Chem. Phys. **73**, 3348 (1980).

[17] A. F. van Driel, I. S. Nikolaev, P. Vergeer, P. Lodahl, D. Vanmaekelbergh and W. L. Vos, *Statistical Analysis of Time-Resolved Emission from Ensembles of Semiconductor Quantum Dots: Interpretation of Exponential Decay Models*, e-print physics/0607043.

[18] M. Megens, J.E.G.J. Wijnhoven, A. Lagendijk and W. L. Vos *Fluorescence Lifetimes and Linewidths of Dye in Photonic Crystals*, Phys. Rev. A **59**, 4727 (1999).

[19] L. Bechger, *Synthesis and Fluorescence of Opal & Air-Sphere Photonic Crystals*, Ph.D. thesis, University of Twente, ISBN: 90-365-1991-8 (2003).

[20] M. Barth, A. Gruber and F. Cichos, *Spectral and Angular Redistribution of Photoluminescence near a Photonic Stop Band*, Phys. Rev. A **72**, 085129 (2005).

[21] N. J. Turro, *Modern Molecular Photochemistry*, University Science Books, California, (1991).

[22] J. R. Lakowicz, *Principles of Fluorescence Spectroscopy* (Second Edition), Kluwer, New-York, (1999).

SAMENVATTING

Spontane emissie is een essentieel proces in generatie van licht uit vele verschillende energiebronnen zoals hitte, elektriciteit of chemische interactie. Derhalve is het de oorzaak van het grootste deel van het licht rond ons. Dit proces brengt straling van fotonen in overgangen tussen hoogenergie en laagenergie toestanden van elementaire lichtbronnen (zoals atomen, moleculen of quantum dots) met zich mee. Aangezien de spontane emissie essentieel is voor diverse dagelijkse toepassingen, zoals lichtgevende dioden, lasers, TV schermen, het oogsten van energie in zonnecellen, is het duidelijk dat de controle over dit fenomeen van groot belang is.

De emissie eigenschappen van de elementaire lichtbronnen worden beinvloed door hun omgeving: de emissie vervalsnelheid (inverse levensduur) van de lichtbronnen wordt bepaald door de lokale optische toestandsdichtheid (LDOS). Er werd voorspeld in 1987 dat fotonische kristallen de LDOS radicaal kunnen wijzigen en daardoor de emissie vervalsnelheden en verspreiding van licht controleren. *Fotonische kristallen* zijn periodieke structuren die uit twee materialen met verschillende brekingsindexen bestaan. Deze periodieke variatie op lengteschalen vergelijkbaar met de golflengte van licht leidt tot interferentie van lichtgolven en tot optische Bragg diffractie. Derhalve zijn de specifieke frequenties belemmerd om zich langs bepaalde richtingen te verspreiden, analoog aan Bragg diffractie van röntgenstralen in atoomkristallen. Dergelijke verboden frequentiebereiken worden *stopgaps* genoemd. Hoe groter het brekingscontrast in de kristallen, hoe erger wordt licht beïnvloed. De situatie wanneer het licht zich in geen richting kan verspreiden, wordt een *fotonische bandkloof* genoemd. Spontane emissie is volledig geremd voor frequenties binnen zo een bandkloof en, omgekeerd, sterk verhoogd voor frequen-

ties buiten de bandkloof. Daarom vormen fotonische kristallen een ultiem gereedschap om licht te manipuleren, welke van extreem belang is voor wetenschappers en ingenieurs.

De recente vooruitgang in nanotechnologie heeft in capaciteit geresulteerd om halfgeleiderstructuren met afmetingen van een paar nanometers te maken. Wegens de kleine grootte, kunnen elektron-gat paren (excitonen) in deze halfgeleider nanodeeltjes worden opgesloten. Dit leidt tot discrete energieniveaus van de excitonen. De nanodeeltjes, die excitons in sferische of cirkelruimten beperken, staan als *quantum dots* bekend. De discrete energieniveaus resulteren in zeer nauwe emissiespectra. De emissiefrequenties kunnen worden afgestemd door de grootte van de nanodeeltjes te variëren: hoe kleiner de grootte, hoe hoger de emissiefrequentie. Deze eigenschappen maken de halfgeleider nanodeeltjes veel belovende elementaire lichtbronnen voor vele nieuwe experimenten en toepassingen.

Dit proefschrift beschrijft tijd- en hoekopgeloste experimenten, waarin de effecten van driedimensionale (3D) fotonische kristallen op de spontane emissie van lichtbronnen (quantum dots en kleurstofmoleculen) worden bestudeerd. In Hoofdstuk 2 wordt een overzicht van de theoretische grondbeginselen van de interactie tussen licht en materie gegeven. We bespreken de factoren die het proces van spontane emissie teweegbrengen en beschouwen in detail de tijdsevolutie van de aangeslagen toestand van de lichtbron die met het gekwantiseerde vacuümveld wisselwerkt. De relatie tussen de snelheid van spontane emissie en de LDOS wordt afgeleid. Het verspreiden van licht in fotonische kristallen wordt onderzocht. Door het voorbeeld van een 1D fotonisch kristal verklaren we de oorsprong van de stopgap. Met behulp van de fotonische dispersierelaties, illustreren we de belangrijke eigenschappen van 3D fotonische kristallen. De door theorie voorspelde sterke veranderingen van de LDOS en vervalsnelheden in 3D fotonische kristallen worden tenslotte besproken.

In Hoofdstuk 3 worden de noodzakelijke gereedschappen om spontane emissie te controleren besproken. Daar bediscussiëren we experimenteel gerealiseerde periodieke structuren met een fotonische bandkloof, de eisen aan hun kristalsymmetrie en dielektrisch contrast voor het openen van de bandkloof evenals de methodes om dergelijke periodieke structuren op grote schaal te vervaardigen. We bespreken optische testen noodzakelijk voor het bestuderen van de interactie van licht met echte fotonische kristallen. Deze testen omvatten metingen van hoekopgeloste spectra van gereflecteerd en doorgelaten licht evenals emissie uit interne lichtbronnen. We beschouwen de rol van onvermijdelijke structurele wanorde in propagatie van licht in echte fotonische kristallen. De fotonische kristallen die in onze emissie experimenten worden gebruikt, worden beschreven, name-

lijk polystyreenopalen en titania inverse opalen. Tot slot bespreken we de lichtbronnen die als interne fluorescente sondes in fotonische kristallen kunnen worden gebruikt.

Hoofdstuk 4 beschrijft de hoekopgeloste metingen van emissie spectra van laserkleurstoffen en quantum dots in opalen en inverse opalen. We nemen duidelijke richtingsafhankelijkheden van de emissie spectra waar: de bereiken van hoeken van sterk verminderde emissie grenzen aan deze met verbeterde emissie. Het blijkt dat de emissie uit ingebedde lichtbronnen zowel door de periodiciteit als door de structurele imperfecties van de kristallen wordt beinvloed: de fotonen worden verstrooid door kristalroostervlakken (Bragg diffractie) en eveneens verspreid door onvermijdelijke structurele wanorde. We verklaren kwantitatief de gemeten richtingsafhankelijke emissie met hulp van een model dat transport van diffuus licht en de fotonische bandstructuur verenigt.

In Hoofdstuk 5 tonen we een experimenteel bewijs van de sterk gewijzigde emissie vervalsnelheden van een ensemble van CdSe quantum dots in de titania inverse opalen. Door de roosterparameter van de fotonische kristallen te variëren, bereiken we zowel vertraging als verhoging van de emissie vervalsnelheden. De complexe vervalcurven worden met succes geanalyseerd met een ononderbroken distributie van vervalsnelheden. De resulterende meestfrequente vervalsnelheid varieert met een factor 3, terwijl de breedte van de distributie een zesvoudige wijziging vertoont. Deze grote wijziging van de distributiebreedte in fotonische kristallen met verschillende roosterparameters wordt geidentificeerd met variaties van de radiative vervalsnelheden van quantum dots bij diverse posities in de eenheidscel en met verschillend georienteerde overgangsdipolen. Deze interpretatie wordt vergeleken met berekeningen van de LDOS in de inverse opalen. Het verschil tussen de laagste en de hoogste gemiddelde emissie vervalsnelheid is zelfs een factor 8, overeenkomstig met de verandering van de totale uitgezonden intensiteit. Door de optische frequentie te variëren binnen het emissiespectrum van de quantum dots, merken we op dat de veranderingen van de vervalsnelheid met de roosterparameter groter zijn bij hogere emissiefrequenties.

In Hoofdstuk 6 bespreken we de LDOS in de titania inverse opalen. Met de vlakkegolf benadering hebben we de LDOS in vele posities in de eenheidscel voor verschillende dipooloriëntaties berekend. We vinden dat de LDOS in de inverse opalen sterk afhangt van de roosterparameter evenals van de positie en oriëntatie van de overgangsdipolen. We hebben voorwaarden geidentificeerd waar de LDOS sterk wordt onderdrukt, sterk verhoogt, en waar de scherpe pieken (van Hove singulariteiten) verschijnen. Voor een theoretische verklaring van de experimentele waarnemingen, welke in Hoofdstuk 5 wor-

den beschreven, hebben we berekeningen van de LDOS in verscheidene posities in interne oppervlakken gemaakt. Bij de frequenties dichtbij de laagste stopgap, wordt de afhankelijkheid van de LDOS van de roosterparameter bewaard bij alle onderzochte posities en dipooloriëntaties. Dit feit komt overeen met de experimentele waarnemingen.

Een tijdopgeloste studie van spontane emissie van kleurstofmoleculen (Rhodamine 6G) in opaal fotonische kristallen wordt gepresenteerd in Hoofdstuk 7. Daar, hebben we de fluorescente levensduren gemeten van de kleurstof door zowel optische frequentie als de roosterparameter van polystyreenopalen te variëren. De waargenomen fluorescente levensduren zijn bijna frequentieonafhankelijk binnen het kleurstofemissie spectrum. Dit wordt toegeschreven aan het brede homogene spectrum van de kleurstof. Nochtans, worden de levensduren gewijzigd als de roosterparameter van de opalen wordt veranderd: we observeren 16 % verhoging en 10 % vertraging van de spontane emissie. De waarnemingen worden verklaard door de LDOS, welke in de opalen varieert in bandbreedtes vergelijkbaar met het homogene spectrum van de kleurstof. De veranderingen van de spontane emissie in de polystyreenopalen zijn aanzienlijk kleiner dan de gevolgen die in de titania inverse opalen worden gemeten. Dit feit is verwant aan veel zwakkere veranderingen van de LDOS in de opalen in vergelijking met de inverse opalen.

ACKNOWLEDGMENTS

The title page of this book bears only one name, however, there are other people who directly or indirectly contributed to this work during the last four years. Now, in the final pages of this book, I want to thank all those people.

At first, I am very grateful to my supervisor, Willem Vos, who is always available for questions, is always ready to give advice and to help in overcoming difficulties. Your enthusiasm, Willem, inspired me to do my best in performing experiments, preparing talks and writing reports. I have learned a lot from you during the time of my Ph.D. study. The fact that this thesis has been written within four years despite our move to Amsterdam is undoubtedly also your achievement. I also want to thank Ad Lagendijk. It was fortunate that I worked in one group with such an experienced scientist as Ad. One extremely useful lesson that I learned from Ad is how important it is for scientists to be able to convincingly present themselves and their results.

I am thankful to Peter Lodahl, who was my daily supervisor until he left us for Denmark. Your experience and attitude to work, Peter, impressed me. You helped me a lot during the early years of my Ph.D. study, and I am grateful to you for that. Also I want to thank Femius Koenderink, who was already very experienced in photonic crystals, when I just started at COPS. As a senior comrade he explained a lot about photonics to new Ph.D. students like me. Also I am thankful to Femius for his MatLab script to calculate the LDOS and for helping me to understand that program.

I am grateful to Lydia Bechger and Léon Woldering for those strongly photonic crystals, which I studied with pleasure; and to Floris van Driel for the highly-efficient quantum dots and for sharing his expertise on them. For about nine months I had a student, Karin Overgaag, whose diploma work resulted in great amount of useful experimental data that

were accurately arranged in images and graphs in a bunch of logbooks. Karin, I appreciate that great work.

I want to thank several people for the technical support, namely Cock Harteveld for the perfectly functioning COPS-lab, Bas Benschop for the spotless work of computers, Klaas Smit for his help in the workshop and Rindert Nauta for helping me with electronics. Assistance of many people at AMOLF is greatly appreciated. Particularly, I am very thankful to Rob Kemper for support in the labs, Hugo Schlatter for providing access to a glove box, Roudy van der Wijk for the nice apartment in the city center, Wouter Harmsen and Piet Kistemaker for helping with numerous documents and for the financial support during the move from Enschede.

For the pleasant working atmosphere, I am also thankful to all other COPS/PBG/PS members, particularly, to Tijmen, Boris, Karen Mu., Martijn, Raymond, Karen Mo., Rudolf, Arie, Ivo, Philip, Rob, Peter, Bernard, Tom, Wouter, Willem T., Valentin, Allard, Vitaly, Timo, Bart, Alex, Adriaan, Paolo, Oscar, Dmitry and Merel. In such an international but still very Dutch collective, I could never feel foreign, and this stimulated me to learn the Dutch language quite quickly. Especially, I am grateful to Tijmen, Willem, Karen and Bart for correcting my spoken Dutch; and certainly, to Philip for his great patience in answering my numerous questions on English grammar.

Here in the Netherlands as well as in Germany, I got to know many people from the "Russian-speaking community", with whom I had pleasant time on various occasions. Keeping a close contact with you, guys, helped me to maintain my national identity while living abroad. Finally, I want to express my unlimited gratitude to my dear Ninochka, because of whom I came to do my Ph.D. in this country, and without whom my life would not be so rich and colorful.

I. N.
Amsterdam
17. 09. 2006

APPENDIX A

MODEL OF DETECTION EFFICIENCY OF EMISSION SET-UP

The aim of this appendix is to explain the difference between the calculated escape distribution and the measured raw intensity illustrated in Fig. 4.4. This difference appears because the width of the projection of the collection optics (the spectrometer slit) on the sample increases with angle θ_e. The spectrometer slit is imaged via lens L_1 and L_2 onto the surface of the sample (Fig. 4.1). The only emission collected emanates from the region confined by the slit projection on the sample surface, see Fig. A.1. This means that the spectrometer collects light from a larger region on the surface at larger detection angles, and that the measured angle-dependent intensity should be corrected for the detection efficiency of the set-up. The detection efficiency is modeled as a ratio $D(\mu_e)$ of the intensity $B(\mu_e)$ collected from the surface region within the slit projection (Fig. A.1) at detection

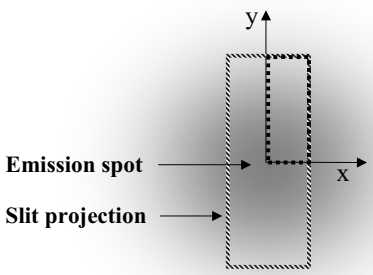

FIGURE A.1: Real-space cartoon of the projection of the spectrometer slit (striped rectangle) on the sample surface overlapped with the emission spot (in grey). One quarter of the slit projection (small dashed rectangle) has one of the corners in the emission-spot center. The width of the projection (along x) increases at larger detection angles θ_e.

angle $\theta_e = \cos^{-1}(\mu_e)$ to the intensity $B(\mu_e = 1)$ collected at normal angle:

$$D(\mu_e) = \frac{B(\mu_e)}{B(\mu_e = 1)}, \quad B(\mu_e) = \int_0^{x(\mu_e)} \int_0^{y_0} I(x, y) dx dy. \tag{A.1}$$

We take into account that the integration runs over a quarter of the slit, as $x(\mu_e) = x_0/\mu_e$ is the half-width of the slit projection, x_0 and y_0 are the half-width and the half-height of the slit projection at $\mu_e = \cos(\theta_e) = 1$, respectively. Typical values of x_0 and y_0 in the experiments are 50 μm and 1 mm. It is assumed that the intensity of diffuse light on the sample surface around the pump beam varies as $I(r) \propto \ell^2/(\ell^2 + r^2)$, where $r^2 = x^2 + y^2$ is the distance from the axis of the pump beam along the sample surface, and ℓ is the mean free path of light in the sample.

Appendix B

Analysis of emission decay curves

This appendix describes analysis of time-resolved emission decay curves - measurements, from which fluorescence decay rates can be extracted. We emphasize the relation between the time-evolution of the excited-state population and that of the corresponding fluorescence decay curve. We consider the cases when the emitting system is described by a single exponential, discrete set of exponentials and continuous distributions.

B.1 Single-exponential decay

Suppose a sample with one sort of fluorophores is excited with an infinitesimally sharp pulse of light. This results in an initial population of the excited state n_0 that is equivalent to the terms 'concentration' or 'number' of the excited fluorophores in the detection volume, which will be equally used throughout this text. The time evolution of the excited emitters decay exponentially, as discussed in Chapter 2, so that

$$n(t) = n_0 \ \exp(-\gamma\, t) \tag{B.1}$$

where $\gamma = \gamma^r + \gamma^n$ is the decay rate of the fluorophores, γ^r is the radiative part of the decay and γ_n is the non-radiative part. The decay rate has a meaning of a number of decay processes per time. In a fluorescence experiment, we do not directly measure the number of excited emitters, but rather the fluorescence intensity *I(t)*. The magnitude of *I(t)*, the flow if emitted photons, is determined by how fast the number of excited emitters decreases so that $I(t) = \Delta n(t)/\Delta t$. Conversely, the change of the concentration within a time bin between 0 and t is proportional to the integral of *I(t)*:

$$\int_0^t I(t')dt' = [n_0 - n(t)]\eta, \tag{B.2}$$

where $\eta = \gamma^r/\gamma$ is the quantum yield of the fluorophores. The normalized fluorescence intensity $f(t) = I(t)/n_0$ is a probability density function of a photon arrival with a dimension of *per time*. The probability that a fluorophore emits a photon in a time window between t_1 and t_2 (let the time of the excitation pulse $t_p = 0$ and $t_1, t_2 \geqslant t_p$) is $p = \int_{t_1}^{t_2} f(t)dt$, while $p_\infty = \int_0^\infty f(t)dt = \eta$.

According to Eq. B.2, the fluorescence decay intensity should be written as

$$I(t) = n_0\gamma^r \ \exp(-\gamma\, t) \tag{B.3}$$

and has a dimension of *per time*. The average amount of time the fluorophores remain in the excited state after the excitation pulse can be calculated knowing the intensity distribution $I(t)$:

$$< t >= \frac{\int_0^\infty I(t)tdt}{\int_0^\infty I(t)dt} = \frac{\int_0^\infty t\exp(-\gamma\, t)dt}{\int_0^\infty \exp(-\gamma\, t)dt} = \frac{1}{\gamma}. \tag{B.4}$$

We see that for a single-exponential decay the average time $< t >$ is equal to the lifetime $\tau = 1/\gamma$. It should be mentioned that the last statement is not true for more complex decay laws, such as multi-exponential and non-exponential decays.

B.2 Discrete set of exponential decays

The fluorescence decay is often multi-exponential when the sample contains several (or many) different sorts of fluorophores. The same will be seen in a case of only one fluorophore in a varying environment (chemically or optically). The total number of excited emitters in the sample is given by

$$n(t) = \sum_{i=1}^{N} n_i \ \exp(-\gamma_i\, t), \tag{B.5}$$

where n_i and γ_i are the excited-state population at $t = 0$ and the decay rate of an i-fluorophore (or of the fluorophore in an i-medium), respectively. N is the number of sorts of the fluorophores (or of the media), *i.e.*, the number of single exponentials.

Consequently, the intensity of a multi-exponential decay is

$$I(t) = \sum_{i=1}^{N} n_i\gamma_i^r \ \exp(-\gamma_i\, t), \tag{B.6}$$

where γ_i^r is the radiative decay rate of an i-fluorophore. In cases when γ^r and γ^n both vary independently, Equation B.6 is not correct: for a certain γ_i there can be more than one

different radiative parts of the decay γ_i^r. In such a situation Eq. B.6 should be rewritten as

$$I(t) = \sum_{i=1}^{N} \Big[\exp(-\gamma_i\, t) \sum_{j=1}^{M_i} n_{ij}\gamma_{ij}^r \Big], \tag{B.7}$$

where n_{ij} is an initial exited-state population of an i-fluorophore demonstrating a radiative decay γ_{ij}^r and a total decay radiative decay ($\gamma_{ij}^r + \gamma_{ij}^n = \gamma_i$, no summation over j). M_i is the number of such i-fluorophores. Thus, single exponentials composing a multi-exponential decay can consist themselves from emission decays of various fluorophores (or of a fluorophore in various environments), which in their turn have the same total decay γ_i (the same decay slope) while revealing different radiative decays γ_{ij}^r (*i.e.*, different quantum yields). Since all these decays with different quantum yields still still show the same slope, it is convenient to take into account only the total weight of the single-exponential decay α_i which represents the amplitude at $t = 0$. So, we have:

$$\sum_{j=1}^{M_i} n_{ij}\gamma_{ij}^r = \alpha_i, \tag{B.8}$$

and the multi-exponential intensity decay is written as

$$I(t) = \sum_{i=1}^{N} \alpha_i\ \exp(-\gamma_i\, t). \tag{B.9}$$

The total emission in the case of multi-exponential decay is

$$\int_0^\infty I(t)dt = \sum_{i=1}^{N} \alpha_i\ \gamma_i^{-1}. \tag{B.10}$$

The average time $< t >$ for a fluorophore in the system to emit a photon can be calculated using Eq. B.4 and is

$$< t >= \frac{\sum_{i=1}^{N} \alpha_i\ \gamma_i^{-2}}{\sum_{i=1}^{N} \alpha_i\ \gamma_i^{-1}} = \sum_{i=1}^{N} f_i\gamma_i^{-1}, \tag{B.11}$$

where f_i is the fractional contribution of an i-single exponential to the total intensity.

B.3 Continuous distribution of exponential decays

There are situations when the fluorescence decay cannot be described by a discrete number of decays, but rather by a distribution of single-exponential decays. One can imagine

a fluorophore in a continuously varying environment, and each environment results in a different decay rate γ. In this case the total number of excited emitters is

$$n(t) = \int_0^\infty \rho(\gamma) \exp(-\gamma\, t) d\gamma, \tag{B.12}$$

where $\rho(\gamma) = n(\gamma)/\Delta\gamma$ is a distribution density of fluorophores over decay rates - number of emitters with decay γ per $\Delta\gamma = \gamma + 1/2\Delta\gamma - (\gamma - 1/2\Delta\gamma)$.

By analogy with the case of discrete distributions (see Eq. B.7) the total emission decay is written as

$$I(t) = \int_0^\infty d\gamma \exp(-\gamma\, t) \int_0^\gamma d\gamma^r \rho(\gamma, \gamma^r)\gamma^r, \tag{B.13}$$

where $\rho(\gamma, \gamma^r) = \frac{n(\gamma,\gamma^r)}{\Delta\gamma\Delta\gamma^r}$, and γ^r can take values from 0 and up to γ ($\gamma^n = 0$). The integral over γ^r

$$\int_0^\gamma d\gamma^r\, \rho(\gamma, \gamma^r)\gamma^r = \alpha(\gamma) \tag{B.14}$$

is defined as a radiative-decay weighted distribution of decay rates $\alpha(\gamma)$ with dimension of [*number of photons*]. Thus, a multi-exponential intensity decay is given by

$$I(t) = \int_0^\infty \alpha(\gamma) \exp(-\gamma\, t) d\gamma, \tag{B.15}$$

and at time $t = 0$:

$$\int_0^\infty \alpha(\gamma) d\gamma = I(0). \tag{B.16}$$

In many cases of continuous distribution of decay rates, the rates are distributed around some center (or most-frequent) value of the decay rate, and therefore, one often uses Gaussian, Lorentzian, log-normal or other functions to describe the function $\alpha(\gamma)$.

If a decay curve *I(t)* is successfully modeled with a decay-rate distribution model, then the function $\alpha(\gamma)$ found from the fit gives information on contribution of each single-exponential with γ to the total emission decay. In order to find a distribution of emitters from a known distribution of single-exponentials, further knowledge of relation between γ^r and γ is required.